

University of Southampton Research Repository ePrints Soton

Copyright © and Moral Rights for this thesis are retained by the author and/or other copyright owners. A copy can be downloaded for personal non-commercial research or study, without prior permission or charge. This thesis cannot be reproduced or quoted extensively from without first obtaining permission in writing from the copyright holder/s. The content must not be changed in any way or sold commercially in any format or medium without the formal permission of the copyright holders.

When referring to this work, full bibliographic details including the author, title, awarding institution and date of the thesis must be given e.g.

AUTHOR (year of submission) "Full thesis title", University of Southampton, name of the University School or Department, PhD Thesis, pagination

UNIVERSITY OF SOUTHAMPTON FACULTY OF ENGINEERING AND THE ENVIRONMENT

Lightweight Lead Acid Batteries for Hybrid Electric Vehicle Applications

by

Lauren Wallis

EngD

January 2015

UNIVERSITY OF SOUTHAMPTON

ABSTRACT

FACULTY OF ENGINEERING AND THE ENVIRONMENT

Electrochemical Engineering
Engineering Doctorate

Lightweight Lead Acid Batteries for Hybrid Electric Vehicle Applications by Lauren Wallis

This report presents architectures, designs and chemistries for novel static soluble lead acid batteries, with the objective of producing a lightweight lead acid battery for improved specific energy. The demands for lightweight lead-acid batteries come from an expanding hybrid electric vehicle market demanding improved battery specific energy. There are several avenues for improving battery specific energy; the main two are improved active material utilisation efficiency and grid weight reduction. Both of these have been focuses of this project.

Two approaches have been taken in this project, the first is focussed on the electrode design. Design modifications have been achieved by using novel grid materials to reduce weight and novel electrode designs to improve active material utilisation. Battery electrodes were built from titanium and the active material was applied as a thin film of lead. Characterisation of lead coatings on several material geometries under different plating regimes was conducted. A novel thin-film active material battery was designed, built and tested satisfactorily to industrial standards.

The second battery system being investigated has the active materials solvated in the methanesulphonic acid electrolyte during the discharged state. Due to the high solubility of lead in this Pb-CH₃SO₃H electrolyte, lead-acid batteries with this chemistry have a theoretical specific energy of 35.7 Ah l⁻¹. This compares favourably with the specific energy for a conventional spiral wound VRLA battery at 44.4 Ah l⁻¹. These soluble lead acid batteries operate by a mechanism whereby cycling is stripping and plating lead and lead dioxide onto the electrodes. Active material utilisation in this type of lead-acid battery is not limited in the same way as conventional lead-acid batteries, as the discharge product is not electrically insulating, as is lead sulphate. The operation mechanism was improved by using additives in the electrolyte to maintain a quality deposit and preserve charge efficiency, voltage efficiency and active mass utilisation. In addition, the use of a separator membrane and novel carbon-polymer electrodes improved battery performance further. The behaviour of a static soluble lead acid battery during cycling with and without additives and a cell membrane is characterised and the results are used to develop a 6 V battery. The results of the 6 V battery cycling under HEV simulated cycling are presented and discussed.

Supervisors

Dr. Richard Wills

Contents

1	\mathbf{Intr}	oduction
	1.1	Project background
	1.2	Objectives
	1.3	Industrial project
		1.3.1 Approach
	1.4	Soluble Lead-Acid Cell
2	Nov	el battery designs for improved energy and power density, including hybrid
	elec	ric vehicle applications.
	2.1	Introduction
	2.2	Terminology
		2.2.1 Hybrid Electric Vechicles
		2.2.2 Battery requirements
	2.3	Test regimes
	2.4	HEV battery criteria
	2.5	Novel Designs
		2.5.1 Bi-polar designs
		2.5.2 Composite
		2.5.3 Ebonex [®]
		2.5.4 CDPE electrodes and novel paste
		2.5.5 Summary
	2.6	Hybrid supercapacitors
	2.7	Soluble Flow Batteries
	2.8	Novel designs: conclusions
		2.8.1 Materials
		2.8.2 Performance: compare reported data and evaluate in comparison to HEVs 2
	2.9	Novel Materials
		2.9.1 Carbon
		2.9.2 Cyclic Voltammetry
		2.9.3 Batteries
		2.9.4 Summary
	2.10	Conductive polymers and ceramics
	2.11	Metals
	2.12	Summary and conclusions
3	Exp	erimental 3
	3.1	Reagents: Preparation of Chemicals, Solutions and Gases
		3.1.1 Lead solutions
	3.2	Cyclic Voltammetry
		3.2.1 Set-up
		3.2.2 Materials and electrolytes
		3.2.3 Electrode preparation

	3.3	Electrodeposition	3
		3.3.1 Set-up	3'
		3.3.2 Electrodes and Electrolytes	38
	3.4	Amperometry	4
		3.4.1 Set-up	4
		3.4.2 Electrolytes	4.
	3.5	SEM: Scanning Electron Microscope	4
	3.6	Battery Charge and Discharge Cycling	42
		3.6.1 Battery 1: TWI Thin Film Battery	42
		3.6.2 Batteries 2 and 3: Static Soluble Lead Acid Batteries	42
		3.6.3 Electrode preparation	44
4	\mathbf{Res}	ults: Electrochemistry of electrode materials in acid solutions	46
	4.1	5 M H_2SO_4	46
	4.2	Electrodes in 6 mM Pb^{2+} in aqueous CH_3SO_3H (1 M)	48
	4.3	Summary of material suitability	51
5	Res	ults: Thin Film lightweight battery	52
_	5.1	Electrodeposition on titanium meshes	52
	0.1	5.1.1 Electrodeposition summary	57
	5.2	Battery testing	58
	5.3	Thin Film battery summary	60
	0.0	Timi Timi baccery summary	U
6	\mathbf{Res}	ults: Soluble static lead-acid battery. Proof of concept	62
	6.1	Undivided cells: -/-/-, -/Bi/Bi and -/Li/Li	62
	6.2	Divided cells: Na/-/-, Na/Bi/Bi and Na/-/Bi $\ \ldots \ \ldots \ \ldots \ \ldots \ \ldots$	66
	6.3	$Lignin sulphonic\ acid\ cells:\ Na/Li/Li\ and\ Na/Li/Bi\ \dots\dots\dots\dots\dots\dots\dots$	68
	6.4	Soluble static lead-acid battery: Summary and conclusions	7.
7	Elec	ctrode studies: galvanostatic amperometry	72
•	7.1	Electrolyte concentration effects	73
	•	7.1.1 Summary	79
	7.2	Limiting factors: mass transport and electrode kinetics	79
	7.3	Conclusions	82
	1.5		Ŭ-
8		ults: Soluble static lead-acid battery. Further studies	83
	8.1	High current tests of 1-cells O	83
		8.1.1 Comparison of 2D and 3D cells: the 1-cells J and K	87
	8.2	3D electrodes under HEV simulated cycling: 1-cells and and 4-cells	88
		8.2.1 Electrode compression ratios	89
		8.2.2 4-cell s-HEV cycling: a bipolar 6 V battery	92
		0.2.2 Teems HZ v eyemig. a sipolar v v sactory	-
		8.2.3 Comparison of 1-cell and 4-cell	95
	8.3		

9 Conclusions 98

List of Figures

1	PALC test regime. The C_1 current is first established. The PALC test involves	
	constant current cycling at the C_1 current mulitplied by a factor	11
2	Bi-polar battery electrode configuration in comparison to mono-polar plates. [73]	14
3	Operating potentials for the lead acid battery. The equilibrium potentials for the	
	lead to lead sulphate reaction and the lead dioxide to lead sulphate reaction and	
	the hydrogen and oxygen evolution reactions are shown. The electrolyte is 1 M	
	H_2SO_4 ,[14] 4.5 M H_2SO_4 ,[28] [7] 5 M H_2SO_4 , [69] and 1.28 g cm ⁻³ H_2SO_4 .[21]	23
4	Cyclic voltammetry of various carbons over the lead-acid battery operating po-	
	tential range. First scan is shown. Electrolyte and scan rate in parentheses. a	
	Petroleum-pitch-based carbon foam (4.5 M H ₂ SO ₄ , 5 mV s ⁻¹) [7], b Natural graph-	
	ite $(4.5 \text{ M H}_2\text{SO}_4, 5 \text{ mV s}^{-1})[23]$, c Synthetic-pitch-based graphite foam (4.5 M)	
	H_2SO_4 , 5 mV s ⁻¹)[28], d RVC (5.3 M H_2SO_4 , 1 mV s ⁻¹)[22]	24
5	Carbon-electrode battery cycle life as a function of thickness of carbon-coating	
	corrosion protection layer. a [7], b [23], c [13], d [34], e [22]	28
6	Cyclic voltammetry of various metal oxides over the lead-acid battery operating	
	potential range. Electrolyte in parentheses. a $TiRuO_2(1.29 \text{ sp. gr. } H_2SO_4)$ [26],	
	b NbSi ₂ (1.365 sp. gr. $\rm H_2SO_4$) [30], c Ebonex (1.0 mol dm $^{-3}\rm H_2SO_4$)[73], d TiSi ₂	
	$(1.365~{\rm sp.~gr.~H_2SO_4})~[30],~{\rm e~BaPbO}~(0.5~{\rm M~H_2SO_4})~[49],~{\rm TaSi_2}~(1.365~{\rm sp.~gr.}$	
	H_2SO_4) [30]	31
7	Photograph of the 3 chamber glass cell used in cyclic voltammetry, as connected	
	to potentiostat. From left to right: reference electrode, working electrode, counter	
	electrode	35
8	Schematic diagram of the 3 chamber glass cell used in cyclic voltammetry. Elec-	
	trolyte used was 5 M H_2SO_4	35
9	Photograph of the 2 chamber glass cell used in cyclic voltammetry, as connected	
	to potentiostat. From left to right: working electrode, counter electrode, reference	
	electrode	36
10	Schematic diagram of the 2 chamber glass cell used in cyclic voltammetry. Elec-	
	trolyte used was 6 mM Pb 1 M CH_3SO_3H	36
11	Typical resin-mounted electrode material as used in the two chamber cell during	
	cyclic voltammetry.	37
12	Electrodeposition bath, 2000 ml. 293 K \pm 2, magentic stirrer	38
13	Example of a 100 x 100 mm titanium Fibretech electrode, with electrical connec-	
	tion	38
14	Battery 1 casing and electrodes.	42
15	Battery 2 (single cell) and battery 3 (four cell) in isometric projection	43
16	Components used in Battery 2 (single cell), including carbon-polymer composite	
	electrode, nickel electrode and current collector, silicone spacer and gasket, and	
. -	Nafion ® membrane.	43
17	Cyclic voltammogram of lead in 5 M H ₂ SO ₄ at 50 mV s ⁻¹ from -0 V vs. SCE to	
	-1.75 V to 1.9 V vs. SCE	47

18	a, b and c. Cyclic voltammograms of various electrode materials in 6 mM Pb 1 M CH ₃ SO ₃ H at 25 mV s ⁻¹ from -0.3 V to -0.8 V to -0.3 V vs. saturated calomel	
	electrode. 293 K	49
19	Lead electrodeposit on titanium mesh. 50 mA cm $^{-2}$ for 30 minutes at 293 \pm 5 K	
	in 1.5 M Pb ²⁺ CH ₃ SO ₃ H (1 M)	53
20	a Thin Film battery capacity and specific capacity, measured during a constant voltage charge, constant load discharge regime at 293 ± 5 K. b Thin Film battery power and specific power, measured during a constant current charge and discharge regime at 293 ± 5 K	60
21	Four voltage / mV against time / s plots showing the cell voltage during selected charge and discharge cycles of soluble lead acid batteries at 150 mA (6 mA cm ⁻²). Battery -/-/- uses 1.5 M Pb ²⁺ in aqueous CH ₃ SO ₃ H (1 M) electrolyte, battery -/Bi/Bi has 1.5 M Pb ²⁺ and 10 mM Bi ³⁺ in aqueous CH ₃ SO ₃ H (1 M) electrolyte.	63
22	a and b: 3D plots showing cell voltage during charge and discharge cycles of 2D soluble lead acid batteries. a, 1.5 M Pb ²⁺ in aqueous CH ₃ SO ₃ H (1 M) electrolyte (-/-/-). b, 1.5 M Pb ²⁺ and 10 mM Bi ³⁺ in aqueous CH ₃ SO ₃ H (1 M) (C). Constant current cycle regime at 150 mA (6 mA cm ⁻²) for 600 s. Charge voltage cut-off 3 V, discharge voltage cut-off 1.2 V. 293 K	64
23	Battery -/-/- electrodes after cycling showing active material remaining on the surface after cycling: left; Pb negative electrode, right; PbO ₂ positive electrode. Constant current charge and discharge at 150 mA (6 mA cm ⁻²) for 600 s. Charge voltage cut-off 3 V, discharge voltage cut-off 1.2 V. 293 K.	64
24	Four voltage / mV against time / s plots showing the cell voltage during selected charge and discharge cycles of soluble lead acid batteries at 150 mA (6 mA cm ⁻²). Battery -/Li/Li uses 1.5 M Pb ²⁺ in aqueous CH ₃ SO ₃ H (1 M) with 1 g l ⁻¹	01
25	ligninsulphonic acid electrolyte	65
26	aqueous CH_3SO_3H (1 M) with a Nafion [®] separator membrane (Na/Bi/Bi) Voltage efficiency for batteries Na/-/-, Na/Bi/Bi and Na/-/Bi. Soluble lead-acid cells with 1.5 M Pb ²⁺ in aqueous CH_3SO_3H (1 M) electrolyte, Nafion [®] membrane and 0.01 M Bi ³⁺ (D and E). Cycle regime: constant current, 150 mA for 600 s.	67
27	Charge voltage cut-off 3 V, discharge voltage cut-off 1.2 V. 293 K Four plots showing the cell voltage during selected charge and discharge cycles of soluble lead acid batteries Na/Li/Li and Na/Li/Bi. Cycle regime: constant current, 150 mA (6 mA cm ⁻²) for 600 s. Charge voltage cut-off 3 V, discharge voltage cut-off 1.2 V. 293 K. Soluble lead-acid cells with 1.5 M Pb ²⁺ in aqueous CH ₃ SO ₃ H (1 M) electrolyte with ligninsuphonic acid (1 g l ⁻¹) and Nafion [®] membrane (G)	68
	and $\mathrm{Bi^{3+}}(0.01\ \mathrm{M})\ (\mathrm{H})$	69

28	Voltage efficiency for soluble lead acid cells -/Li/Li, Na/Li/Li and Na/Li/Bi. Soluble lead-acid cells with 1.5 M Pb ²⁺ in aqueous CH ₃ SO ₃ H (1 M) electrolyte with	
	ligninsuphonic acid 1 g l ⁻¹ , Nafion [®] membrane (-/Li/Li and Na/Li/Li) and 0.01	
	M Bi ³⁺ (Na/Li/B). Cycle regime: constant current, 150 mA (6 mA cm ⁻²) for 600	
	s. Charge voltage cut-off 3 V, discharge voltage cut-off 1.2 V. 293 K	69
29	Concentration of Pb^{2+} in solution in the electrolyte for each battery at the end of	
	each cycle. Coloured lines correspond to cells, black dashed lines to values 0 and	
	1 for coulombic efficiency. The cell lettering is shown in table 27	70
30	Negative electrode current response to constant, stepped potentials. a Electrolyte:	
	0.01 M Pb ²⁺ in aqueous CH ₃ SO ₃ H (1 M). b Electrolyte: 1.5 M Pb ²⁺ in aqueous	
	${ m CH_3SO_3H}$ (1 M).293 \pm 2 K. The applied potentials are shown in the figure legend.	75
31	Lead electrode limiting currents as a function of applied overpotential and electro-	
	lyte $[Pb^{2+}]$. Potentials range from -0.78 to -0.18 V $vs.$ SCE, where the equilibrium	
	potential is assumed to be -0.42 V. Electrolyte $[Pb^{2+}]$ ranged from 0.01 M to 1.5	
	M Pb ²⁺ in aqueous CH ₃ SO ₃ H (1 M). 293 \pm 2 K. Left: deposition potentials; right:	
	dissolution potentials	76
32	Positive electrode current response to constant, stepped potentials. a Electrolyte:	
	$0.75~\mathrm{M~Pb^{2+}}$ in aqueous CH ₃ SO ₃ H (1 M). 293 \pm 2 K. b Electrolyte: 0.75 M Pb ²⁺	
	in aqueous CH ₃ SO ₃ H (1 M) with 10 mM Bi ³⁺ . 293 \pm 2 K. The applied potentials	
0.0	are shown in the figure legends	78
33	Lead dioxide electrode limiting currents as a function of applied overpotential and	
	electrolyte $[Pb^{2+}]$. Potentials range from 0.80 to 2.20 V vs. SCE, where the equilibrium potential is assumed to be 1.50 V. Electrolyte $[Pb^{2+}]$ ranges from 0.01	
	M to 1.5 M Pb ²⁺ in aqueous CH ₃ SO ₃ H (1 M) with 10 mM Bi ³⁺ . 293 \pm 2 K. Left:	
	deposition potentials; right: dissolution potentials	79
34	Lead (a) and lead dioxide (b) electrode limiting currents as a function of applied	10
J -	overpotential and electrolyte [Pb $^{2+}$]. Potentials range from 0.80 to 2.20 V vs.	
	SCE, where the equilibrium potential is assumed to be 1.47 V. Electrolyte $[Pb^{2+}]$	
	ranged from 0.01 M to 1.5 M Pb ²⁺ in aqueous CH ₃ SO ₃ H (1 M). 293 \pm 2 K. Left:	
	deposition; right: dissolution.	81
35	Corroded nickel negative electrode current collector taken from 1-cell J after con-	
	stant current cycling at 20 mA $\rm cm^{-2}$. In subsequent tests, 1-cell O was used	84
36	A voltage vs. time plot showing cell voltage during charge and discharge cycles	
	of 1-cell O, a soluble lead acid cell. Constant current cycle regime at 150 mA (6	
	mA cm ⁻²) for 600 s. Charge voltage cut-off 2.5 V, discharge voltage cut-off 1.2	
	V. 293 K. 1.5 M Pb ²⁺ in aqueous CH ₃ SO ₃ H (1 M) electrolyte at the negative	
	electrode and 1.5 M Pb ²⁺ and 10 mM Bi ³⁺ in aqueous $\mathrm{CH_3SO_3H}$ (1 M) at the	o -
	positive electrode.	86

37	A voltage vs. time plot showing cell voltage during charge and discharge cycles of a 1-cell K and a 1-cell O static soluble lead acid cells. Constant current cycle regime at 150 mA (6 mA cm ⁻²) for 600 s. Charge voltage cut-off 2.5 V, discharge voltage cut-off 1.2 V. 293 K. 1.5 M Pb ²⁺ in aqueous CH ₃ SO ₃ H (1 M) electrolyte	
	at the negative electrode and 1.5 M Pb ²⁺ and 10 mM Bi ³⁺ in aqueous CH ₃ SO ₃ H	
	(1 M) at the positive electrode	88
38 39	Constant current charge and discharge cycle regime s-HEV A voltage vs . time plot showing cell voltage during charge and discharge cycles	89
	of 1-cell N static soluble lead acid cell. s-HEV cycle regime at 500 mA (20 mA cm ⁻²). Charge voltage cut-off 2.5 V, discharge voltage cut-off 1.2 V. 293 K. 1.5 M	
	Pb ²⁺ in aqueous CH ₃ SO ₃ H (1 M) electrolyte at the negative electrode and 1.5 M	0.1
40	Pb ²⁺ and 10 mM Bi ³⁺ in aqueous CH ₃ SO ₃ H (1 M) at the positive electrode A voltage vs. time plot showing cell voltage during charge and discharge cycles	91
40	of a 1-cell O 3D soluble lead acid cell. s-HEV cycle regime at 500 mA (20 mA cm ⁻²). Charge voltage cut-off 2.5 V, discharge voltage cut-off 1.2 V. 293 K. 1.5 M	
	Pb ²⁺ in aqueous CH ₃ SO ₃ H (1 M) electrolyte at the negative electrode and 1.5 M	
	Pb ²⁺ and 10 mM Bi ³⁺ in aqueous CH_3SO_3H (1 M) at the positive electrode	91
41	A voltage vs. time plot showing cell voltage during charge and discharge cycles	91
	of three soluble lead acid cells under three different compressions: 0, 25 and 75	
	%. These are 1-cells O N and M. Both electrodes are 3D carbon felt. The charge	
	regime is s-HEV cycle regime at 500 mA (20 mA cm ⁻²). Charge voltage cut-off 2.5	
	V, discharge voltage cut-off 1.2 V. 293 K. 1.5 M Pb ²⁺ in aqueous CH ₃ SO ₃ H (1 M)	
	electrolyte at the negative electrode and 1.5 M Pb ²⁺ and 10 mM Bi ³⁺ in aqueous	
	CH ₃ SO ₃ H (1 M) at the positive electrode	92
42	A voltage vs. time plot showing cell voltage during charge and discharge cycles of	
	4-cell B, a static soluble lead acid cell. s-HEV cycle regime at 500 mA (20 mA	
	$$ cm $^{\!-2}).$ Charge voltage cut-off 9.5 V, discharge voltage cut-off 4 V. 293 K. 1.5 M	
	${ m Pb^{2+}}$ in aqueous ${ m CH_3SO_3H}$ (1 M) electrolyte at the negative electrode and 1.5 M	
	$\rm Pb^{2+}$ and 10 mM $\rm Bi^{3+}$ in a queous $\rm CH_3SO_3H$ (1 M) at the positive electrode. 	93
43	A voltage vs. time plot showing cell voltage during charge and discharge cycles	
	of a modified 4-cell A, a static soluble lead acid cell. This cell has half the 3D	
	electrode removed, and the electrolyte level is half of 4-cell A. s-HEV cycle regime	
	at 250 mA (20 mA $\rm cm^{-2}$). Charge voltage cut-off 8.5 V, discharge voltage cut-off	
	4.8 V. 293 K. 1.5 M $\mathrm{Pb^{2+}}$ in aqueous $\mathrm{CH_3SO_3H}$ (1 M) electrolyte at the negative	
	electrode and 1.5 M $\mathrm{Pb^{2+}}$ and 10 mM $\mathrm{Bi^{3+}}$ in aqueous $\mathrm{CH_3SO_3H}$ (1 M) at the	
	positive electrode.	94
44	Electrolyte levels in the $5.6~\mathrm{ml}~6~\mathrm{V}$ battery have increased after s-HEV cycling	94

List of Tables

1	Types of lead acid battery: commercially available Cyclon D-cell (benchmark);	
	industrial project thin-film electrode battery; novel static soluble lead acid battery.	2
2	Hybrid electric vehicle terminology as used in the literature.	6
3	Hybrid vehicle performance requirements	8
4	Technology Readiness Level (TRL). Higher number indicates a shorter time-scale	
	to commercialisation. Based on NASA TRLs. [48]	9
5	HEV test profiles: study-specific. Positive current = charge, negative current =	
	discharge	10
6	A collection of model HEV test regimes used in the literature. There are different	
	sign conventions and standard units according to nationality of the author	12
7	HEV test profiles: real-life data from hybrid electric vehicles. Positive current =	
	$charge, \ negative \ current = discharge. \ \dots $	13
8	Specifications for Power-Assist HEVs	14
9	Summary comparison of bi-polar battery electrodes and paste material. (Values	
	are for active material utilisation unless stated otherwise.) [32]	17
10	Carbon materials used as battery electrodes and manufacturing processes	22
11	Coatings applied to carbon to provide corrosion protection	26
12	Summary of novel grid materials investigated for use in lead acid batteries showing	
	the voltage range over which they are suitable for use and relevant performance	
	characteristics and behaviours.	32
13	Chemicals used during the project, inleuding the supplier and purity.	34
14	Electrolytes used during cyclic voltammetry, including concentration	35
15	Titanium meshes used as substrates during electrodeposition of lead, electrolyte	
	composition 1.5 M Pb 1 M CH_3SO_3H with 1 g l^{-1} ligninsulphonate	40
16	Electrolyte used during amperometry experiments, including concentration	41
17	Materials used as cell electrodes, including supplier and a brief description	43
18	Materials used during the project for other components of both the batteries 1 and	
	2 (single- and four-cell), including supplier and a brief description	44
19	Lead-plated titanium electrodes used in battery 1 (single-cell). The substrate	
	material, mass of deposited lead, total electrode mass and pre- and post-treatments	
	are listed	44
20	Lead-plated titanium electrodes used in battery 1 (single-cell). The substrate	
	material, mass of deposited lead, total electrode mass and pre- and post-treatments	
	are listed	45
21	Nucleation overpotential for shortlisted substrate materials in 6 mM Pb 1 M	
	${ m CH_{3}SO_{3}H}$ at 25 mVs ⁻¹ . 293 K	51
22	SEM images showing the morphology and distribution of lead electrodeposited	
	onto Goodfellow woven mesh from 1.5 M Pb 1 M methanesulphonic acid with 1 g	
	l^{-1} ligninsulphonic acid at 55.5 mA cm $^{-2}$ for time periods between $20 - 120$ minutes.	
	$293 \pm 5 \text{ K}$	53

23	SEM images of lead electrodeposited from 1.5 M Pb 1 M methanesulphonic acid at 293 ± 5 K at current densities between 14 and 221 mA cm ⁻² . 0.21 g cm ⁻² of	
	lead was deposited during each set.	55
24	The lead - titanium interface after electrodeposition from 1.5 M Pb 1 M methanes-	
	ulphonic acid at current densities between 55.5 mA cm ⁻² and 221 mA cm ⁻² for	
	60 minutes. 293 ± 5 K	56
25	Table showing mass of electrodes used in the thin film battery, including with and	00
	without active material. Also included is the Cyclon D cell, where the mass of the	
	electrode is the mass of the grid without active material.	58
26	Soluble lead-acid cell configurations, showing nomenclature, separator membrane	
	and additives.	62
27	Cell voltages, voltage efficiencies and cycle number to failure for soluble lead acid	
	batteries under charge and discharge cycles: constant current, 150 mA (6 mA cm ⁻²)	
	for 600 s. Charge voltage cut-off 3 V, discharge voltage cut-off 1.2 V. 293 K	70
28	Galvanostatic Amperometry experimental conditions: potentials	73
29	Galvanostatic Amperometry experimental conditions: electrolytes	73
30	Significant limiting currents: 0.75 M Pb ²⁺ , $\eta = 0.2$ V	79
31	Nomenclature of cells used in this chapter under the s-HEV cycle regime: 2D	
	carbon polymer composite and 3D carbon felt electrodes, 2 V and 6 V cells with	
	different interelectrode gaps. Electrolyte composition was 1.5 M $\mathrm{Pb^{2+}}$ in aqueous	
	${ m CH_3SO_3H}$ (1 M) electrolyte for the negative electrode, and 1.5 M ${ m Pb^{2+}}$ and 10 mM	
	${\rm Bi^{3+}}$ in aqueous ${\rm CH_3SO_3H}$ (1 M) for the positive electrode. The charge voltage	
	cut-off was 2.5 V, discharge voltage cut-off 1.2 V for the 1-cells.	83
32	High constant current cycling test regime used with 3D 1-cells O. The applied	
	charge and discharge currents, cycle times and corresponding DoDs are listed.	
	The surface area is geometrical surface area. Electrolyte composition was 1.5 M	
	Pb ²⁺ in aqueous CH ₃ SO ₃ H (1 M) electrolyte for the negative electrode, and 1.5	
	M Pb ²⁺ and 10 mM Bi ³⁺ in aqueous CH ₃ SO ₃ H (1 M) for the positive electrode.	0.4
00	The charge voltage cut-off was 2.5 V, discharge voltage cut-off 1.2 V. 293 K	84
33	Charge and voltage efficiency for three selected cycles of 1-cells O with 3D electrodes under the high current cycle regime at 150, 600, 1086 and 1809 mA for	
	600 s. Charge voltage cut-off 2.5 V, discharge voltage cut-off 1.2 V. 293 K. 1.5 M	
	Pb ²⁺ in aqueous CH ₃ SO ₃ H (1 M) electrolyte at the negative electrode and 1.5 M	
	Pb ²⁺ and 10 mM Bi ³⁺ in aqueous CH ₃ SO ₃ H (1 M) at the positive electrode	86
34	Cycle life of 1-cells O with 3D electrodes under the high constant current cycling	00
J 1	test regime	87
35	Comparison of 1-cells K with 3D electrodes to 1-cells J with 2D electrodes and a	٠,
	nickel negative electrode, at 150 mA constant current cycling.	87

36	Constant current charge and discharge cycle regime s-HEV. Current, SoC, cell con-	
	dition and step time are listed for each cell volume. The surface area is geometrical	
	surface area. Electrolyte composition was 1.5 M $\mathrm{Pb^{2+}}$ in aqueous $\mathrm{CH_3SO_3H}$ (1 M)	
	electrolyte for the negative electrode, and $1.5~\mathrm{M~Pb^{2+}}$ and $10~\mathrm{mM~Bi^{3+}}$ in aqueous	
	CH ₃ SO ₃ H (1 M) for the positive electrode. The charge voltage cut-off was 2.5 V,	
	discharge voltage cut-off 1.2 V. 293 K	89
37	Actual SoC for the 1-cells N and O. SoC calculations are based on: during charge;	
	the time to reach a charge voltage above 2.2 V and during discharge; the time to	
	reach the lower voltage cut-off. The discrepancy is caused by capacity fade	92
38	Comparison of performance for 1-cell N and 4-cell A under s-HEV tests	95
39	Specific energy of 1-cells and 4-cells. Table includes mass of individual components	
	and electrolyte.	96

Academic Thesis: Declaration Of Authorship

I, Lauren Wallis

declare that this thesis and the work presented in it are my own and has been generated by me as the result of my own original research.

Lightweight Lead Acid Batteries for Hybrid Electric Vehicle Applications

I confirm that:

- 1. This work was done wholly or mainly while in candidature for a research degree at this University;
- 2. Where any part of this thesis has previously been submitted for a degree or any other qualification at this University or any other institution, this has been clearly stated;
 - 3. Where I have consulted the published work of others, this is always clearly attributed;
- 4. Where I have quoted from the work of others, the source is always given. With the exception of such quotations, this thesis is entirely my own work;
 - 5. I have acknowledged all main sources of help;
- 6. Where the thesis is based on work done by myself jointly with others, I have made clear exactly what was done by others and what I have contributed myself;
- 7. Either none of this work has been published before submission, or parts of this work have been published as: [72]

Signed:	
Date:	

Acknowledgements

Firstly, my thanks go to my supervisor, Richard Wills, for supporting me throughout this project. His encouragement, advice and friendship has been invaluable. I am grateful that he took me on as his first student.

Without financial support, this project would not have been possible, so I wish to thank TWI and the EPSRC for their funding. TWI were also generous with their use of facilities and materials, which I also acknowledge.

I wish to express my warm gratitude to those in Electrochemical Engineering: everyone in the department has helped me in some way over the years. The lab has been a good working environment, and I wish everyone all the best.

Also, working with the EngD cohort has been a great experience. I wish to thank the IDTC for the support and stimulating environment. It has been enriching.

Most of all, I am grateful to those family members and friends who continually encouraged me and showered me with support.

Nomenclature

3D Three dimensional

 η Overpotential / V

ABS Acrylonitrile butadienestyrene

AGM Absorbtive glass mat

Ah Battery capacity / Ah

ALABC Advanced Lead Acid Battery Consortium

BET Brunauer-Emmett-Teller surface area test

BFE Boron fluoride electrolyte

BILAPS Bipolar Lead Acid Power Source

C-rate The current at which the battery would discharge in 1

hour

CDPE Carbon doped polyethylene

CSM Copper stretch metal

DoD Depth of Discharge

EIS Electrochemical impedance spectroscopy

EU European Union

EUCAR European motor industry research body

F Faraday's constant 96500

GHG Greenhouse Gases

HDPE High density polyethylene

HEV Hybrid electric vehicle

HR-PSoC High-rate partial state of charge

IPCC Intergovernmental Panel for Climate Change

ITRI International Tin Research Institute

j current density

LABD Lead acid battery development

M Mass / g

m Molecular mass

NAM Negative active mass

NiMH Nickel-metal-hydride

NTA Nitrilotriacetate electrolyte

PALC Power-assist life cycle

PAM Positive active mass

PANI Polyaniline

PMMA Poly(methyl methacrylate)

PNGV Partnership for new-generation vehicles

PSoC Partial state of charge

PTFE Polytetraflouroethlyene

RHOLAB Reliable, highly optimised lead-acid battery

RVC Reticulated vitreous carbon

s-HEV Simulated Hybrid Electric Vehicle battery test regime

SCE Saturated Calomel Electrode

SHE Standard hydrogen electrode

SLI Starting, lighting and ignition

SoC State of Charge

 ${f t}$ Time / ${f s}$

TRL Technology readiness level

VRLA Valve regulated lead acid

XRD X-ray diffraction

z Valency

1 Introduction

The main body of the thesis contains the literature review and an experimental section. Conclusions and recommendations for future work and references follow. The literature review describes the lead acid battery technology, limitations, applications and emerging applications. Within the experimental section is the material selection, the industrial project, and proof of concept and development of a static soluble lead acid battery.

1.1 Project background

Energy storage is an important technology in many applications, and lead acid batteries occupy the largest market share. New applications for lead acid batteries are emerging; each application requires specific design improvements to meet the performance. A major emerging application for lead acid batteries is the hybrid electric vehicle (HEV). This report describes lead acid battery performance in this application and analyses novel designs which have been proposed in the literature. Two novel battery designs have been built and tested for suitability in HEV applications. They have been compared to a benchmark commercially-available battery which is similar to some deomonstration HEV batteries in the literature. Performance characteristics of the three batteries are presented in table 1.

1.2 Objectives

The project objective is to design, build and test a lightweight lead acid battery, which has characteristics suitable for HEV applications. Two methods have been investigated: using novel, lightweight electrodes and novel electrolyte. The novel electrolyte battery chemistry is based on the methanesulphonic acid / lead system. This system has the potential to address the limiting factors faced by conventional lead acid batteries, there is no insulating lead sulphate and it is possible to use a high-current bi-polar configuration. The electrode geometry will be optimised for surface area-to-volume ratio of the electrolyte according to the system characteristics. Therefore, the battery configuration will be bi-polar with novel 3D electrodes.

	Conventional lead-acid battery	Thin-film active material lead-acid battery	Static soluble lead-acid battery
Project example	Benchmark, Cyclon D cell	TWI industrial project	Lab demonstration battery
$_{ m image}$	Cyclon 2 VOLT 2.5 AH D CELL SEALED-LEAD RECHARGEABLE BATTERY NONSPILLABLE MADE IN USA		
Full cell reaction	$Pb + PbO_2 + 2H_2 SO_4 \Leftrightarrow PbSO_4$	$Pb + PbO_2 + 2H_2 SO_4 \Leftrightarrow PbSO_4$	$\mathrm{Pb} + \mathrm{PbO}_2 \Leftrightarrow \mathrm{Pb}^{2+}$
Description	2 V, valve regulated spiral wound battery. Pasted active materials on cast lead grids.	2 V, flat plate battery. Electrodeposited, thin film active material on titanium grids. Three grid manufacturing methods: sintering, expanding, weaving.	6 V static soluble battery. Solvated active material, which electrodeposits during charge. Planar 2D electrodes of nickel and carbon-polymer composite positive, and of 3D carbon felt.
$\frac{\text{Specific energy / Ah}}{\text{kg}^{-1}}$	17.30	0.15-0.52	5.54
Specific energy $/$ Ah l^{-1}	44.41	6.80	38.46

Table 1: Types of lead acid battery: commercially available Cyclon D-cell (benchmark); industrial project thin-film electrode battery; novel static soluble lead acid battery.

1.3 Industrial project

The objective of this industry-based project was to design, build and test a novel lead acid battery using titanium grids electrodeposited with lead as electrodes. Different grid geometries were compared to a commercially available battery. The work was carried out in conjunction with the TSB-funded project LAB-LCV at TWI. One of the main work packages within LAB-LCV was the development of a fibrous metallic titanium mesh. The use of titanium as a substrate material for the battery electrodes provides significant weight reduction, resulting in increased specific capacity and power over a battery with lead-electrodes. The titanium meshes manufactured in LAB-LCV were compared to commercially available products. A lightweight lead-acid battery based on the principle of thin-film active material was designed, manufactured and tested. The thin-film of active material was electrodeposited onto the substrate material to produce battery electrodes, which were tested by battery charge and discharge cycling. All the electrodeposited electrodes performed better than solid lead electrodes, but the best performing were those with the thinnest layer of electrodeposited lead. Furthermore, the electrode design was considered suitable as a stand-alone electrode or as a grid for pasting. The lightweight electrodes are particularly suitable for applications such as hybrid electric vehicles. The electrodes can be stacked in series to produce a higher voltage battery.

1.3.1 Approach

The project was split into two research strands:

- Electroplating optimisation including bath design, electrolyte composition, current density and temperature.
- Electrode manufacture and test characterisation of the cell during charge/discharge conditions.

The purpose of the tests was to ascertain the effect of electrode geometry and active material preparation on cell performance. Three different electrode geometries and two post-deposition treatments were used.

1.4 Soluble Lead-Acid Cell

A novel lead acid battery with soluble active materials is under development. The methanesulphonic acid / lead system has been investigated with cyclic voltammetry and battery cycling. Cell design has been iterative; improvements have been made by: including a separator membrane and electrolyte additives, which have been shown to increase cell cycle life by 300%; and using 3D electrodes in a bipolar configuration to increase power. Further characterisation of this system has involved interelectrode gap optimisation, state of charge investigations and a multi-cell battery construction and test according to a literature-standard HEV test regime.

2 Novel battery designs for improved energy and power density, including hybrid electric vehicle applications.

2.1 Introduction

A critical overview of electrode materials for lead-acid batteries is presented in the context of improved energy and power density for emerging applications, including hybrid electric vehicles (HEVs). Technical progress and performance characteristics of HEVs and lead-acid batteries potentially suitable for HEV applications as reported in the academic literature are compared. Types of novel lead-acid battery are briefly summarised, drawing attention to their construction, material composition and relative merits. Novel battery designs considered in this paper include bi-polar, hybrid supercapacitor and soluble flow, and novel grid materials include metals, carbons and polymers. Where available, demonstration batteries are discussed in relation to the performance requirements for HEVs.

It is now unequivocal that anthropometric greenhouse gas emissions (GHG) are causing significant changes to natural systems. [27] Land and sea temperature increases are already affecting snow and ice cover; river levels and number and sizes of lakes; weather patterns including heat waves, frosts, droughts, and floods; and associated impacts on life. Predictions show that as the GHG concentrations increase, these effects will worsen. [27] Many international bodies, including the IPCC and the EU Climate Commission, are calling for steps towards climate change mitigation by GHG emission reduction. Total global anthropometric GHG emissions totaled 49 Gt CO₂ eq / yr in 2010, with 76 % from CO₂ and the remainder from methane, nitrous oxide and fluorinated gases. This is produced mainly by electricity and heat production, industry and transport. Out of the three sectors analysed for capacity to mitigate emissions - in industry; transport and buildings - transport is described as offering the highest potential reduction, of 20-50 %, by 2050. While industry could reduce GHG emissions by up to 20 % using technology, emissions from buildings are highly dependent on behavioural change and thus uncertain. [77] Transport offers the highest likelihood of the highest GHG reductions of all the sectors: this is a compelling reason to focus on reducing transport GHG emissions.

The available methods to achieve a reduction in transport GHG emissions are numerous and varied. While the IPCC discusses fuel improvements, infrastructure development, and modal shift, much of development has been on improving cars. For example, the EU legislation aimed at decreasing transport GHG emissions covers emissions targets for new vehicles, fuels and tyres to reduce drag. [18] Rightly so, as in the UK, 58 % of the transport emissions come from cars and taxis. [15] The automotive industry has responded to the emissions targets in many ways, including; reducing the vehicle mass, improving aerodynamics, increasing drive-train efficiency, and in some models, using alternative propulsion systems. These methods correspond to all terms in the vehicle power consumption equation 1, except for reducing speed.

$$power_{car} \approx 4 \left[\frac{1}{2} m_c v^3 / d + \frac{1}{2} \rho A v^3 \right]$$
 (1)

The alternative propulsion systems are of particular interest as they are a technological so-

lution rather than a design solution. They include full-electric vehicles, hybrid and hydrogen powered vehicles. As the most common of these vehicles are the hybrids (HEVs), they will form the focus of this study.

By installing an electric motor and a battery, which provides power to the wheels in addition to the engine, an immediate reduction in GHGs is possible. This is simply because the electric motor is powered by electricity generated during idling, coasting or braking (known as regenerative braking). The actual fuel savings from HEVs are contested, and range in the literature from negligible to up to 37 %. [1, 29, 67] An additional benefit is the associated reduction in fuel cost, which may offset the increase in outlay cost, incurred due to the increased complexity of the system as well as the motor and battery. Indeed, in HEVs, the largest additional cost is that of the battery. The performance demands for batteries in this application are high: specifc power and energy, recharge rate, cost, self-discharge rate; and each of the available battery chemistries offers a combination of some but not all of these characteristics. For example, lithium batteries have a much higher specific power than lead-acid batteries, but have a much higher cost than both lead acid and nickel-metal-hydride batteries (NiMH). [19] All three battery chemistries are used in HEVs on the market, depending on the precise product specification. Currently, the cheapest and the only recyclable battery is the lead-acid battery. In addition, the lead acid battery does not require a battery management system, has a wider operating temperature range and lower self-discharge rate than the other chemistries. [19] For these reasons, there is a large incentive to improve the specific energy and power of the lead acid battery.

The bibliography for lead-acid batteries is extensive, due to its long history and wide ranging applications, including telecommunications, backup power and portable devices, as well as in the automotive industry. As result, the technology has been much improved since Planté's discovery in 1859. Prominent research groups include the Lead Acid Battery Development (LABD) at the Bulgarian Academy of Sciences, who mainly seek to understand the systems, and the Advanced Lead Acid Battery Consortium (ALABC), who develop the technology with collaborative industrial demonstration projects. The chemistry, operating conditions and performance characteristics are well described in several papers. [4, 47, 70, 51, 19, 58] Improvements have been made consistently on the cycle life and reliability, but recently the focus of development has moved to increasing the specific energy and power, particularly for hybrid electric vehicle applications. Greater specific energy has been achieved by both lightweighting components using novel designs and/or materials [46, 3, 67] and improving active material utilisation. [50, 2, 56, 58] Novel designs evaluated in this paper include bi-polar, hybrid supercapacitors and soluble flow batteries; which use materials including metals, carbons, polymers and composites, to varying levels of demonstration.

The scope of this review is to discuss the use of novel electrode designs and materials in leadacid batteries, particularly performance requirements for hybrid electric vehicle applications. This includes an analysis of the battery requirements for hybrid electric vehicles (including cycle life, active material utilisation, specific power and energy), as well as an evaluation of novel battery designs using formations of carbon, metals, polymers and composites, where reported in the academic literature.

2.2 Terminology

This section of the paper aims to clarify the terminology in order to establish some criteria for assessing suitability of batteries for this application. Definitions of hybrid vehicles, battery performance requirements and experimental methods are discussed.

2.2.1 Hybrid Electric Vechicles

There are a number of requirements for HEV batteries; in addition to powering the auxiliary on-board electricals and starting, lighting and ignition (SLI). It is most common in the literature for HEVs to be described according to the functions, and there are twelve common labels for differing types, as shown in table 2. Some of the same labels are used to describe vehicles with different operating modes; for example, the label 'mild' refers to HEVs without power assist in one case and with power assist in three cases. For simplicity, the differing types have been divided into three categories according to function: stop-start, power-assist and pure-electric; these terms will be used throughout this paper. The most common and well-described HEV type is the power-assist.

	Other names	Modes of		References
		operation		
	stop-start	Stop-start		[47]
		function.		
Stop-Start	dual battery			[47]
	micro	Regenerative		[65][38][63]
	mild	braking.		[38]
	micro-mild		36 V, 150 Ah	[45]
	soft	Electrically		[47]
	mild	assisted launch.		[65]
	power assist			[38][3]
Power-Assist	mild	Power-assist		[47][66]
	full	during low-speed.		[38]
	medium		25-40 kW 0.3-0.5 kWh	[45]
	full	Longer and more		[47]
		frequent power		
	medium	assist.		[8]
	pure electric	Electric only		[38]
Pure Electric	plug-in	mode (limited		[47]
	dual mode	range).		[3]

Table 2: Hybrid electric vehicle terminology as used in the literature.

2.2.2 Battery requirements

The different HEV battery requirements as described in the lead-acid battery literature are shown in table 3. Each row in the table shows the important parameters of an HEV battery, and each column represents a different HEV mode. The range of requirements across studies is shown. For example, in a Stop-Start mode, the energy requirements range from 20 to 90 Ah. The battery power and energy requirements increase as the number of operating modes increase (from left to right in the table); a few examples of HEV battery characteristics are detailed here.

The operating mode for stop-start batteries involves SLI and charging during coasting and

braking. An example of a battery used in this applications is be the BMW 12 V 70 Ah valve-regulated lead acid absorbtive glass mat (VRLA-AGM) [63]. 12 V batteries with a lower energy capacity of 50 Ah are used in two of the three demonstration vehicles from an ALABC demonstration programme, including the Citroen C3 Stop & Start, the Renault Clio and the Ford Fiesta Microhybrid. [65] There are also designs for stop-start HEVs using the 42 V electrical system, and this requires a 36 V 20 Ah [66] or 25 Ah [45] battery.

The power-assist HEV battery is required to provide assistance to the internal combustion engine during acceleration and hill climbing, and to receive charge during regenerative braking. [3] It can be as small as 36 V, operating on the 42 V system. [66, 65], and ranges as high as 144 V [45][8] or 360 V [3]. The energy capacity requirements range from 0.3 - 0.5 kW h [45] to 1 - 2 kW h [3] and 1 - 3 kW h [38, 42] to ~5 kW h [65]. The power requirements also range widely from 15 kW [66] to 60 kW [38], but the most common range is from 25 - 30 kW. Some studies have smaller power requirements for charge than discharge. [60, 45]

Pure electric hybrids have some all electric driving range (as well as the other features) of up to 30 - 50 miles so therefore they have a larger energy requirement. [3] The battery voltage ranges from 202 V [42] to 300 - 360 V. [3]

As can be seen, the data from the literature is incomplete and based on different test regimes. A fuller analysis of HEV-specific battery performance is given below.

2.3 Test regimes

The level of development of the batteries reported in the literature varies from small single electrode tests to in-vehicle demonstrations. The experimental method is considered and distinctions made between proof of concept by electrochemical methods including cyclic voltamettry, and demonstration batteries tested in laboratories or in field tests. The stage of development is considered in terms of technology readiness levels (TRL), as defined in table 4.

Pure-Electric	max.	100	20	360	ı	ı	0.4	
	I	50	6 - 10, 10	300	ı	ı	ı	[3][38][42]
Pur	min.	37.8	1.3	201.6	6.5	29	0.2	<u>S</u>
Power Assist	max.	09	3	336, 300-360	31	150	2-4	[09]
	ı	15, 20, 20-30, 50	1, 1-2	144, 144	ı	48, 60	-	[65][8][38][66][45] [3][62][60
	min.	6.3-11.7	0.3 - 0.5	36, 36	∞	40	0.5	[9]
Stop- Start	max.	15	П	36	06	ı	ı	[45]
	ı	10	ı	ı	25	25	ı	[66][45]
	min.	6	0.5	14	20	ı	ı	[38]
Deremotor	r aranicoci	kW	kW h	Λ	Ah	kg	$kW kg^{-1}$	reference

Table 3: Hybrid vehicle performance requirements.

	HEVs.	NASA missions.
TRL	Descr	iption
1	Research on basic principles, e.g.	Basic principles observed and reported.
	cyclic voltammetry.	
2	Proof-of concept tests are conducted	Technology concept and/or application
	on a small demonstration-cell under	${\it formulated}.$
	generic test regimes. Some	
	performance data of the components	
	are given, e.g. resistance of the plates	
	or specific currents $/$ A cm ⁻² .	
3	Tests are conducted on a small battery	Analytical and experimental critical
	under generic test regimes.	${\rm function~and/or~characterists}$
		${\it proof-of-concept.}$
4	Tests are conducted on a small battery	Component/subsyste, validation in
	under application-specific test regimes,	laboratory environment.
	e.g. PALC. Some important feasibility	
	indicators are ascertained e.g. cycle	
	life or specific capacity.	
5	Tests are conducted on a battery	System/subsystem/component
	under application-specific test regimes.	validation in relevant environment.
	More rigorous tests, more indicators	
	are measured and the design includes	
	some optimisation.	
6	Full-size battery laboratory testing,	System/subsystem model or
	i.e. sufficient voltage for the intended	prototyping demonstration in a
	application.	relevant end-to-end environment
		(ground or space).
7	Demonstration in real-world	System prototyping demonstration in
	application, e.g. in an HEV.	an operational environment.
8	Product is available on the market.	Actual system completed and 'mission
		qualified' through test and
		demonstraion in an operational
		environment (ground or space).
9	Product is available on the market and	Actual system 'mission proven'
	with sales.	through successful mission operations
		(ground or space).

Table 4: Technology Readiness Level (TRL). Higher number indicates a shorter time-scale to commercialisation. Based on NASA TRLs. [48]

Along with the number of HEV definitions, there are a similar number of battery test regimes used in the literature. These are reported in tables 5, 6 and 7. All of the tests operate at high-rate partial state of charge (HR-PSoC). The majority of tests (shown in table 5) have been designed for the study but there are some standard tests (shown in table 6) and some tests based on real-life vehicle data (shown in table 7). It must be considered that study-specific tests may be biased towards the performance of the battery rather than to the requirements of HEVs.

HEV battery cycling profile (cut-offs are in brackets)						Description	Reference	
Test time / s	Voltage	Nominal	Power	Current	Current	Current	Describaton	1 retereile
	/ V	capac-	/ kW	at C ₁ -	at C_5 -	/ A		
		ity /		rate /	$\mathrm{rate}\ /$			
		%		A	A			
0 - 30	(1.77)	-	-	-	-2.5	-	Simplified test regime.	
30 - 36.8	=	-	=	-	0	-	Constant current then	
36.8 - 67.8	2.5	-	-	-	2.5	-	constant voltage charging.	
67.8 - 74.6	-	-	-	-	0	-	Used as an initial	[38]
							comparison test prior to	
							PALC tests.	
0 - 10	-	-	4	-	-	-	Partnership for	
10 - 36	=	=	0	-	=	=	new-generation vehicles	
36 - 38	_	_	-6	_	-	_	(PNGV) test profile. Not	
38 - 42	_	_	-4	_	-	_	used in the study. Positive	[8]
42 - 46	_	_	-2	_	=	_	current = discharge,	
46 - 72	_	_	0	_	=	_	negative current = charge.	
0 - 60		_	-	-		-35		
60 - 60.5	_	-	- -	~18	-	-300	Simulated HRPSoC 42 V	
60.5 - 70	_	-	-	10	-	-150	cycling. Constant current	
70 - 140	14	-	=	-	=	35	then constant voltage	
	14	-	-	-	-		charging conducted on $12~\mathrm{V}$	[37]
140 - 145	-	-	-	-	-	0	batteries. Failure was	
145 - 150	14	=	=	-	=	35	end-of-discharge voltage at	
							9.6 V under HRPSoC.	
<u> </u>	(1.75)	_	_	-1	_	_		
57600	2.47	_	_	0.2	_	_		
-		(50)		-1				
10	_	(30)		0	_	_	Simplified HEV cycle test.	
60	(2.83)	-	-	2	-	_	Constant current then	
10	(2.00)	-	-	0	-	_	constant voltage charging at	
60	_	-	-	-2	-	_	steps 2, 10 and 12.	[44]
repeat steps		-	-		-	-	Comparison between	[44]
• •	(1.83)	-	-	-	-	-		
4 - 7 once	(1.75)	-	-	-1	-	-	standard VRLA and	
57600	2.47	-	=	0.2	=		optimised batteries.	
-	(1.75)	-	-	-1	-	-		
57600	2.47	- (*0)	-	0.2	-	-		
-	- (10)	(50)	-	-1	-	-		
9000	(10)	-	=	-	-	-10	(a) 11 · · · ·	
1800	(10)	-	-	-	-	-17.5	Shallow cycling at partial	
2400	14.4	-	=	-	=	(17.5)	state of charge. Pass	
repeat steps	=	-	=	-	=	=	requirement is not stated,	
2 - 3 85 times							but 1600 cycles is more than	[67]
-	(10.5)	-	-	-	-	-2.5	three times the requirement.	
64800	14.4	-	-	-	-	(5)	Demonstrates the ability of	
-	(10.5)	-	=	-	=	-2.5	the Orbital batteries to pass	
82800	14.4	-	-	-	-	(5)	this and several other tests.	
repeat steps	-	-	-	-	-	-		
1 - 7 six times								
30	(7.2)	-	=	-	=	-480		

Table 5: HEV test profiles: study-specific. Positive current = charge, negative current = discharge.

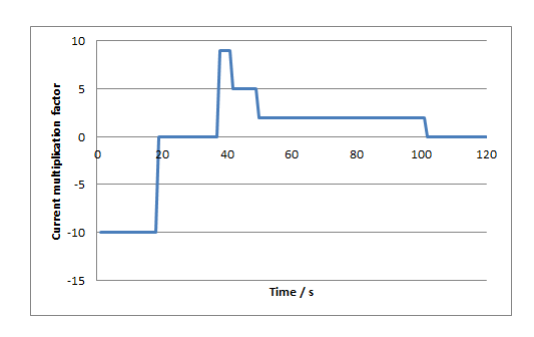


Figure 1: PALC test regime. The C_1 current is first established. The PALC test involves constant current cycling at the C_1 current mulitplied by a factor.

The power-assist life cycle (PALC) test is: the most frequently used; internationally recongised; scalable to different sized batteries; designed by vehicle manufacturers and similar to the reported in-vehicle tests. [8] The PALC test involves first establishing the C₁ current, and then constant current testing at a multiples of this current, as shown in figure 1. The C₁ current is the current which discharges the battery in one hour. Several studies use the PALC regime, as shown in table 6. For these reasons, it is a good and robust test regime. The largest discharge current in the PALC is -10 C₁. Study-specific HEV tests use discharge currents of differing magnitude. In two studies using simplified test regimes the maximum discharge current was much smaller than the PALC: 1 C₁ [44] and 0.2 C₁ (- 10 A of a 50 Ah battery). [67] The other simplified test regimes (shown in table 5) were significantly more demanding than the PALC, at -12.5 C₁ and around -18 C₁[38, 37]. The PALC test regime sits centrally within the range of battery tests.

Test time / Power / Current /		Current /	Description	Reference
s	kW	A		
0 - 18	-	80		
18 - 37	=	0	FUGAR	
37 - 41	-	-72	EUCAR power assist test regime, not	
41 - 49	-	-40	used in this study. Positive current =	
49 - 101	=	-18	discharge, negative current = charge.	
101 - 120	Ξ	0		[8]
0-10	4	-		[6]
10-36	0	-		
36-37	-6	-	PNGV Power Assist. Positive current	
37-43	- 4	-	= discharge.	
43-48	-2	-		
48-72	0	=		
0 - 18	-	-300		
18 - 37	=	0		
37 - 41	=	250	EUCAR Power-assist life cycle profile.	[62]
41 - 49	=	150	Negative current $=$ discharge.	[02]
49- 101	=	80		
101- 120	=	0		
0 - 18	=	-28	EUCAR power assist test regime.	
	-		Used as part of test regime: discharge	
	-		to 60% SoC at 0.5 C ₂ rate, 10,000	
18 - 37	-	0	EUCAR cycles; recharge for 20h at	
37 - 41	=	25	2.45 V; 2h capacity determination	[38]
41 - 49	=	14	then repeat until failure. Failure is	
49 - 101	-	6	defined as either the measured	
101 - 120	-	0	capacity becoming less than 50% or	
			the cell voltage falling below 1.4 V.	

Table 6: A collection of model HEV test regimes used in the literature. There are different sign conventions and standard units according to nationality of the author..

Real-vehicle-data-based bench tests (table 7) used scaled-down voltages but currents similar to the PALC. Bench tests of a 36 V, 8 Ah battery under the real Reliable, highly optimised lead acid battery (RHOLAB) test regime give 50 A peak charge and -95 A peak discharge currents. (Real-life in-vehicle tests were conducted with 144 V batteries.) This corresponds to 6.3C₁ and -11.95 C₁ which is similar to the PALC requirements. In the same study, an HEV test run gave similar current traces to the RHOLAB test regime of between 50 A and -100 A, validating the test regime well. [8] . Real data was used to test an 80 V module, which was scaled down from a 336 V design. The test profile included charge peaks at 80 A and discharge peaks at -120 A. It is not possible to compare these values to the PALC as the battery capacity was not reported. [60]

HEV	battery cycling	profile (real-world tes	Description	Reference	
	Number of			Description	Reference
Time / s	cycles	Power / W	Current /		
	(approx.)		A		
0 - 1500	50	-	60 to -95	Cycle profile taken from the	
1500 - 2000	15	-	50 to 0	RHOLAB hybrid vehicle, bench	[8]
				testing conducted on a 36 $ m V$	
0 - 1000	13	-	40 to -20	battery.	
1000 - 5400	80	-	30 to -90	In-vehicle testing in a Honda	
5400 - 8000	8	-	30 to - 35	Insight Vehicle at Millbrook	[8]
8000 - 9000	2	-	15 to - 65	proving ground.	
0 - 450	10	2500 to -2500	-	Cycle profile provided by TNO	
450 - 2000	35	7500 to -7500	-	from a hybrid vehicle: peaks	[60]
				above 40K kW removed and	[ooj
				reduced by a factor of 4.	
0 - 450	10	2500 to -2500	-	Cycle profile provided by TNO	
				from a hybrid vehicle: peaks	
450 - 900	12	6000 to -4000	_	above 40K kW removed and	[60]
900 - 2000	12	4000 to -4000	_	reduced by a factor of 4.	
900 -2000	8	8000 to -8000	-	reduced by a factor of 4.	

Table 7: HEV test profiles: real-life data from hybrid electric vehicles. Positive current = charge, negative current = discharge.

2.4 HEV battery criteria

For simplicity, when evaluating the batteries described in this review, the following criteria will be used to assess suitability for HEV applications. The main assumption is that the type of HEV is Power-Assist. This is because: it is the most common HEV type; there is real-life vehicle test data available; Stop-Start hybrid perfomance requirements mentioned in the literature are not based on published evidence; the Pure-Electric hybrid vehicle specifications are taken from the Toyota Prius which has a NIMH battery, so will be discounted here. [42] Also, it should be noted that the Pure-Electric hybrid requirements are similar to one definition of the Power-Assist requirements. [62] This is due to the flexibility of the definitions used to describe HEVs. [60, 8] The peak power required is 6.3-40 kW for charge, 11.7-50 kW for discharge (0.27 and 0.33 kW kg⁻¹for charge and discharge), minimum capacity 8 Ah and voltage of 144 or 336 V. The cycle life is particularly difficult to define because it is not mentioned in these real-vehicle tests and the cycle-life test regimes used vary widely (shown in tables 5, 6 and 7). For simplicity, the PALC cycle life of 100 000 cycles will be used. [62] (The number of cycles is so high because this is a shallow charge and discharge regime.) Using the PALC regime is justified as most of the benchand in-vehicle-tests are similar to the PALC.

These specifications (table 8) will be used as a benchmark when evaluating the novel lead-acid batteries for suitability for HEV applications.

	Mini	mum [8]	Preferred [62]		
	Charge Discharge		Charge	Discharge	
Peak kW	6.3	11.7	40	50	
${ m kW~kg^{-1}}$	=	-	0.27	0.33	
A h		3	3	•	
System V		144	336		
PALC cycles		100	000		

Table 8: Specifications for Power-Assist HEVs.

2.5 Novel Designs

2.5.1 Bi-polar designs

Bi-polar designs can provide higher power density than monopolar designs; for example, prototypes have been described which can deliver 4 kW kg⁻¹ over 10 seconds. [71] This value is more than ten times greater than that used in HEVs (table 8). The high power is a result of the low internal resistance, which is a result of the electrode arrangement. The current pathway is shorter than in monopolar designs as it flows through the battery perpendicular to the plane of the individual electrode plates, to current collectors at either end of the battery. Each bipolar electrode therefore has a positive and negative surface, as shown in figure 2. Current flow in this orientation, rather than along the electrode plate to current collectors at the top as in conventional designs, optimises current distribution by minimising current inequality as well as resistance caused by current flow along the grid. [10]

Another benefit of bi-polar configuration is that if one electrode pair fails, unlike in the conventional configuration, where the whole battery will fail, the only effect is that the voltage decreases.

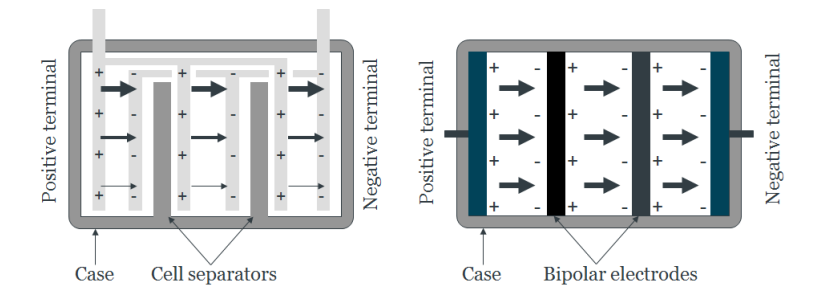


Figure 2: Bi-polar battery electrode configuration in comparison to mono-polar plates. [73]

Electrode material selection is the most contentious point for these battery designs. [30] Along with pre-requisite characteristics for lead acid batteries, the materials must be: non-porous; ionically non-conductive and have enhanced corrosion resistance to prevent electrolyte pathways forming from the positive to negative faces of the electrode. Full cell construction and testing of a variety of bipolar batteries has been produced academically and commercially, with the most advanced examples included here.

2.5.2 Composite

A series of batteries have been built and tested using electrodes of a composite substrate electroplated with lead. While the material composition is undisclosed, the properties are: areal resistance, $0.04~\Omega~\rm cm^2$; density, $1.6~\rm g~cm^{-3}$; specific resistance, $1.2~\Omega~\rm cm$ and low hydrogen and oxygen overpotentials (10 mV at 1 mA cm⁻²). The first bi-polar battery made using this material was 4 V with the active material formed by a Planté ex- and in- situ process. This battery was designed for pulsed-power applications, and galvanostatic testing showed that at 950 W kg⁻¹ the specific energy is 4.1 Wh kg⁻¹.[61] While the voltage is not sufficient for HEV applications, this proof of concept demonstrates that the specific power capability of bi-polar batteries is within HEV requirements.

The bi-polar concept was refined for HEV applications at TNO by increasing the voltage to 80 V, using a thin 3.4 mm cell design with a central cooling plate and an optimised paste. The paste was developed by Centurion and contains hollow fibres of undisclosed composition for high current use at low state of charge (SoC). This 80 V 8 Ah 65 kg battery was tested at 5 kW for 10 s pulses, and a 42 V module was tested at 9 kW for 4 s. The 80 V module gave a discharge current of 140 A (0.26 A cm⁻²) and the 42 V module gave 300 A (0.56 A cm⁻²). Up-scaling and extrapolation using a calculated Ragone plot yields a possible maximum specific power of 450 W kg⁻¹ and the author proposes several weight reduction measures to achieve 500 W kg⁻¹. [60] Unfortunately, this 80 V battery is incapable of providing sufficient power for HEV applications: the reported power is 5 kW and the calculated specific power is 0.172 kW kg⁻¹ (80 V, 140 A, 65 kg).

Further advancement was achieved in the BILAPS European project. This battery stack comprises bi-polar plates, spacer, negative and positive active mass, absorptive glass mat (AGM) separator and O-rings for sealing which allow autopsy of the battery. The improvements include vacuum filling, internal temperature monitoring, cell resistance monitoring, conductive additives in the paste, a re-crystallisation prevention technique involving high frequency electronic pulses, and a battery management system. A 12 V and a 30 V battery were built. The cells have an internal resistance of 0.5 m Ω per cell for the 12 V battery, and 0.9 m Ω for the 30 V battery. Tests were carried out under the power-assist life cycle (PALC) profile (see table 6) at 50% SoC of the 12 V, 30 Ah and 36 V, 32 Ah battery. The 12 V battery during discharge at 300 A gives a cell voltage of 1.63 V and 0.4 A cm⁻² and operates steadily for 16 hours. The 36 V battery gives 7 hours of stable running with 7 C discharge and 6.3 C charge peaks and operates a stable operating temperature over 7000 PALCs, however with 10 C discharge and 9 C charge peaks the temperature rises unsatisfactorily. A suggested solution to the temperature rise is to reduce the electrical resistance of the active material. [62] This battery does not fulfill the PALC test requirements that it underwent, or provide sufficient power for HEV requirements. Despite this, the currents are high, and it appears that the power would be sufficient if only the battery voltage could be increased. The many further developments that are required for this design mean that the TRL is around 4.

Although these batteries have not demonstrated sufficient power for HEVs, an important point is that there are no reported problems with the electrode substrate material. The material is reported to be stable and non-sulphating. Although the failure mechanism was not explicitly

described, the limiting factor in the design is stated to be the electrical resistance of the plate; discussion of reducing the internal resistance relates to additives in the paste mix and not to the substrate material composition. It appears that this series of papers has identified a suitable electrode material for bi-polar batteries. However, the material composition is undisclosed by the authors.

2.5.3 Ebonex®

A titanium oxide ceramic, Ebonex[®], is used as the grid material in the Atraverda product, which includes 6, 12, 36 and 42 V designs. Plate resistance is less than 40 $\mu\Omega$; for the total 19 plates this is less than 1 m Ω . [40] The potential operating range for Ebonex is -1.8 to +2.2 V vs. Pb/PbSO₄, density is 11.35 g cm⁻³ and conductivity is 48.544 S cm⁻¹. [17] Other properties of Ebonex[®] can be found in [73]. Atraverda report details of 6 V bipolar batteries with electrodes comprised of Ebonex[®]-polymer coated in a lead alloy interface foil and pasted with active material. These batteries have been tested to IEC 896-2 standard (At least 50 cycles of room temperature discharges at 3 h rate to 75% depth of discharge (DoD). End of life is when capacity falls to 80% rated capacity.) Battery lifetime in accelerated overcharge tests of 1500 h exceeds the pass-criteria by 2.5 times. Post-cycling tear-down after 75 cycles shows that only 10% of the protective metallic foil interface had been corroded; a cycle life of 750 cycles was extrapolated. [40] A 4 V, 7 Ah bi-polar battery using Ebonex[®] electrodes was compared to a 6 V, 1.2 Ah conventional battery and found to have twice the active mass utilisation at 10 C. [73]

This battery has reached commercialisation but is yet to be installed in a commercial product; its techology readiness level (TRL) is actually around 4 or 5 as some tests have been conducted but characterisation is incomplete. The published performance data for these batteries is insufficient to demonstrate suitability for HEVs, however the low voltage and number of cycles to failure suggest that they would be unsuitable. Also, the fact that the cycle life to failure calculation is based on the corrosion rate of the lead-layer suggests that bare Ebonex[®] is not a suitable bi-polar electrode material.

2.5.4 CDPE electrodes and novel paste

This 6 V bipolar battery was constructed in a cylindrical design. A comparative study was conducted between two different electrode materials and pasted positive active materials. All electrodes were 5 cm in diameter and 4 mm thick, and machined with concentric grooves on the surfaces in contact with the active material. One type of electrode was cast from lead-tin alloy, and the other was comprised of carbon doped polyethylene (CDPE) coated in silver then lead (200 µm) via electroless- and electro- deposition respectively. The conventional negative and positive pastes contained battery lead oxide powder, carbon black (0.15 %), CMC (undisclosed acronym) (0.1 %), humic acid (0.1 %), 1,2-acid (0.1 %), barium sulphate (0.2 %), cellulose fibre (0.08 %) and polyamide fibres; the final density was 4.34 g cm⁻³ for the negative paste and 4.25 g cm⁻³ for the postive. The doped positive paste was prepared by adding ammonium persulphate (750 g) and deionized water (780 ml) to the paste mix at 50 ° C. Electrode formation was conducted at 30 mA g⁻¹ and testing was carried out at a current density of 48 mA g⁻¹. The most significant finding from this paper is that while the CDPE-electrode improves the energy and cycle-life

Battery configuration.	mA h	Cycle	${ m mW~g^{-1}}$	$ m mW~h~g^{-1}$
	g^{-1}	life	per unit	
			cell	
Lead-tin electrodes,	150	45	59.7	895.3
conventional paste.				
CDPE electrodes,	152	50	57.4	867.0
conventional paste.				
CDPE electrodes, novel	198	140	83.3	1176.9
paste.				

Table 9: Summary comparison of bi-polar battery electrodes and paste material. (Values are for active material utilisation unless stated otherwise.) [32]

performance, the novel paste formulation yields more significant improvements. Table 9 shows these and other performance data for these batteries, including the specific power of 0.083 kW kg⁻¹, which is an order of magnitude lower than HEV requirements. In addition, the low cycle life and the low TRL of 3 show that this design is currently insufficient for HEVs.

This paper shows that the effect of paste formulation is more significant than the electrode material compostion[32].

2.5.5 Summary

Bi-polar batteries have been shown to have both increased active mass utilisation [76] and peak power over short time periods [36] compared to monopolar batteries. This improvement was shown to be due to the paste formulation rather than the electrode material properties [32]. Paste additives were also discussed as a method to increase the maximum current. [62] While some currents were reported (0.56 A cm⁻² [60] 48 mA g⁻¹ [32]) it is difficult to evaluate these specific values in terms of suitability for HEV applications.

As for electrode material behaviour, there are only two references to corrosion in the literature. It is well known that the high operating potential, dictated by the equilibrium potential for PbO₂, which is 1.6 V vs. SCE in 4.7 mol dm⁻³sulfuric acid, [16] is the reason that corrosion-resistant materials must be used. One study showed that the cycle life is improved by replacing the corrosion-susceptible lead-tin electrode with a CDPE electrode, [32] and another used the lead-tin layer corrosion rate to estimate the Ebonex[®]-based battery life-time. [40] One study did not mention that the lead electrode would soon corrode catastrophically. [36] However, none of the studies explicitly discuss the failure mechanism and several do not cycle to failure. It is beyond the scope of these proof-of-concept, low TRL papers, and reveals that bi-polar batteries are still in the development stage. It appears that until a material which can resist corrosion at high potentials is found, the lifetime of bi-polar batteries will be insufficient for commercialisation in HEVs.

2.6 Hybrid supercapacitors

A capacitor plate is used in conjunction with a conventional battery electrode to produce a device which can offer characteristics of both a capacitor and a battery. The capacitor plate allows high rate operation for short time periods and the battery plate stores sufficient energy for longer low rate discharge. This is especially important during HRPSoC in HEVs.

The most significant hybrid supercapacitor is the UltraBattery. The UltraBattery is designed to meet the performance requirements of HEV applications. It was developed by CSIRO and manufactured by Furukawa in Japan and East Penn in the USA. The design comprises a hybrid negative plate made of half spongy lead (conventional negative plate) and half carbon supercapacitor arranged in parallel. Additives have been incorporated into the carbon capacitor to equalise the potential with the lead electrode, preventing excessive hydrogen evolution. The supercapacitor has been tested extensively, and the first tests were 2.5 C charge and discharge cycles. Bench tests comparing the Ultra-Battery to a similar control cell without the carbon hybrid-supercapacitor show the discharge and charge power have been increased by 50 % and 60 % respectively. The cell completed more than 17000 cycles of the test profile used, shown in Table 7. For comparison, the control cell completed 1500 cycles and a state-of-the-art VRLA completed 4000 cycles. [38] The battery was tested to USFreedomCAR standards, and shown to meet or exceed the minimum standards, as shown in table 2.

The Ultra-Battery was demonstrated in a Honda Insight where 12 x 12 V prototype Ultra-Batteries were installed and outperformed the original NiMH batteries. The HEV completed 100,000 miles in 9 months and gave a fuel efficiency of the vehicle at 4.73 l / 100 km (roughly 60 mpg). During the tests, the battery met all requirements. [9] This battery has demonstrated HEV suitability, and can be given a TRL of 7.

2.7 Soluble Flow Batteries

Soluble lead acid flow batteries use completely novel lead-acid battery chemistry. The active materials are no longer contained in a solid paste on the electrodes, but in solution in the electrolyte, which is composed of Pb²⁺ dissolved in methanesulphonic acid. The mechanism for charge and discharge is dissolution and deposition of lead and lead dioxide onto the negative and positive electrodes respectively.

$$2Pb^{2+} + 2H_2O \leftrightarrow Pb + PbO_2 + 4H^+ \tag{2}$$

[24]

Typically, the cell voltage is roughly 1.5 V during discharge, although the open circuit voltage is 1.78 V. The coulombic efficiency is >85% (the highest coulombic efficiency is 93%) and voltage efficiency is around 65 % .[54] The current density range is 20-160 mA cm⁻², so the battery power can be increased simply by increasing the size and surface area of the electrodes. [76] The current density is not limited by the rate of mass transport as the electrolyte is pumped to flow across the electrodes. The electrolyte is stored in an external tank of any size; thus the energy capacity can be easily increased. The electrolyte conductivity is dependent on both acid and lead ion concentration increasing with acid concentration but decreasing with lead ion concentration so that at 0.9 M CH₃SO₃H and 1 M Pb²⁺ the conductivity is 0.193 Ω^{-1} cm⁻¹ and at 2 M Pb²⁺ the conductivity is 0.160 Ω^{-1} cm⁻¹. The maximum solubility of lead, 2 M Pb²⁺, is at approximately 1 M CH₃SO₃H. [24] At this concentration, the theoretic specific capacity of the electrolyte is 53.6 Ah 1^{-1} .

There have been three soluble flow cell configurations, with electrode surface areas of 2, 64

and 100 cm². The first reported flow battery was built with 1 x 2 cm electrodes supported in a polypropylene housing. The inter-electrode gap width was varied between 40 and 160 mm and was filled with 1.5 M Pb²⁺0.9 M M CH₃SO₃H electrolyte flowing at 20 mm s⁻¹. The specific capacity of electrolyte at this concentration is 40.2 Ah l⁻¹. Several different electrode materials were used; the best was found to be pressed nickel foam for the negative electrode and RVC for the positive electrode. Plots are presented showing cell discharges from 20 mA cm⁻² up to 100 mA cm⁻². However, the coulombic efficiency depends on the current: at 20 mA cm⁻² it is 85 %, but at 100 mA cm⁻² it is 50%. The cell voltage also decreases from 1.57 V to 1.26 V at 100 mA cm⁻². [54]

The 64 cm²cell was a general-purpose electrochemical reactor; several set-ups were used, including bi-polar operation. Galvanostatic tests were carried out at current densities up to 100 mA cm⁻². When used as a mono-polar cell with RVC electrodes for 25 cycles (11.6 Ah discharge), the failure mode was PbO₂sludging. With carbon felt as the posivite electrode, the cell cycled for 14 cycles (6.3 Ah discharge) until failure under the same mode. During bi-polar operation, the electrodes were nickel foam and reticulated vitreous carbon (RVC) for negative- and positive-end electrodes respectively and a planar carbon-HDPE (high density polyethylene) composite bi-polar electrode. The charge and discharge voltages were 3.7 V and 3.4 V at 20 mA cm⁻². The cell resistance was 0.63 Ω ; during charge this was the limiting factor in the cell. During discharge, the reaction kinetics or mass transport were limiting. The failure of the bi-polar cells occurred after 12 cycles (5.4 Ah discharge) and was due to the breakdown of the bipolar electrode, which was 1 mm thick RVC on Polytetrafluoroethylene (PTFE) support, or 1 mm thick RVC on Toray carbon support. [76]

The 100 cm² battery was tested under several flow regimes, with different electrode materials and with and without electrolyte additives. With carbon polymer composite electrodes and RVC granules on the surface, and 1 g dm⁻¹ligninsulphonic acid, the cycle life was shown to be 126 cycles with charge efficiency of 67 % and voltage efficiency of 77%. Carbon-HDPE composite electrodes give 100 cycles with charge efficiency of 91 % and voltage efficiency of 81 %[76]

The failure modes of these flow cells are related to short-circuiting between the two electrodes from either: 1) Pb dendrites forming between the electrodes; 2) PbO₂ sludging at the bottom of the electrolyte chamber; or 3) PbO₂ creep as a result of well-adhered deposits growing over the cell components. [76] Some of these have been addressed via the introduction of additives to the electrolyte. Sodium ligninsulphonate was found to be an effective levelling agent to improve the lead deposits, however the three inorganic ions used (Ni(II), Fe(III) and (Bi(III)) did not offer further improvements. [25] In later studies, 5 mM hexadecyltrimethylammonium cation, $C_{16}H_{33}(CH_3)3N^+$ was used to improve the negative deposit. [55] These batteries are at very low-technology readiness level (TRL) of around 2 or 3. Therefore there is scope for further improvement of these cells for several applications; load-levelling is cited as the target application. HEVs may be a future application as the specific current density is of the same order of magnitude as the most promising bi-polar battery. [60] The number of cells stacked (the battery voltage) must be increased significantly in order to achieve the required power for HEV applications.

2.8 Novel designs: conclusions

2.8.1 Materials

Most of the novel designs described here have been made possible by the use of novel materials. Polymers, carbons and ceramics (Ebonex®) have all been used and some display corrosion-resistant characteristics. The most corrosion-resistant materials appear to be: the composite used in the bi-polar battery; [60, 62] and carbon, as used in the UltraBattery (for part of the negative electrode) and in the soluble lead acid flow cells (for both positive and negative electrodes). [38, 76] However, when used as a bi-polar electrode, RVC on carbon and PTFE caused failure. [76] Materials which have not been demonstrated to be corrosion resistant at either electrode include: Ebonex®, lead and CDPE.

2.8.2 Performance: compare reported data and evaluate in comparison to HEVs

Demonstration in an HEV has been achieved with only one of these novel designs: the UltraBattery. [38][9] This 144 V system was operational over 100 000 miles in 9 months. Aside from this, there are no other novel designs which have TRL above 5, and the batteries at this level pose large questions for development. In order to achieve suitability for HEVs, these designs must demonstrate: high enough voltage [62, 40, 32, 76]; suitable operating characteristics [36, 76]; life cycles (all except the UltraBattery). Three designs show interesting performance characteristics: The 42 V bi-polar battery provides 0.56 A cm⁻² of electrode; and the Atraverda design passes the IEC 896-2 standard; the specific capacity of Karami's bipolar battery is 198 Ah kg⁻¹, which is the highest reported value for all the batteries examined in this paper.

2.9 Novel Materials

2.9.1 Carbon

The suitability of carbon for use as an electrode structure material in conventional lead acid batteries has been debated for some time. Furthermore, among those who do consider it suitable there is disagreement over whether a protective coating is required. Part of the debate stems from the wide variety of carbon forms. Table 10 lists the origin of the carbons tested in the literature. There are five carbons, of differing origin and geometry, including: RVC; two pitch-based foams, derived from naphthalene and petroleum; a carbon honeycomb, made from recycled paperboard; and a natural graphite punched sheet. There is large variance in electrochemical, mechanical and electrical properties. Electrical conductivity has been reported as varying from 1.2 S cm⁻¹ for reticulated vitreous carbon (RVC) [22] to 20 S cm⁻¹ for carbon foam [6] and 103 S cm⁻¹ for the graphite foams. [28] Density is reported as 0.048 g cm⁻³[22], 0.3 g cm⁻³[7] and 1.1 g cm⁻³[23]; and the surface area varies from 18 [22] to 89 cm² cm⁻³[7].

Type of carbon	Manufacturing method	Composition	Reference
Carbon honeycomb	Corrugated paperboard from waste packaging were stacked and glued at the outer edges using liquid-phenol-formaldehyde resin CELLOBOND® J2027L and Phencat 382 in a weight ratio of 100:5. After curing for 5 h at 60 °C, more glue was applied to the enitre block including ethanol in a ratio of 100:5:20 and cured again for 24 h at 60 °C. Electrodes were cut from this block, and then dried by heating in air from 25 °C to 195 °C at a rate of 12 °C h ⁻¹ . Carbonisation of three batches was conducted via a temperature increase from 200 °C to 650-700 °C at 120, 90 and 60 °C h ⁻¹ then up to 1000 °C at 480, 420 and 300 °C h ⁻¹ respectively.	Corrugated paperboard from waste packaging coated in liquid-phenolformaldehyde resin CELLOBOND® J2027L, Phencat 382 and ethanol.	[34]
Natural graphite sheet	m M/s Graphite India Ltd. Punched into grids.	Flexible graphite sheets. High quality natural graphite flakes without binder.	[23]
Petroleum- pitch-based carbon foam	Polyeurethane foam was used as a template. Dipped in slurry for 3 minutes, passed through rollers, dried then heated to 450 °C in nitrogen and soaked for 2hrs. Cooled, then oxidised at 0.1 °C min-1 up to 350 °C in an air flow of 0.8 m ³ hr ⁻¹ then carbonised at 1000 °C for 3 hours in argon.	Petroleum-derived pitch, ground and mixed with 2 wt.% organic additives (binder, thickener and suspension agent) and 35 wt.% water to form homogenous slurry. Polyurethane template has become part of the foam.	[7]
Synthetic pitch-based graphite foam	Pitch heated in Al pan at 1 °C min ⁻¹ under 1000 psi until full carbonisation at 1000 °C. Graphitisation was then achieved with heat treatment to 2800 °C.	Mitsubishi ARA24, meso-phase, napthalane-based synthetic pitch.	[28]
RVC	ERG Inc.	-	[22, 14]

Table 10: Carbon materials used as battery electrodes and manufacturing processes.

2.9.2 Cyclic Voltammetry

Cyclic voltammetry is extensively used as an analytical tool for assessing grid material stability in the potential operating range of lead acid batteries. The technique provides a rapid assessment of oxidative and reductive processes over a range of electrode potentials and can help screen materials prior to longer-term stability tests. The reaction potentials have been determined via this method: the equilibrium potential for the Pb \leftrightarrow PbSO₄reaction of solid lead electrodes in 4.5 M H₂SO₄ is -0.36 V vs. SHE [7] [28] (-0.35 V vs. SHE in 5 M H₂SO₄ [69]) and for PbO₂ \leftrightarrow PbSO₄ it is 1.74 V vs. SHE [7] and 1.73 V vs. SHE [28]. Hydrogen and oxygen evolution begins to occur at roughly -0.59 to -0.76 V vs. SHE [7] [28] [14] and at 1.7 to 2.2 V vs. SHE [7][14][21][28]respectively. The potentials are plotted in figure 3.

A suitable alternative electrode material would be electrochemically stable at the lead and lead dioxide equilibrium potentials, and have similar or higher gas evolution overpotentials. Electrochemical stability is indicated on cyclic voltammograms by an absence of current at the relevant potential.

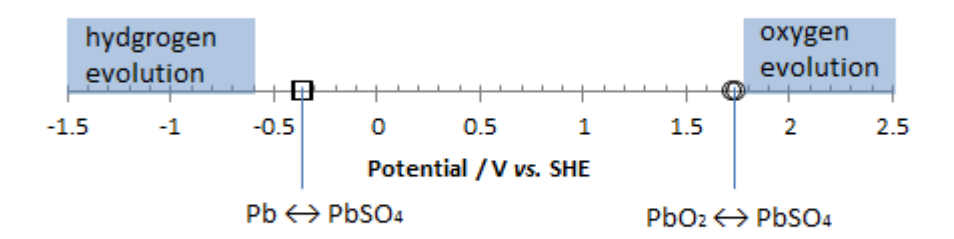


Figure 3: Operating potentials for the lead acid battery. The equilibrium potentials for the lead to lead sulphate reaction and the lead dioxide to lead sulphate reaction and the hydrogen and oxygen evolution reactions are shown. The electrolyte is 1 M H₂SO₄,[14] 4.5 M H₂SO₄,[28] [7] 5 M H₂SO₄, [69] and 1.28 g cm⁻³ H₂SO₄.[21]

Figure 4 presents voltammograms of a selection of carbon materials over the potential range associated with the lead-acid positive and negative electrodes. It is clear that the different carbons exhibit different electrochemical responses. The onset of hydrogen evolution differs between materials by approximately 470 mV between samples, and oxygen ranges over 400 mV. The potentials noted here correspond to reduction and oxidation currents of 1 mA cm⁻² for hydrogen and oxygen evolution respectively. The earliest hydrogen evolution is exhibited by natural graphite shows at circa -0.61 V vs. SHE while petroleum-pitch-based carbon inhibits hydrogen evolution until circa -1.08 V vs. SHE. The behaviour at positive potentials is different. The synthetic-pitch-based carbon evolves oxygen at the lowest potential, 1.73 V vs. SHE, and the highest is the petroleum-pitch-based carbon at 2.13 V vs. SHE. In addition, several materials including the natural graphite show some hysteresis in the voltammetric response, possibly due to capacitance effects; and the synthetic-pitch-based graphite exhibits some quasi-reversible redox activity at positive potentials.

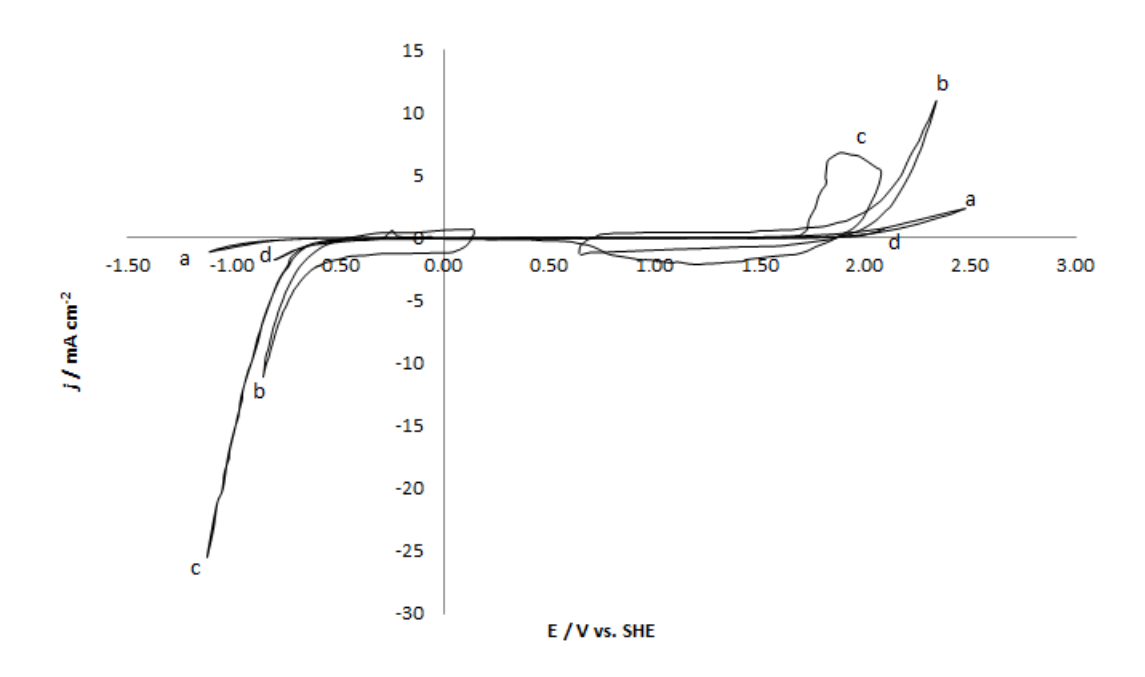


Figure 4: Cyclic voltammetry of various carbons over the lead-acid battery operating potential range. First scan is shown. Electrolyte and scan rate in parentheses. a Petroleum-pitch-based carbon foam (4.5 M H₂SO₄, 5 mV s⁻¹) [7], b Natural graphite (4.5 M H₂SO₄, 5 mV s⁻¹) [23], c Synthetic-pitch-based graphite foam (4.5 M H₂SO₄, 5 mV s⁻¹) [28], d RVC (5.3 M H₂SO₄, 1 mV s⁻¹) [22].

The petroleum-pitch-based carbon foam (figure 4 a) shows the lowest gas evolution rates of all the materials. It also has the lowest hysteresis. This scan range is the widest, showing an oxidation current beginning at 2.13 V vs. standard hydrogen electrode (SHE) and a reduction current at -1.08 V vs. SHE. There are no currents flowing at or near the battery operating potentials (of -0.36 V vs. SHE and 1.74 V vs. SHE), suggesting suitability of this material for a lead-acid battery application. No additional scan numbers are reported so behaviour during cycling is unknown. [7]

The natural graphite sheet (figure 4 b) begins hydrogen evolution at the lowest overpotential at -0.61 V vs. SHE. Oxygen evolution begins at 2.03 V vs. SHE. These values imply that this material may be suitable for use as either electrode, however the large hysteresis suggests that this material has high capacitance which would produce negative effects during battery operation. Also, the authors report that the electrolyte penetrates into the graphite and causes mechanical degradation. [23]

The synthetic-pitch-based graphite (figure 4 c) shows an oxidation current beginning at 1.72 V vs. SHE and a reduction current at -0.68 V vs. SHE. At the negative electrode, this reduction current would not interfere with the battery reaction, and no hysteresis is shown, suggesting suitability for the negative electrode. However, at positive potentials, the oxidation current occurs at the battery reaction potential. It also rises quickly; for example the positive current is 1.5 mA cm⁻² at 1.73 V vs. SHE and 6.7 mA cm⁻² at 1.86 V vs. SHE. In addition, as the cycle number increases, the oxidation current commences at a lower overpotential. These behaviours rule out suitability of this material at the postive electrode. The open shape of the curve is attributed to intercalation of H_2SO_4 into the interstices of the graphite sheets, with material

shedding as a result. The compounds are reported as:

$$C_x + 3H_2SO_4 \rightarrow C_x^+ HSO_4^- 2H_2SO_4 + H^+ + e^-$$
 (3)

[28].

The RVC electrode (figure 4 d) begins hydrogen evolution at -0.71 V vs. SHE and oxygen evolution is not present in this scan range, up to 2.09 V vs. SHE. According to the first scan, this material looks suitable for use in both electrodes. However, as the cycling progresses towards 50 cycles, at negative potentials, the reduction current more than doubles at the highest overpotential. Despite this trend, the current is still very low, and within tolerable limits. This material may still be useful at the negative current. With cycling at the positive potentials, there is no significant degradation of behaviour. This data suggests that the material is suitable for use at both electrodes. [22]

Several of these authors go on to use these materials in small-scale demonstration cells. This is where the accuracy of the predictions based on voltammetry are revealed. The petroleum-pitch-based carbon foam looks suitable for both electrodes, and is used in a cell as both electrodes, but the battery fails after one cycle due to positive electrode degradation. [7] Even when used only as the negative electrode, the performance is underwhelming. [6, 5] The synthetic pitch-based foam appears to be unsuitable for the positive electrode, and indeed when it is used in a demonstration cell for both electrodes, it is the positive which fails. [28] Neither the natural graphite sheet nor the RVC materials are used in their bare forms in demonstration cells, despite the fact that the RVC appears to be suitable at least for the positive electrode. [22, 23] The results of the demonstration-cell experiments are discussed in more detail below.

Coated carbon In order to mitigate the problems associated with electrolyte penetration, material degradation or lack of adhesion of positive active material, several authors use a coating on the carbon substrate. [34, 53, 12, 13, 22, 11, 23] A summary is presented in table 11.

Natural graphite sheet. Both the oxidation currents at potentials above 2 V vs. SHE and the hysteresis effects have been reduced by coating the graphite electrodes with Pb and then Pb/PANI (polyaniline). After 20 cycles, both substrates now exhibit a reduction current that was not present at cycle 1. The lead oxidation current has increased significantly more than the graphite/Pb/PANI; the author suggests that the PANI offers more protection than lead alone, however, the author offers no explanation for this conclusion. It could also be attributed to the higher electrical resistance of the PANI coating. In fact, the reported electrical resistance of the grids is indeed high at values between 27-60 Ω depending on state of charge. [23] A different study described a similar the peak size difference between different substrates, but attributed this phenomenon to different substrate surface areas. This study compared electrochemical peaks of Pb electroplated onto RVC and metallic Pb, and attributes reduced current peaks on the platinum coated sample to the platinum coating reducing the real surface area of the sample. The small peak at 1.6 V vs. SHE is explained as evidence of PbO₂ cracking due to the potential sweep going above 2.2 V vs. SHE. [14]

Substrate		Layer	1 / μm		Laye	er 2 / μm	Reference
Graphite	Pb	50	Electroplated	PANI	5	-	[23]
RVC	Pt	-	Potential cycling in 0.5 M H ₂ SO ₄ 3% chloroplatinic acid from -240 to 1000 mV vs. SCE for 50 minutes.	Pb	-	Cathodic electroplating in acetate solution, ambient temperature, 1.5 to 2.0 mA cm ⁻² for 20 - 30 minutes.	[14]
RVC	Pb	-	Electroplating from alkaline acetate bath.	-	-	-	[11]
RVC	Pb	10 to 15	-	-	-	-	[11]
RVC	РЪ	Positive electrode: 60; Negative electrode: 20.	-	-	-	-	[13]
RVC	Pb-Sn 1 wt. %	Positive electrode: 200 to 300; Negative electrode: 80 to 120.	Galvanostatic electroplating from fluoroborate bath.	-	-	-	[22]
Carbon	Cu (grid ends only)	5	Electroplating from 1 M CuSO ₄ 0.5 M H ₂ SO ₄ .	Pb-Sn 2 wt. %	100	Electroplating from lead phenolsulphonate $200~{\rm g~dm^{-3}}$, tin phenolsulphonate $6.35~{\rm g~dm^{-3}}$, free phenolsulphonic acid $40~{\rm g~dm^{-3}}$, sodium ligninsulphonate $0.5~{\rm g~dm^{-3}}$.	[34]

Table 11: Coatings applied to carbon to provide corrosion protection.

2.9.3 Batteries

A 2 V 24 Ah commercial cell was assembled with graphite electrodes, coated in 50 μm lead and 5 μm PANI, then pasted and formed. The battery's specific capacity was close to 40 Wh kg⁻¹ at the C5 rate. An initial voltage drop during discharge was attributed to high electrical resistance. After 50 cycles, active material had shed from both electrodes due to exfoliation of the electrodeposited lead layer. [23]

Carbon foam was used to build a battery which was directly compared to a similar one with lead sheet electrodes. The capacity of the carbon battery was 80 mAh compared to 72 mAh for the lead sheet. A PSoC cycling regime was used which was well suited to the carbon.[6] X-ray diffraction (XRD) showed that the positive electrode was not converting PbSO₄ to PbO₂ during charge. [5]A graphite 2 V pasted battery failed to perform more than one cycle at 10 mA due to the performance of the positive electrode; most likely failure occurred because of lack of adhesion of positive active mass (PAM) to the current collector. Intercalation of H₂SO₄ into the carbon was proposed as causing the failure. This was confirmed by experiment on a small three-electrode cell of pasted-graphite electrodes; the positive electrode was the limiting electrode [28]

Coated carbon batteries The clearest argument for a coating on the carbon substrate comes from the battery performance. Table 11 and figure 5 together show the materials which were used to coat the novel carbon substrates and the reason for the coatings. Regardless of the coating composition, the thickness of the coating determined the cycle life, and Figure 4 shows this linear relationship clearly. A battery using an uncoated carbon foam lasts for roughly 30 cycles [5]; coatings with lead or lead-tin increase the cycle life up to a maximum of 500 cycles with a 300 µm lead coating on the positive plate and 120 µm on the negative. [22] Including PANI in the lead coating on a graphite sheet has no effect on cycle life, this battery also fails at 30 cycles [23].

Figure 5 tells us two things: that 1) if the cyle life is proportional to the thickness of the lead layer, then a lead grid would offer the longest cycle life and 2) the active material adheres best to lead; any alternative substrate must be compatible with the active material.

Pitch-based carbon foam was used as negative current collector in a battery. The results were improved partial state of charge (PSoC) cyclability in comparison to the full-lead control electrode, perhaps due to increased specific surface area (cm²cm⁻³) and interconnectivity of the carbon ligaments. But oxygen evolution occurs at 0.6 V, too low for the Pb \rightarrow PbO₂ reaction to begin, rendering it unsuitable for positive electrode application. Utilization of the negative plate is ca. 60 % and charge acceptance up to 72 %. [7, 6]

Czerwinksi has built a series of carbon-based batteries, including a battery with Pb/RVC pasted negative electrodes and a charge capacity of 150 Ah kg⁻¹.[11, 12]However, findings show that when comparing batteries with typical positive electrodes but either bare or coated RVC negative electrodes the results are similar: the problems arise from the positive electrode. This is linked to corrosion. The most advanced battery in this series of papers presents cycling of a battery with both positive and negative Pb-RVC electrodes. A 2 V 2 Ah cell gave 24-25 Ah kg⁻¹ at the 20-h rate and gave 105 cycles.[13]However, a 2 V 40 Wh kg⁻¹ PANI-Pb-graphite battery failed by active material shedding from both positive and negative electrodes after 30 cycles.[23] Another battery used a 100 micron lead/tin alloy coating on both electrodes. After surviving 191 deep cycles, the lead/tin coating was completely corroded and the carbon substrate structure

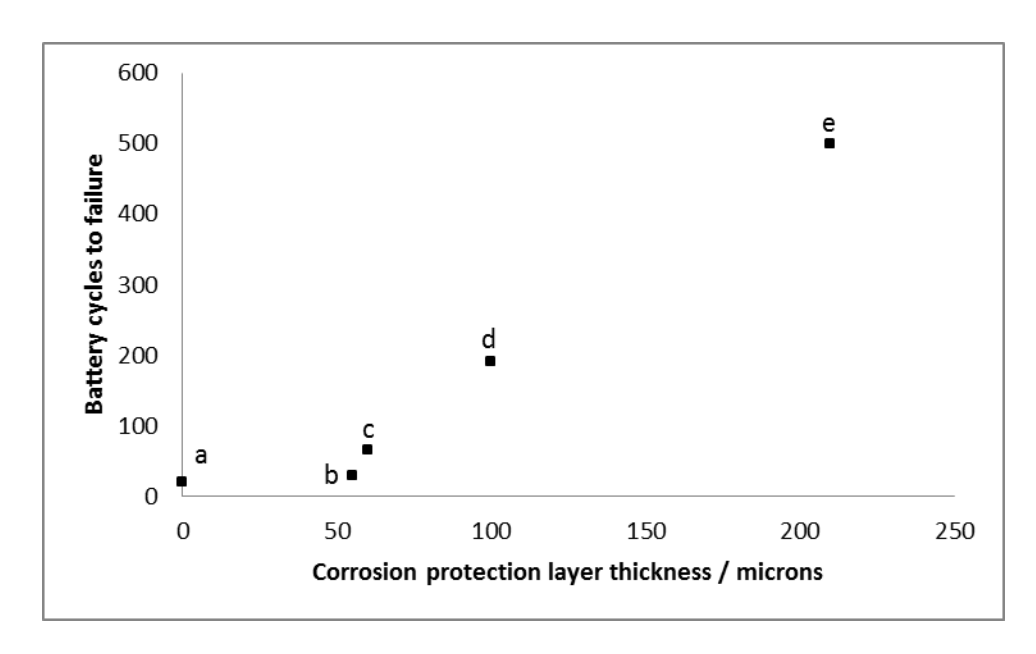


Figure 5: Carbon-electrode battery cycle life as a function of thickness of carbon-coating corrosion protection layer. a [7], b [23], c [13], d [34], e [22]

was damaged and lost mechanical integrity. [34]

Electrical resistance and impedance As expected, RVC has a much higher impedance than lead. This was measured by electrochemical impedance spectroscopy (EIS) and plotted on a Nyquist plot. The high impedance is attributable to the lower conductivity of RVC. In the same study, the impedance of fully charged and fully discharged plates was also measured. Comparing the values reveals that the impedance is affected more by the state of charge than by the grid material. When the plates are fully charged, the most significant part of the impedance is attributable to the diffusion across the pores; when the plate is fully discharged this becomes insignificant as the lower frequency impedance (associated with the carbon) becomes dominant. [5] This suggests that the electrical conductivity of the carbon, while lower than lead, is still higher than the lead sulphate and lead oxides present after discharge. This is supported by another study of a lead-coated carbon-honeycomb battery during cycling. The ohmic resistance of the positive electrode increased with progressing cycles. The author suggests either the lead sulphate is accumulating or that a corrosion layer at the interface between current collector and the active mass is forming with cycles. Finally, tear-down analysis revealed this was not the case, but that severe corrosion of the positive electrode occured through the lead-tin coating to the carbon. [34] Contradicting this however, is a different study which describes typical changes of PAM during cycling and suggests that lead sulphate would not accumulate in the PAM. [51]

2.9.4 Summary

Carbon can take many forms. The most discussed for lead-acid battery applications are graphite and vitreous carbon. Both types can be formed into high – surface area geometries: foams, reticulated. There are disagreements in literature about suitability, and whether a protective coating is required. The clear conclusion from figure 5 is that there is in fact a linear relationship between lead coating thickness (on both electrodes) and cycle life. The electrical resistance of

carbon has less of an effect on plate impedance than the DoD of the battery.

2.10 Conductive polymers and ceramics

Polymers and ceramics have been investiagetd for use as either a grid substrate or a coating. The reasons for use are either the density (significantly lower than lead), or the corrosion resistance (again, lower than lead). The selected materials have sufficient electrical conductivity: the polymers include polyaniline, acrylonitrile butadienestyrene (ABS), carbon-doped polyethelyne and the ceramics are barium metaplumbate and glass.

An unspecified polymer was used as a substrate in a composite grid: polymer core, conductive starting layer, copper, lead. The grid composed of these fibres knitted into a mesh. Batteries made from these electrodes showed increased negative active material utilisation and capacity over EV plates [64]. Conductive (carbon-doped) polyethelyne was used as a bi-polar electrode material. Four different electrode types were used with cycle life ranging from 45 – 140, and 150-198 mAh g^{-1} and 59.7-83.3 mW g^{-1} . [32] Polyaniline is a conductive polymer (electrical resistance of 10 ohm m⁻¹), which was grafted onto the surface of polypropylene from aniline solution by adding ammonium persulphate. Negative electrodes were constructed by using the polypropylene base, polyaniline, copper, 1 mm thick lead. Same oxidised in H₂SO₄ then immersed in polyaniline. A cell was built 2 negative plates, 1 positive plate, and tested over 100 cycles at 150 mA. The capacity fade was significant: from 40 Ah kg⁻¹ to 20 Ah kg⁻¹ after 100 cycles. [57] PANI was again used as a layer in a corrosion-protecting coating on lead/carbon electrodes positive and negative electrodes. [23] These electrodes had a resistance of $0.027 - 0.06 \Omega$ depending on state of charge. A new battery design replacing the lead negative electrode with a polyaniline electrode was investigated by voltammetry and half cell reactions. Negative electrode capacity of 240 mA h g⁻¹ and full cell estimated energy 100 W h kg⁻¹. [20] Another conductive composite uses ABS as a substrate for copper (10 micron) then lead (100 micron) electrodeposition and then coated with polyaniline for corrosion resistance. A battery was cycled which yielded 50 Wh kg⁻¹ at the C/5 rate for 120 cycles with little capacity degradation. [43]

Barium metaplumbate, BaPbO, is a conductive perovskite ceramic, resisitivity 8.3 x 10 $^{-4}\Omega$ cm[49] which has been analysed for suitability at lead-acid battery operating potentials. (Kao, Haberichter, & Patel, 1994) Suitability as a corrosion resistant coating was confirmed via float-life tests, where BaPbO coated Pb-Ca-Sn grids maintained a higher normalised reserve capacity than control Pb-Ca-Sn grids. Grid creep was less for the BaPbO grids and cross-sectional micrographs reveal less inter-granular corrosion. However, it can be attacked by sulphuric acid, and requires a protective lead coating to survive longer than 10 weeks from loss of grid material. [31] BaPbO has been used as a substrate for lead deposition, and via voltammetry its suitability for use as a lead-acid battery electrode material has been established. [49]

Glass fibres were coated with lead and made into a mesh size 5x3 mm. A battery with one positive plate and two negatives was built, resulting in active material utilisation becoming between 5-50 % greater than conventional gravity-cast grids, depending on temperature and discharge rate. Cycle life was 108 cycles. [74]

Non-graphite foam as electrode substrates which performed better than graphite foam, but still poorly in comparison to conventional batteries. Both negative and positive electrodes were limiting and suffered from formation of barrier layers, corrosion layers and shedding of active

2.11 Metals

Several titanium-based materials have been investigated. Titanium may be suitable for negative electrodes only as the overpotential for TiO_2 formation from surface products is -0.5 V vs. SCE; below this potential, current flow is inhibited by this passive film until the oxygen evolution potential is reached at ~2.2 V. [68] For the purpose of a hybrid supercapacitor, PbO₂ was electrodeposited onto Ti/SnO₂ electrode. The electrode was prepared by thermal decomposition, SnO₂ doped with 5% Sb. The PbO₂ thin film was pulsed at 25 mA cm⁻² for 0.01 s then relaxed for 0.1 s for 2.75 h until 60 μm was formed. The solution was 0.5 M Pb(NO₃)₂. This was used as the positive electrode, and the negative electrode was RVC. The resulting device provided $32.3~\mathrm{Wh~kg^{-1}}$, $200~\mathrm{mA~g^{-1}}$ for $4500~\mathrm{deep}$ cycles .The high-power and long life was attributed to the pulse deposition method of the PbO₂ and the stability of the Ti/SnO₂ current collector in H₂SO₄ solution. [79] Tin dioxide (15 μm) was applied to titanium substrates by sputtering, and shown to have similar electrochemical properties to a lead substrate when pasted with active material. Corrosion resistance was verified by SEM after 100 cycles. Deep discharge (below 0.5 V vs. Pb/PbSO₄) initiated tin dioxide dissolution in sulphuric acid. [35] The operating potential values of Ebonex are within the potential limits for lead-acid batteries. Titanium oxides of the Ebonex stochiometry have been used as bi-polar electrodes by Atraverda. [40]

Lead coated onto aluminium has been shown to prevent corrosion. The electrodeposited lead coating with thickness of between $100-500~\mu m$ increases useful life of positive electrode and prevents scaling of active lead dioxide mass through grid destruction [78]. Tin oxide (pyrolytic, was prepared by spraying tin chloride solution onto the Al substrates, then heated to 400 °C), thickness of around 1 μm is enough to protect aluminium from chemical degradation. This was established by plating Al onto glass plates, then immersing in acid until completely dissolved. [59]

Copper requires protection from the electrolyte, this is achieved by using 20-30 µm thick layer of electrodeposited lead. As this is the negative electrode active material, it must be ensured that it does not participate in the reaction, become consumed and expose copper to the electrolyte. This would result in; increased rate of hydrogen evolution, dissolution of copper and deposition onto the NAM surface. Copper is not used as substrate because there is no suitably efficient protective plating due to the tiny amounts of copper tolerable in the electrolyte before causing deposition. They propose to use a two-layer coating, the first of lead, the second of lead-tin-zinc alloys. These had been previously electrodeposited with boron fluoride electrolyte (BFE), now nitrilotriacetate electrolyte (NTA) is used. The lead deposition with NTA produces smaller lead crystals (1-2 µm instead of 10 µm with BFE) and allows a coating of lead of 5 µm instead of 20 µm, it also shows increased corrosion resistance. The lead-tin-zinc alloy also showed no porosity at 5 μm. Batteries constructed using this as negative electrodes have been constructed and tested, and show long service life. [41] Copper has been used as a negative electrode material in two major industrial applications. Exide's submarine batteries use CSM (copper stretch metal) negative plates [70] [33] and the BEWAG battery in Berlin had copper negative grids. The BEWAG battery was built in 1986 for West Berlin but dismantled after the reunification of Germany. At the time it was the largest in the world at 17 MW, 14 MWh. [70] Copper plates have improved

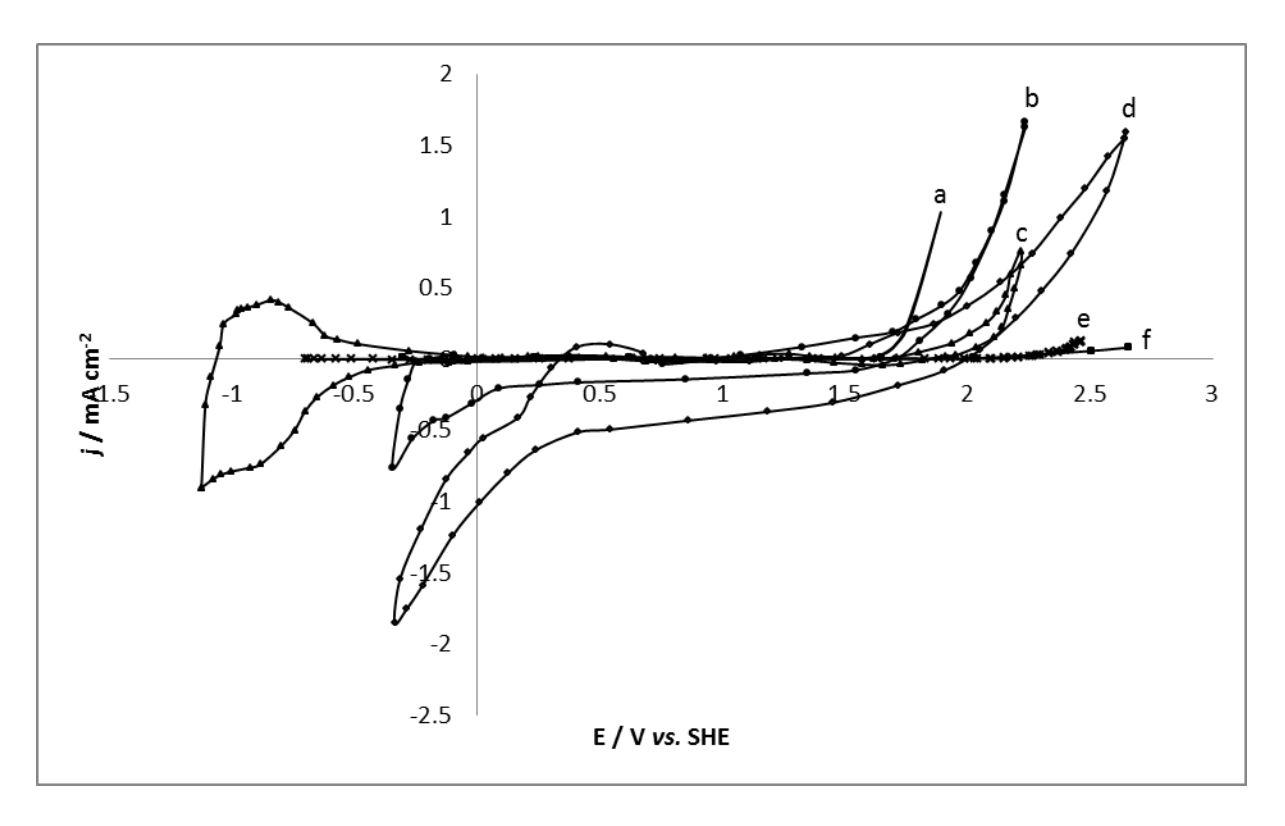


Figure 6: Cyclic voltammetry of various metal oxides over the lead-acid battery operating potential range. Electrolyte in parentheses. a $TiRuO_2(1.29 \text{ sp. gr. } H_2SO_4)$ [26], b $NbSi_2$ (1.365 sp. gr. H_2SO_4) [30], c Ebonex (1.0 mol dm⁻³ H_2SO_4)[73], d $TiSi_2$ (1.365 sp. gr. H_2SO_4) [30], e BaPbO (0.5 M H_2SO_4) [49], $TaSi_2$ (1.365 sp. gr. H_2SO_4) [30]

volumetric energy density, longer service life and resistance to shock and vibration [33] The conductive properties of copper have also been utilised in composite electrodeposited grids. [75]

2.12 Summary and conclusions

While the voltammetry may suggest suitability of novel materials, including carbons, to be used as novel grid materials, the real proof of suitability is in demonstration batteries. The success of batteries built and tested has been low. The novel-material battery with the best reported energy density is [13] 24-25 Ah kg⁻¹ but the longest cycle life was 191 deep cycles. [34] This value for energy density is an improvement on a conventional spiral-wound VRLA battery which offers 17.3 24-25 Ah kg⁻¹(Cyclon D cell). Kirchev did not report the energy density of his 3 Ah battery. The grid weight reduction problem has been investigated by several authors, and [13] offers a robust study into carbon electrodes, however the commercialisation of this concept is yet to be seen. Many non-lead grid materials have been utilised in laboratory studies but each has its limitations. The UltraBattery offered good performance in a demonstration vehicle, but has not yet been commercialised. The only novel-material battery to be commercialised has lead-coated copper electrodes.

Direct comparison of the battery types is not possible due to the lack of reported data (for example, cycle life but not energy density [34]). Often cycle life values, the most contentious point, have different definitions in different papers, or are not tested for at all. Also, the test regimes used to generate these values vary widely between papers; as shown in tables 5 and

	Operable voltage range $/$ V $vs.$ SHE			
Material			performance	Reference
	Lower negative limit	Upper positive limit	characteristics	
D			$18 \; {\rm cm^2 \; cm^{-3}}$	
Reticulated			$0.048~{ m g~cm}^{-3}$	
vitreous carbon	-0.5	2.1	1.2 S cm ⁻¹	[22]
(RVC) from	0.0		(bulk)	[]
ERG			200 S cm ⁻¹	
			(ligament)	
			Negative	
			electrode	
			current doubles	
			after 50 cycles.	
			No change to	
			positive current.	
			positive current.	
Graphite foam			$10^{3} {\rm S \ cm^{-1}}$	
(manufactured			180 W m ⁻¹ K ⁻¹	
1 '	-	2	$\frac{160 \text{ W m} \text{ K}}{200 \text{ cm}^2 \text{ cm}^{-2}}$	[28]
in-house, but similar to			0.6 g cm^{-3}	
			0.0 g cm	
ORNL foam)			$1.1~{ m g}~{ m cm}^{-3}$	
Natural graphite	-0.65	2	Hysteresis effect	
			with cycling	
Petroleum			$0.3~{ m g~cm}^{-3}$	
derived			0.5 g cm	
	-1	3.24	$89 \text{ cm}^2 \text{ cm}^{-3}$	[7]
pitch-based carbon foam			20 S cm ⁻¹	
		0.1	20 5 CIII	[0.9]
Graphite / Pb	-	2.1	-	[23]
Graphite / Pb / PANI	-	2.2	-	[23]
RVC / Pb	-0.2	2	-	[14]
RVC / Pt / Pb	-0.4	2.2	-	[14]
Ebonex	-1	2.5	-	[73]
TiSi_2	-0.2	2.2	Hysteresis	[26]
			effects with	
			cycling	
$TaSi_2$	-0.2	2.7	-	[26]
$\overline{\text{TiRuO}_2}$	-	1.8	_	[26]
BaPbO	-0.6	2.5	-	[49]
	1	1	1	[L -]

Table 12: Summary of novel grid materials investigated for use in lead acid batteries showing the voltage range over which they are suitable for use and relevant performance characteristics and behaviours.

7. Both these problems would be solved if a standard test regime were widely adopted. The test regime should be thorough, application-relevant and industrially-trusted. The battery test regime which most fits this criteria is the PALC. My suggestion is to use this test regime in future battery development.

Therefore, it is difficult to predict the efficacy of different materials for this new application using the literature alone. Generally, the literature is encouraging: there is promise for using some form of carbon as an electrode material. Just how this will perform under HEV cycling must been seen from experiment.

3 Experimental

3.1 Reagents: Preparation of Chemicals, Solutions and Gases

All reagents, presented in table 13, were used as received from the manufacturers without further purification. All solutions were prepared using water from a Purite Ondeo 15 water purifier and unless otherwise stated were thoroughly deoxygenated with a vigorous nitrogen bubble stream for 3 minutes prior to experiments.

Chemical	Supplier	Purity
Lead Carbonate: PbCO ₃	Aldrich	-
Methanesulphonic Acid: CH ₃ SO ₃ H	BASF	-
Sodium Ligninsulphonate	Aldrich	-
Sulphuric Acid: H ₂ SO ₄	ReAgent	-
Bismuth (III) oxide: Bi ₂ O ₃	Aldrich	99.999 %
Tin(II) sulphate: SnSO ₄	Acros Organics	99 %

Table 13: Chemicals used during the project, including the supplier and purity.

3.1.1 Lead solutions

Lead methanesulphonate, $Pb(CH_3SO_3)_2$, was prepared as an aqueous solution, via the reaction of lead carbonate with methanesulphonic acid (equation 4).

$$PbCO_3(s) + 2CH_3SO_3H(aq) \rightarrow Pb(CH_3SO_3)_2(aq) + CO_2(g) + H_2O(l)$$
 (4)

Solutions were left for 24 hours to equilibriate to room temperature and filtered to remove insoluble carbonates prior to use.

3.2 Cyclic Voltammetry

3.2.1 Set-up

Voltammetric measurements were conducted and data recorded with one of the two apparatus set-ups:

- •A Princeton VSP Potentiostat with VSP software and a two chamber cell (figures 9 and 10)
- •An Autolab Potentiostat with Nova data collection software, in a three chamber cell (figures 7 and 8).

All experiments were carried out at 293 K \pm 2. The Luggin capillary, which separated the working and counter electrodes from the reference electrode, was placed 1 mm from the working electrode. The counter electrode was a platinum mesh of 50 x 50 mm. The reference electrode was a saturated calomel electrode (SCE). The scan rate was 25 mV s⁻¹unless otherwise stated, and the potential limits were -0.3 V vs. SCE to -0.8 V.

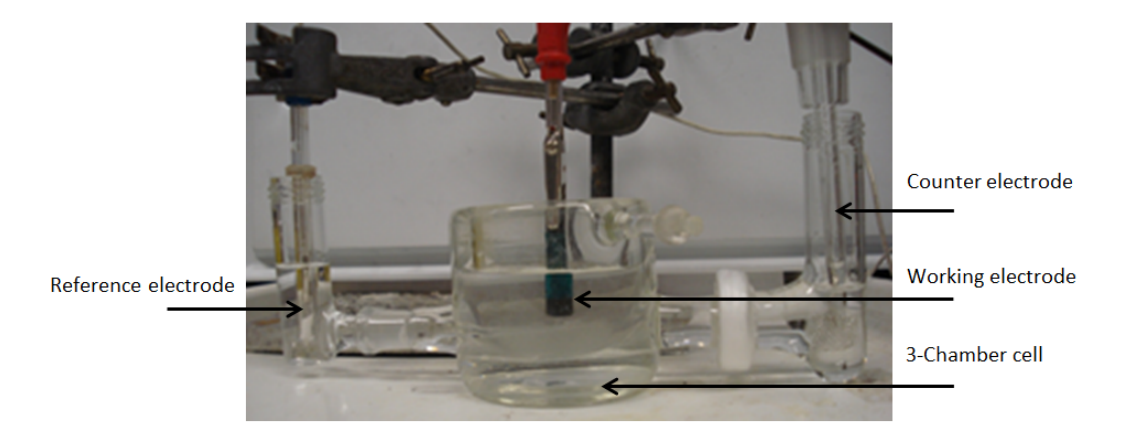


Figure 7: Photograph of the 3 chamber glass cell used in cyclic voltammetry, as connected to potentiostat. From left to right: reference electrode, working electrode, counter electrode.

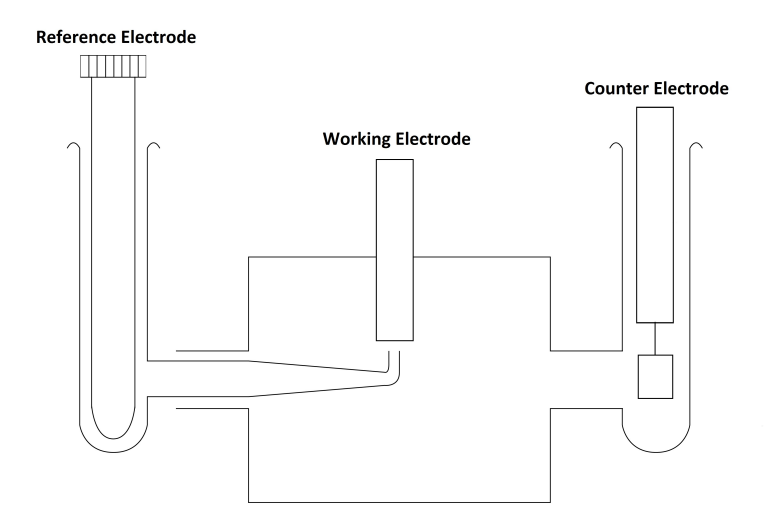


Figure 8: Schematic diagram of the 3 chamber glass cell used in cyclic voltammetry. Electrolyte used was 5 M $\rm H_2SO_4$.

3.2.2 Materials and electrolytes

The materials that were used as working electrodes during cyclic voltammetry include: titanium, nickel, copper, 304L steel, mild steel and carbon-polymer composite. With the exception of the carbon-polymer composite, which was supplied from Entegris, all other materials were supplied by TWI, the project sponsor.

The electrolytes used during the experiments are listed in table 14.

ĺ	$5~\mathrm{M}~\mathrm{H_2SO_4}$				
ĺ	1 M CH ₃ SO ₃ H				
Ì	6 mM Pb 1 M CH ₃ SO ₃ H				

Table 14: Electrolytes used during cyclic voltammetry, including concentration.

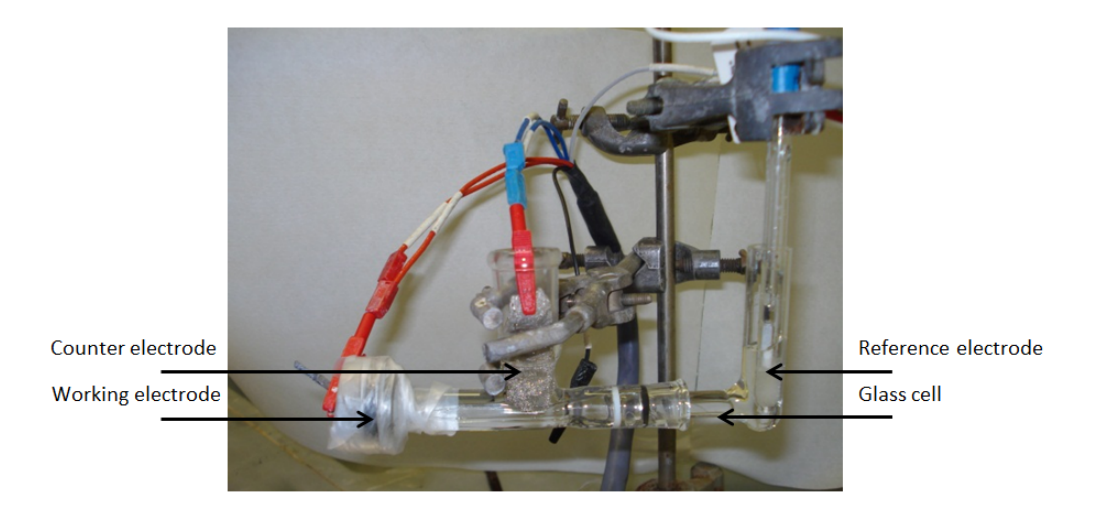


Figure 9: Photograph of the 2 chamber glass cell used in cyclic voltammetry, as connected to potentiostat. From left to right: working electrode, counter electrode, reference electrode.

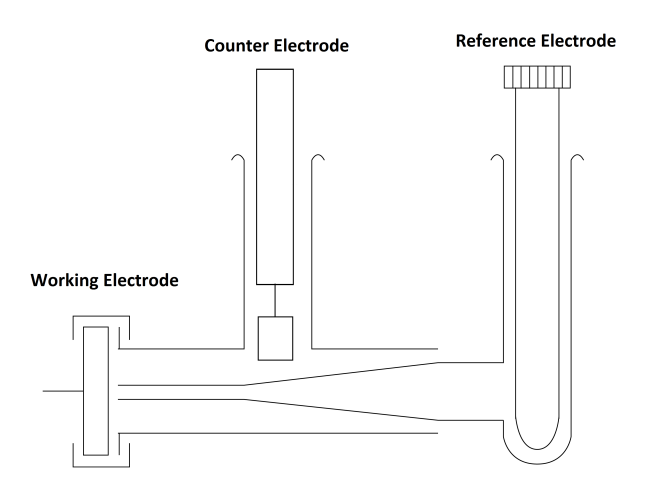


Figure 10: Schematic diagram of the 2 chamber glass cell used in cyclic voltammetry. Electrolyte used was 6 mM Pb 1 M $\rm CH_3SO_3H$.

3.2.3 Electrode preparation

For the three chamber cell experiments, the electrodes were prepared by cleaning with 800 grit silicon carbide paper, then rubbing with acetone. The surface area was defined with Cole Parmer Green Polyester tape (08277-28).

The two chamber cell electrodes were prepared in the following manner, an example of which is shown in figure 11. A small cross section (0.2 x 1 mm) of material was set in epoxy resin and mechanically ground then polished to 1 micron. The electrodes were first ground with 400 grit silicon carbide paper on Buehler polishing wheels, then 800, 1200 and 1400 grit paper in sequence. The final polishing was achieved with 1 micron diamond paste and a polishing wheel.

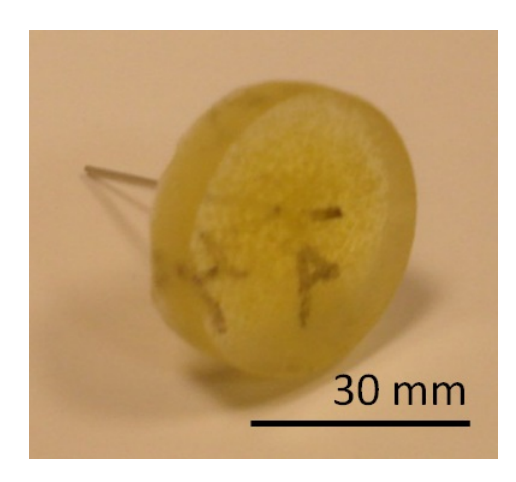


Figure 11: Typical resin-mounted electrode material as used in the two chamber cell during cyclic voltammetry.

3.3 Electrodeposition

3.3.1 Set-up

Electrodeposition of lead (shown in equation 5) was conducted with one of the two apparatus set-ups:

- •100 ml plating bath, with 10 x 10 mm carbon-polymer composite (Entegris) counter electrode, driven by a Princeton VSP Potentiostat
- •2000 ml plating bath, with 100 x 100 mm lead sheet (99.9 %, Goodfellow) counter electrode, driven by PAD 30 A Power Supply (shown in figure 12).

In both set-ups, the current density was a constant 50 mA cm⁻², the temperature was 293 K \pm 2 and the electrolyte was agitated with a magnetic stirrer.

$$Pb^{2+}(aq) + 2e^{-} \to Pb(s) \tag{5}$$



Figure 12: Electrodeposition bath, 2000 ml. 293 K \pm 2, magentic stirrer.

3.3.2 Electrodes and Electrolytes

During electrodeposition, three types of titanium mesh were used as electrodes, these are shown in table 15. The electrode dimensions were either 30 x 10 mm or 100 x 100 mm. The Fibretech mesh was manufactured at the required size; the Dexmet material was cut with scissors and the Goodfellow mesh was cut with tin snips. Unless otherwise stated, electrical connection was made with crocodile clips and then coated in MacDermid 45 Stopping-Off Lacquer. The laquer both insulated the electrical connections and defined the electrode geometric surface area as 1 or 95 cm² for each type of electrode. An example 100 x 100 mm Fibretech electrode, complete with electrical connection and lacquer is shown in figure 13.

The average surface roughness of the profile of the Dexmet materials is $3.72~\mu m$, as measured with Alicona surface imaging. An attempt was made to conduct BET (Brunauer-Emmett-Teller) testing on the fibres. This test involves nitrogen adsorbtion onto the surface of particles, and is commonly used for analysing powders. For example, lead oxide pastes, which are used as active material in lead acid batteries, have a BET surface area of 1.5 to 2.5 m²g⁻¹. [74] The minimum surface area which is measurable by this method is in the order of m²g⁻¹; these fibres do not have sufficient surface area to give a value in this test. The surface area is significantly below that of a powder.



Figure 13: Example of a 100 x 100 mm titanium Fibretech electrode, with electrical connection.

Before electrodeposition each electrode substrate was cleaned by first rubbing down with

acetone, then 5 % nitric acid, then deionised water. In addition, three samples underwent three different methods of surface cleaning: rubbing with acetone, submerging in an ultrasonic bath for 10 minutes, and exposing to a plasma field for 10 minutes.

The electrolyte was $1.5~\mathrm{M}$ Pb $1~\mathrm{M}$ CH₃SO₃H solution with $1~\mathrm{g}$ l $^{-1}$ ligninsulphonate throughout lead electrodeposition. For tin electrodeposition a solution of $0.05~\mathrm{M}$ Sn $1~\mathrm{M}$ methanesulphonic acid was used.

Goodfellow	Woven titanium mesh.	000 ANOSE 4004	Wire diameter: 0.23 mm.	Nominal aperture: 0.19 mm.	$60 \times 60 \text{ wires/inch. } 20\% \text{ open}$	area, twill weave.	0.088	1	Stiff.
Dexmet 1108		0000	Strand width:	0.025 mm Long	Way Diamond	length: 4.56 mm.	0.010	0.5	Flexible.
Dexmet 3020	Expanded titanium mesh.	AND SE	Strand width:	0.076 mm. Long	Way Diamond	length: 0.50 mm .	0.004	0.2	Flex
Fibretech	Melt-spun and sintered titanium fibre network.	must cov milat by variety is account.	Fibre diameter: 0.1 mm.	Fibre length: 5 mm.			0.15	4	Poor structural integrity, stiff.
Name (inlcuding manuacturer)	Electrode material.	SEM image	Material	dimensions			$\mathrm{Mass} \ / \ \mathrm{g} \ \mathrm{cm}^{-2}$	Thickness / mm	Comments

Table 15: Titanium meshes used as substrates during electrodeposition of lead, electrolyte composition 1.5 M Pb 1 M $\rm CH_3SO_3H$ with 1 g $\rm l^{-1}$ ligninsulphonate.

3.4 Amperometry

3.4.1 Set-up

The amperometry was performed using the two chamber glass cell shown in figures 9 and 10. An SCE reference electrode, and platinum mesh of 50 x 50 mm counter electrode was used. The AutoLab potentiostat with Nova software was used throughout to apply a constant, stepped potential and to record the response data. The temperature was 293 K \pm 2.

The applied potentials were in the range of -0.24 to -0.72 V vs. SCE for the negative electrode and 1.26 to 1.74 V vs. SCE for the postitive electrode. A charge potential was applied for 60 s, then a discharge potential of the same overpotential was immediately applied for 60 s. The response current was recorded, and the limiting current was noted.

Electrodes were carbon-polymer composite (Entegris) and were prepared by cleaning with 800 grit silicon carbide paper and rubbing with acetone.

Between experiments, glassware was rinsed thoroughly in deionised water and then acetone. The counter electrode was stripped of excess deposit by immersion in 1 M CH₃SO₃H and connected to a lead electrode and potentiostat, until the current reading dropped to 0 A. The counter electrode was then rinsed in deionised water and then acetone.

3.4.2 Electrolytes

The lead-methanesulphonic acid electrolytes used during amperometry are shown in table 16. The methanesulphonic acid concentration was a constant 1 M, while the lead concentration ranged from 0.010 M to 1.500 M. This is up to the maximum solubility limit for lead in methanesulphonic acid. [24] For half of the experiments, bismuth was present at a concentration of 10 mM. This concentration was similar to other additive concentrations used in the literature. [25]

	lyte Concentr	
Pb ²⁺	$\mathrm{CH_{3}SO_{3}H}$	Bi^{2+}
0.010	1.000	0.000
0.100	1.000	0.000
0.750	1.000	0.000
1.000	1.000	0.000
1.500	1.000	0.000
0.010	1.000	0.01
0.100	1.000	0.01
0.750	1.000	0.01
1.000	1.000	0.01
1.500	1.000	0.01

Table 16: Electrolyte used during amperometry experiments, including concentration.

3.5 SEM: Scanning Electron Microscope

SEM images were taken in one of two SEM suites:

- Jeol 8600 at TWI
- Jeol JSM 6500 F at the University of Southampton

All samples for images were prepared in accordance with local procedure.

3.6 Battery Charge and Discharge Cycling

Three battery designs were built and tested. The design of each one is informed by previous designs. They are described below.

3.6.1 Battery 1: TWI Thin Film Battery

The first battery, under the TWI industrial project, was assembled using the 95 cm² negative electrodes described in the section 3.3.2 as negative electrodes, and the positive electrode was a solid lead sheet (99.9 %, Goodfellow). The casing was manufactured by TWI, made from Poly(methyl methacrylate) (PMMA) plastic and bonded with an epoxy resin. The assembly is shown in figure 14. During operation, the casing was filled with 5 M sulphuric acid.

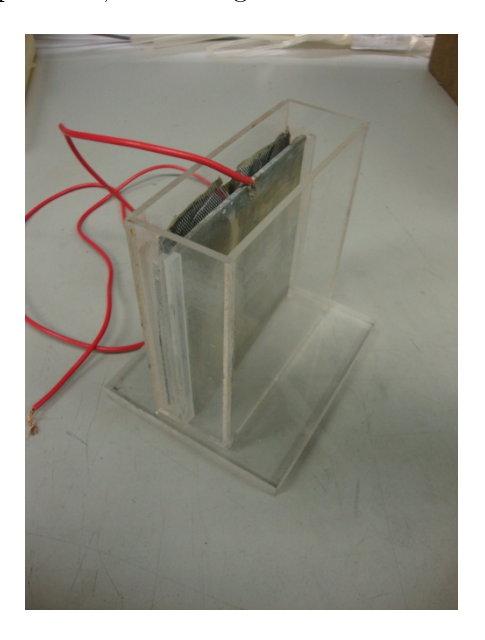


Figure 14: Battery 1 casing and electrodes.

Battery cycling was performed using a bespoke battery test rig built by MIRA. The cycle regime involved constant voltage charging at 2.445 V, and constant load discharging at 5 Ω . The cut-off current for charge was <30 mA and the cut-off voltage for discharge was 1.7 V.

Other tests were performed on this battery using the Autolab potentiostat to test the power output. Constant current inputs at 4 mA cm² for charge and 1, 3, 5, 10 and 15 mA cm² for discharge were used. An initial charge period of 600s was applied, followed immediately by discharge for 20 s. Each subsequent charge period was 60 s, and discharge 20 s. The operating voltage was recorded, and used with the current to calculate the battery power.

3.6.2 Batteries 2 and 3: Static Soluble Lead Acid Batteries

Flat-plate electrode, soluble lead batteries were assembled. Figure 15 shows the two different sizes of battery set-up. The component labels are shown in figure 16. During operation, the components were fixed together using G-clamps.

Battery 2 is a single cell, where battery three is four cells connected in series in a bipolar arrangement. Battery cycling for battery 2 was conducted using an MTI battery tester, while battery 3 was tested using a BasyTec battery tester (the maximum voltage for the four-cell battery

exceeded the limit of the MTI tester). Electrical connection was made via crocodile clips to the nickel current take-off tabs.

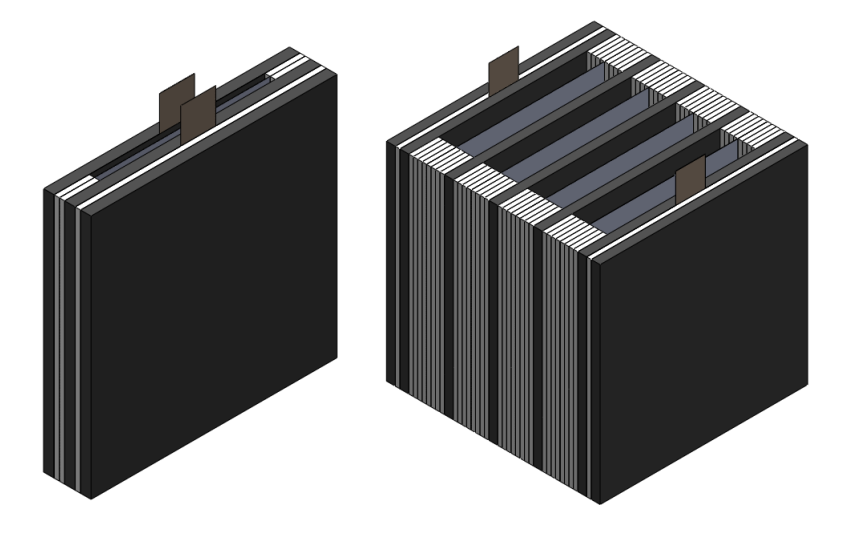


Figure 15: Battery 2 (single cell) and battery 3 (four cell) in isometric projection.

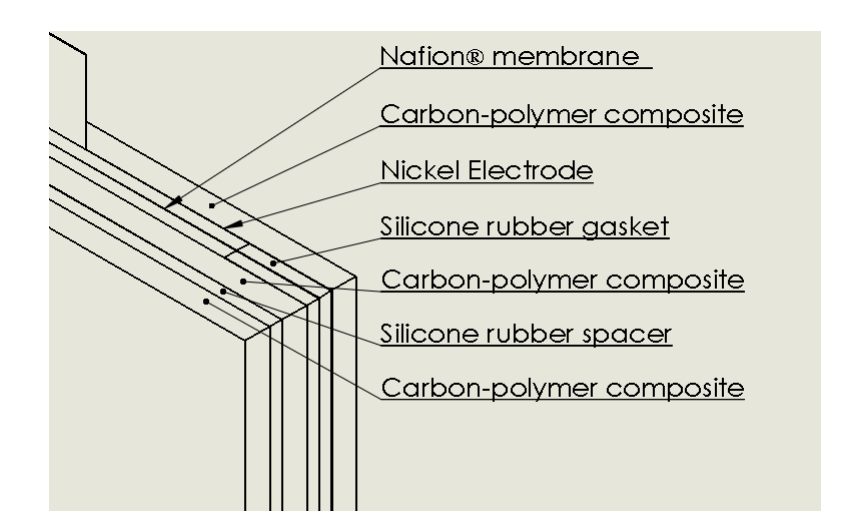


Figure 16: Components used in Battery 2 (single cell), including carbon-polymer composite electrode, nickel electrode and current collector, silicone spacer and gasket, and Nafion ® membrane.

The materials listed in table 17 were used as electrodes for both batteries 2 and 3. The nickel foil was also used as a current collector, which includes the current take-off tabs.

Material	Supplier	Description
Carbon-polymer composite	Entegris	Sheet thickness, 3.2 mm
Nickel Foil	Dexmet	Sheet thickness, 0.1 mm

Table 17: Materials used as cell electrodes, including supplier and a brief description.

The materials listed in table 18 were used for various components of both batteries 2 and 3.

Material	Supplier	Description	Function
Nafion ® membrane	DuPont	m NF115/H+	Separator membrane
Silicon rubber	RS	Sheet thickness: 1.5 mm	Spacer and gasket
Nickel Foil	Dexmet	Sheet thickness: 0.1 mm	Electrode material and current collector

Table 18: Materials used during the project for other components of both the batteries 1 and 2 (single- and four-cell), including supplier and a brief description.

3.6.3 Electrode preparation

For battery 1, electrode preparation involved electrodeposition, as described in section 3.3.2 above. Eight different titanium electrodes were produced, and one solid lead plate was also used, as shown in tables 19 and 20. The nomenclature used in table 19 refers to the manufacturer, heat treatment and the mass of electrodeposited lead: for example, Goodfellow HT 16 was supplied by Goodfellow, was heat treated and had 16 g of lead electrodeposited. NHT stands for not heat treated. The nomenclature in table 20 is the manufacturer's own product name.

Name	Mass of	Total mass	Pre-	Post-	Image
	lead / g	of electrode	${ m treatment}$	treatment	
	/ 8	1			
Fibretech	7.3	/ g 19.9	Tin sputter	_	
	1.0	10.0	coated		
			(TWI,		
			Edwards)		
			Edwards)		
Goodfellow	16.0	24.5	-	Heat-	
HT 16				treated in a	
				vacuum	
				oven for	
				220 °C for	
				20 minutes.	200 um
Goodfellow	24.0	30.7	-	Heat-	0992032-0320-1465-00
HT 24				treated in a	• 1
				vacuum	
				oven for	
				220 °C for	
				20 minutes.	20 us
Goodfellow	24.0	31.2	-	-	09820120329 11 07 76
NHT 24					
					20 un

Table 19: Lead-plated titanium electrodes used in battery 1 (single-cell). The substrate material, mass of deposited lead, total electrode mass and pre- and post-treatments are listed.

Name	Mass of	Total mass	Pre-	Post-	Image
	$\mathrm{lead}\ /\ \mathrm{g}$	of electrode	${ m treatment}$	treatment	
		/ g 2.2			
Dexmet	1.5	2.2	-	-	
3020 1.5					
Dexmet 1108 1.5	1.5	2.4	-	-	22.0-
Dexmet 3020 14	14.2	15.2	-	-	- 25 m
Dexmet 1108 14	14.2	15.2	-	-	20.0
Lead plate	-	300.0	-	-	09820120538413446

Table 20: Lead-plated titanium electrodes used in battery 1 (single-cell). The substrate material, mass of deposited lead, total electrode mass and pre- and post-treatments are listed.

The electrodes were cleaned by rinsing in acetone prior to insertion in the battery casing. For batteries 2 and 3, the electrodes were prepared by rubbing with 800 grit silicon-carbide paper, then rubbing with acetone.

4 Results: Electrochemistry of electrode materials in acid solutions

The two battery systems under investigation in this project use electrodes electroplated with lead. The quality of the lead electrodeposit is critical to battery performance, and is therefore investigated. Preliminary studies on selected materials have been conducted to ascertain stability of the electrodes during lead electrodeposition and dissolution.

4.1 5 M H_2SO_4

The electrochemical method used is cyclic voltammetry in 5 M $\rm H_2SO_4$. All potentials are stated with respect to saturated calomel electrode (SCE) and the temperature was 293 \pm 2 K.

Lead The behaviour of solid lead in 5 M H₂SO₄ was determined in order to provide a baseline for comparative studies and to ascertain the operating potential window of the Pb/PbO₂ electrode couples. A cyclic voltammogram of a solid lead electrode was taken (figure 17). The potential was scanned from a starting value of 0 V vs. SCE towards a value of -1.75 V before returning to 1.9 V at a constant scan rate of 50 mV s⁻¹. Both the positive and negative electrode reactions are shown in this voltammogram.

On the forward scan, i.e. scanning towards more negative potentials (arrow 1), there is a cathodic reduction reaction occurring at -0.88 V. This corresponds to conversion of PbSO₄ to Pb metal (area A). The PbSO₄ spontaneously forms on the surface of lead when it is exposed to H₂SO₄. At potentials more negative than -1.30 V, and during the return scan (arrow 2), the current diminishes. This is due to consumption of the PbSO₄.

On the reverse scan there is an anodic oxidation peak beginning at circa -0.95 V (arrow 2), and peaks at -0.51 V which corresponds to the formation of PbSO₄ on the electrode surface (area B). There is a sharp drop in current at -0.46 V, which corresponds to an electrically insulating layer of PbSO₄becoming formed. This layer isolates the lead from the electrolyte, and thus no more reaction takes place as the current drops to zero.

The mechanism for PbSO₄ formation at negative potentials is a two-step reaction. Pb²⁺ ions dissolve from the surface of the solid lead, before bonding with SO₄⁻ to form the solid PbSO₄. This two-step reaction is shown in equations 6 and 7.

$$Pb + HSO_4^- - 2e^- \rightarrow Pb^{2+} + SO_4^- + H^+$$
 (6)

(electrochemical dissolution step)

$$Pb^{2+} + SO_4^- \leftrightarrow PbSO_4^- \tag{7}$$

(chemical deposition step)

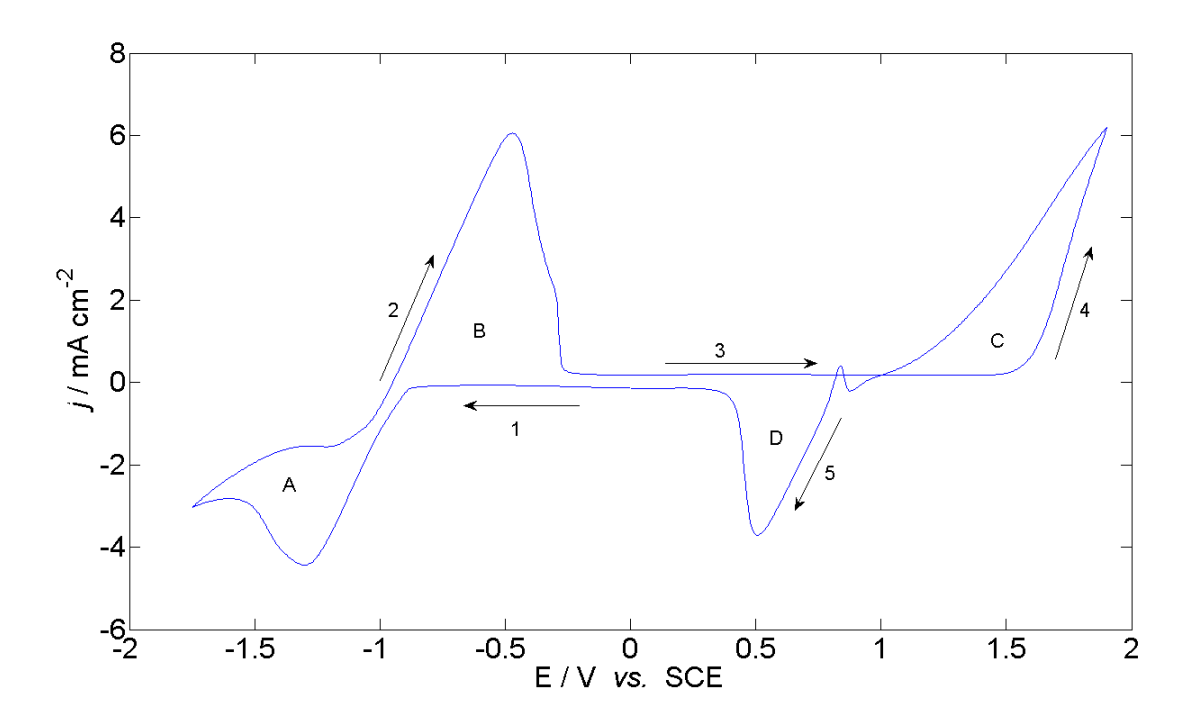


Figure 17: Cyclic voltammogram of lead in 5 M $\rm H_2SO_4$ at 50 mV s⁻¹ from -0 V vs. SCE to -1.75 V to 1.9 V vs. SCE.

At positive potentials, the reaction couple is PbSO₄ /PbO₂. On the forward scan, (arrow 3), PbO₂ formation begins at 1.57 V, continuing on the reverse scan (area C) until 1.01 V. The overpotential for PbO₂ deposition (area C) is 0.66 V, whereas for the negative electrode reaction (Pb/PbSO₄) there is no nucleation overpotential. In addition, the PbO₂ dissolution reaction kinetics are less favourable than for Pb dissolution, as shown by the magnitude of the current peaks. The peak current for PbO₂ dissolution is 4 mAcm⁻² (D) whereas Pb dissolution peaks at 6 mAcm⁻² (B).

For these reasons, in the lead-acid battery, the performance is limited by the positive electrode. During battery charge, the greater overpotential is limiting, and during discharge the slower reaction kinetics are limiting.

4.2 Electrodes in 6 mM Pb²⁺ in aqueous CH₃SO₃H (1 M)

Cyclic voltammograms of selected electrode materials were taken 6 mM Pb²⁺ in aqueous CH₃SO₃H (1 M). The materials included; nickel, copper, mild steel, 304L steel, glassy carbon and titanium. It was not practical to include lead in the set of electrode materials (thus repeating the experiment in section 4.1), as lead is soluble in CH₃SO₃H. The experimental conditions were consistent with the sulphuric acid experiments, with the exception that the electrolyte used was 6 mM Pb²⁺ in aqueous CH₃SO₃H (1 M). The temperature was 293 \pm 5 K, and the potential was scanned from a starting value of -300 mV vs. SCE down to a value of -800 mV before returning to -300 mV at a constant scan rate of 25 mV s⁻¹. This allows the investigation of the Pb²⁺/ Pb couple during deposition and stripping, which correspond respectively with charge and discharge of the soluble lead acid battery system at the negative electrode. In addition to assessing the suitability of these materials for the soluble lead acid system, the ability of these materials to be electrodeposited is assessed for the Thin Film battery system.

Nickel Figure 18a shows a typical Pb^{2+}/Pb voltammogram in 6 mM Pb^{2+} in aqueous CH_3SO_3H (1 M) on the nickel electrode. During the forward scan a cathodic reduction wave is observed starting at -0.58 V (shown as the dark blue line on figure 18a). This corresponds to the reduction of Pb^{2+} to Pb, which is the deposition of solid Pb onto the electrode surface. The current increases as the overpotential increases, showing that the rate of lead consumption at the electrode surface is within the limits of mass transport to supply lead from the electrolyte bulk,

During the reverse scan, the formation of Pb continues to a potential more positive than the reduction wave, before a sharp symmetrical anodic stripping peak, commencing at -0.48 V and peaking at -0.43 V. The commencement of this peak, which corresponds with the crossover from cathodic to anodic current, is a good approximation for the equilibrium potential of this couple, and is shown as the black dashed line on figure 18a. The overpotential for Pb deposition on nickel therefore is 20 mV. This overpotential is due to the kinetics of forming Pb nuclei on this electrode surface. (As we shall see, the value of the overpotential is different for each material.) This overpotential is low, and shows that electrodeposition of lead onto nickel is favourable.

The anodic stripping peak is symmetrical and drops to zero current; typical of a dissolution reaction where the current initially rapidly increases to a peak then drops to zero as all the material is consumed. The dissolution current density is greater than the deposition current density, because the material is on the electrode surface and thus there are no mass transport limitations.

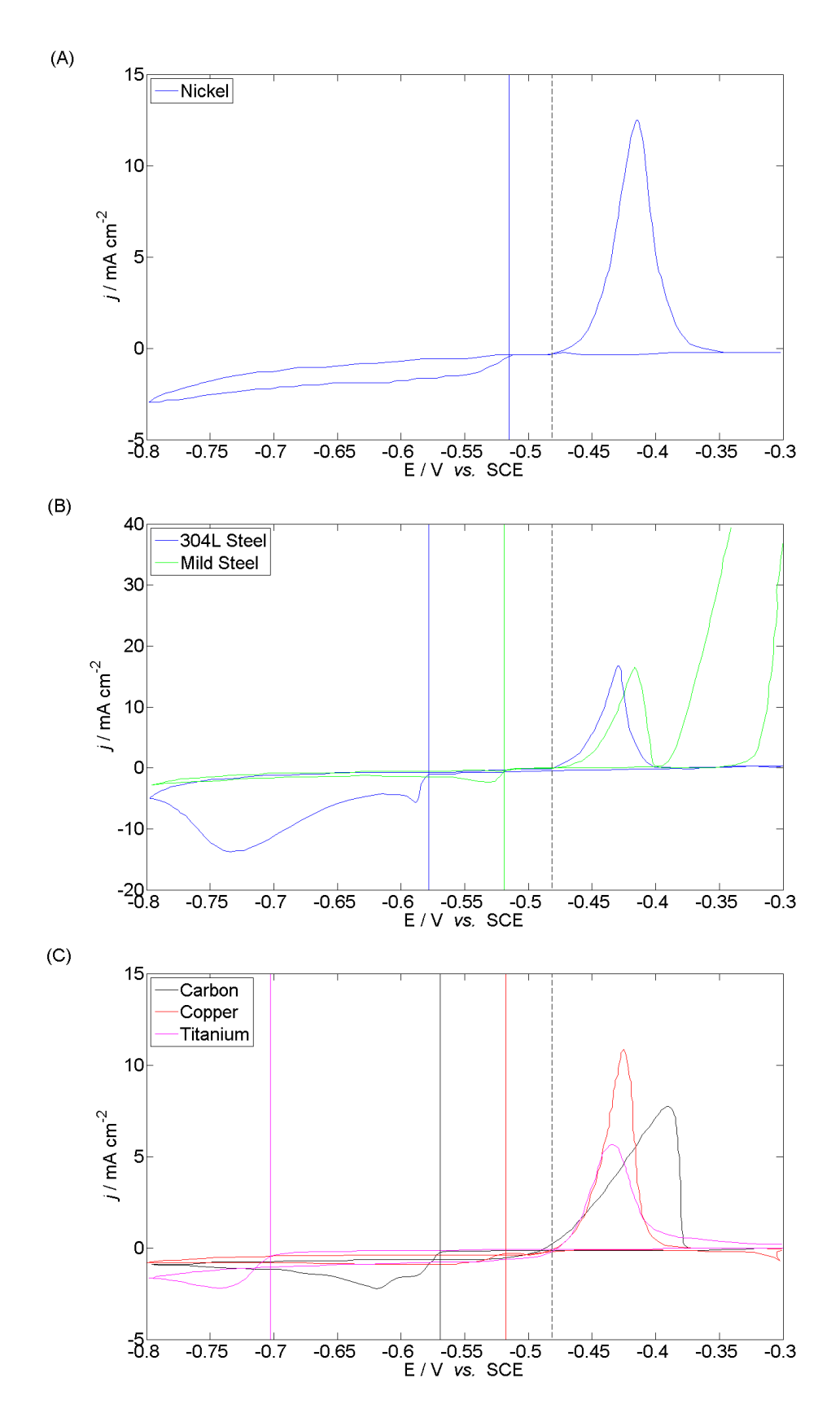


Figure 18: a, b and c. Cyclic voltammograms of various electrode materials in 6 mM Pb 1 M $\rm CH_3SO_3H$ at 25 mV s⁻¹ from -0.3 V to -0.8 V to -0.3 V vs. saturated calomel electrode. 293 K.

304L steel, mild steel $\,$ Figure 18 b shows voltammograms for each 304L steel and mild steel in the 6 mM $\,$ Pb $^{2+}$ in aqueous CH₃SO₃H (1 M). At the 304L steel electrode, during the forward scan

a cathodic reduction wave with two peaks is observed starting at -0.58 V (shown as the dark blue line on figure 18a). This first peak at -0.58 V of 6.5 mA cm⁻² again corresponds to the reduction of Pb²⁺ to Pb (which is the deposition of solid Pb onto the electrode surface). Following the initial peak, the current then decreases until -0.61 V, where it begins to increase again to another peak at -0.73 V of 13.8 mA cm⁻². The second peak is a result of either 1) a parasitic side reaction from electrochemical activity of an alloying element and/or vigorous hydrogen evolution, or 2) increasing surface area due to rough or dendritic Pb deposits.

On the reverse scan, the formation of Pb continues to a potential more positive than the reduction wave, before a sharp symmetrical anodic stripping peak, commencing at -0.48 V and peaking at -0.43 V. The overpotential for Pb deposition on 304 L steel therefore is 100 mV. This higher overpotential is due to the unfavourable kinetics of forming Pb nuclei on this electrode surface.

The mild steel electrode again exhibits a reduction wave on the forward scan, the values for which are -0.52 V and a magnitude of 3 mA cm⁻². On the reverse scan, the oxidation peak is similar to the other materials, showing that dissolution is not as sensitive to electrode material as deposition. However, as the voltage increases above -0.4 V, huge oxidation currents reveal high-rate corrosion.

Carbon, copper, titanium Figure 18c shows voltammograms for carbon, copper and titanium.

For the carbon electrode on the forward scan, no current was observed until -0.52 V, when the reduction wave begins. The gradient for the reduction wave is lower than that for the nickel. This shows that nucleation is less facile on carbon, and this is a result of crystallographic mismatch between Pb and C. The higher nucleation overpotential for carbon, of 120 mV, corroborates. In addition, there is a second wave. This is a result of the uneven, dendritic deposit formation causing an increase in electrochemically active surface area.

On the reverse scan, there is an oxidation peak, which also has a lower gradient than the other materials. This is a result of the lower conductivity of carbon: Ohm's Law dictates that the gradient of this curve should be lower as the higher resistance slows the reaction. There are no significant parasitic side reactions for the carbon electrode, as it is an inert element.

The copper electrode shows a reduction peak on the forward scan at a very low overpotential of 20 mV, showing that there is good crystallographic alignment between Pb and Cu. The oxidation stripping peak on the reverse scan is also typical.

The voltammetry of the titanium electrode shows a large nucleation overpotential of 220 mV. This is a result of the unfavourable surface properties caused by the titanium oxide layer present on the surface. On the reverse scan, the oxidation peak is relatively small. This indicates that less material was deposited due to the large overpotential leading to less time for deposition.

Nucleation overpotentials The nucleation overpotentials for the Pb²⁺/Pb redox couple on the selected materials are shown in table 21. Titanium has the highest overpotential at 220 mV. This means that it is the least suitable for lead deposition. Nickel, with the lowest overpotential at 34 mV is the most suitable.

Nickel	Copper	Mild Steel	Carbon	304 L Steel	Titanium
34	37	38	88	97	221

Table 21: Nucleation overpotential for shortlisted substrate materials in 6 mM Pb 1 M $\rm CH_3SO_3H$ at 25 mVs⁻¹. 293 K.

4.3 Summary of material suitability

In effect, a process of elimination can be used to assess suitability of each of the electrode materials. In order to be suitable for use as an electrode in both the soluble lead and the Thin Film batteries, the material must first show good characteristics for lead electrodeposition. The selection criteria for suitable substrate materials includes: minimal side reactions and a low nucleation overpotential.

The materials which suffer from side reactions are 304L and mild steels, which are affected by electrochemical activity from alloying elements and corrosion respectively. In the case of 304L steel, the side reactions disrupt deposition and will result in an incomplete, porous lead deposit. The corrosion layer on the surface of the mild steel forms upon immersion in the deposition bath, and will form a barrier to smooth, coherent lead deposition. These reactions rule out suitability for electrodeposition of lead for both of these materials.

The nucleation overpotential is related to the crystallographic match of the deposit and the substrate. A greater match leads to a smoother, more coherent deposit which is more fit for purpose. Crystallographic mismatch accounts for the high overpotentials for carbon and 304L steel. However, titanium has the greatest nucleation overpotential; this is due to the insulating oxidation layer on the surface.

As a result, nickel, copper and carbon are the most suitable electrode materials for electrodeposition because they exhibit minimal side reactions. However, they are known to dissolve or produce gassing, but the rate of these reactions is low in comparison to the other candidate materials. Of these three, nickel and copper have the lowest deposition overpotentials. It is recommended that these materials become the focus for further investigation as the substrate for lead electrodepostion within both soluble and Thin Film batteries.

5 Results: Thin Film lightweight battery

This body of work was directed by the industrial sponsors, TWI, who had a specific interest in titanium mesh electrodes. These meshes were to be electrodeposited with lead, which would then act both to 1) protect the titanium from further passivation, and 2) as active material in a sulphuric acid electrolyte. The name 'Thin Film' refers to the layer of lead which is deposited onto the titanium. The lead film should be as thin as possible in order to reduce the weight of the electrode. Similarly, titanium was favoured as a material due to its low density. Reducing the weight of these components will significantly reduce the total weight of the battery, as the electrodes and active material form the majority of the weight of lead acid batteries. [19] Thus, the specific energy and power (Ah kg⁻¹and W kg⁻¹) of the battery will be increased.

5.1 Electrodeposition on titanium meshes

A suitable electrodeposit can be defined in two ways: 1) it completely covers the substrate surface; 2) it is well adhered or 'locked-in' to the surface. The methods used to assess the success suitability of the electrodeposition are SEM and EDX analysis. EDX analysis is used to ascertain the composition of the deposit, and to investigate the exposed titanium surface. In all cases, the deposit was pure lead, and the exposed titanium oxide layer was so thin that it is not visible with EDX analysis.

The SEM images taken of the lead electrodeposits show two perspectives; 1) surface and 2) cross section. Clearly visible in the figure 19 are the lead nucleation sites (A), which appear as hemispherical nodules on the substrate surface (B).

As the deposition progresses, these nucleation points increase in size until they overlap. This can most clearly be seen in table 22; as the deposition progresses with time, the nodules increase in size and then completely cover the substrate. Complete coverage of the substrate by the Pb coating occurs after 60 minutes at 55.5 mA cm⁻², corresponding to 0.21 g of lead per cm². All surface area values given are for geometrical surface area.

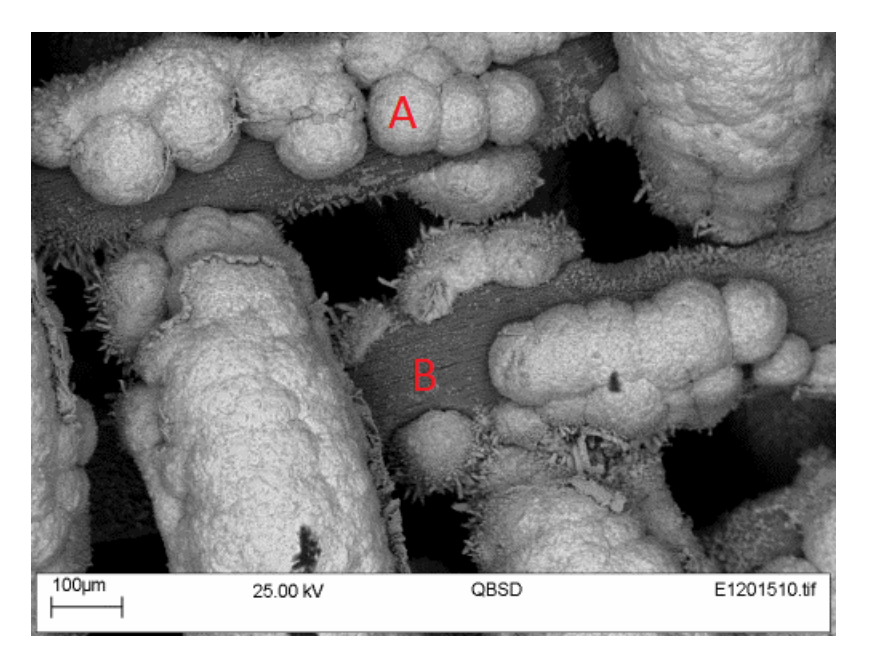


Figure 19: Lead electrodeposit on titanium mesh. 50 mA cm $^{\text{-}2} for 30$ minutes at 293 \pm 5 K in 1.5 M Pb^2+ CH_3SO_3H (1 M).

			CDAT	
Deposition	Deposition	Theoretical	SEM image	
current	time /	mass of		
density /	min	lead de-		
mA cm ⁻²		posited		
		/ g cm ⁻²		
55.5	30	0.11	Tight GGD EXCEPT #	* 200 0 500 0 500 1884 080 100084
55.5	45	0.16	The Trans	THE HAVE GID COMP
55.5	60	0.21	THE RESERVE SEED SCHOOL P	10 10 100000 10000000 100000000 10000000
55.5	120	0.43	The Krew GRO Konsore	TO BE THE STATE OF ST

Table 22: SEM images showing the morphology and distribution of lead electrodeposited onto Goodfellow woven mesh from 1.5 M Pb 1 M methanesulphonic acid with 1 g l⁻¹ligninsulphonic acid at 55.5 mA cm⁻² for time periods between 20 – 120 minutes. 293 \pm 5 K

These values are related to Faraday's Law (equation 8), which states that the mass of the electrodeposit is proportional to current and time:

$$M = \frac{Itm}{Fz} \tag{8}$$

where M = mass of electrodeposit / g, I = current / A, t = time / s, m = molecular mass / g mol⁻¹, F = 96500 and z = valence of metal.

As the current density is increased, the morphology of the deposit is affected. Higher current densities lead to more uneven deposits. This is shown in table 23, where the current desnity ranges from 14 to 221 mA cm⁻² and the deposition time is adjusted to preserve a deposit of 0.25 g of lead per cm². The cross section image taken at 14 mA cm⁻² shows that the lead deposit is smooth and completely covers the substrate. The deposits become more nodular as the current density increases, and at 111 mA cm⁻² the substrate is no longer isolated, despite having an equal mass of lead deposit.

These nodular deposits have a nigher surface area-to-mass ratio, and would (potentially) be more suitable than the smooth deposits for use as a battery electrode. However, the actual amount of lead which is deposited is less than this theoretical value. There are inefficiencies in the deposition process due to side reactions and electrical resistance in the system. The efficiency decreases as the current density increases. Unfortunately, it was not practicable to measure this by weighing the sample before and after deposition. The deposited lead and the substrate material were both fragile and shed material at the lightest movement.

Deposition	Deposition	SEM	image
current density / mA cm ⁻²	time / min		
14	240		0 500 ° 205 0 €
14	240		
28	120		200m 2004V ORIO E131463.9
111	30	190/m 25 00 W 0000 E10000H M	2000 000 000 E100048
		25.0VW	2000 € 60 € 60 € 60 € 60 € 60 € 60 € 60
221	15	P	

Table 23: SEM images of lead electrodeposited from 1.5 M Pb 1 M methanesulphonic acid at 293 ± 5 K at current densities between 14 and 221 mA cm⁻². 0.21 g cm⁻² of lead was deposited during each set.

While the current density affects the morphology of the deposit (and thus the surface area), there is no effect on the interface between the deposite and the substrate. Deposition at current densities between 55.5 and 221 mA cm⁻² were investigated. Cross sectional SEM images of the lead-substrate interface (table 24) show that consistently there is a gap of up to 2 µm between the lead (areas 1) and the substrate (areas 2). There may be several factors causing this gap: 1) the dissimilarities between the crystal structure of lead (face centred cubic) and titanium (hexagonal close packed) causing residual stress may cause lamination; or 2) the titanium oxide layer may be preventing adhesion of the two metals. Also, 3) the gap may be a shadow due to a slight angle on the SEM stage; there is a possibility that more of the soft lead was removed during polishing than the hard titanium. This interface gap was not reduced when three different cleaning methods were tested (rubbing with acetone, ultrasonic bath and plasma field). The effect of this interface gap is poor adhesion: the samples were readily fragmented on the slightest impact or flex and had to be treated with utmost care. It would have been useful to conduct adhesion tests, but the time constraints of the project prohibited this.

In addition to the poor adhesion, many of the deposits exhibit porosity, as highlighted in the red circles in the table. Areas a are a result of incomplete amalgamation of the nucleation points, and area b appears to be a stress crack, likely also caused by the dissmilar crystal structures of the deposit and substrate.

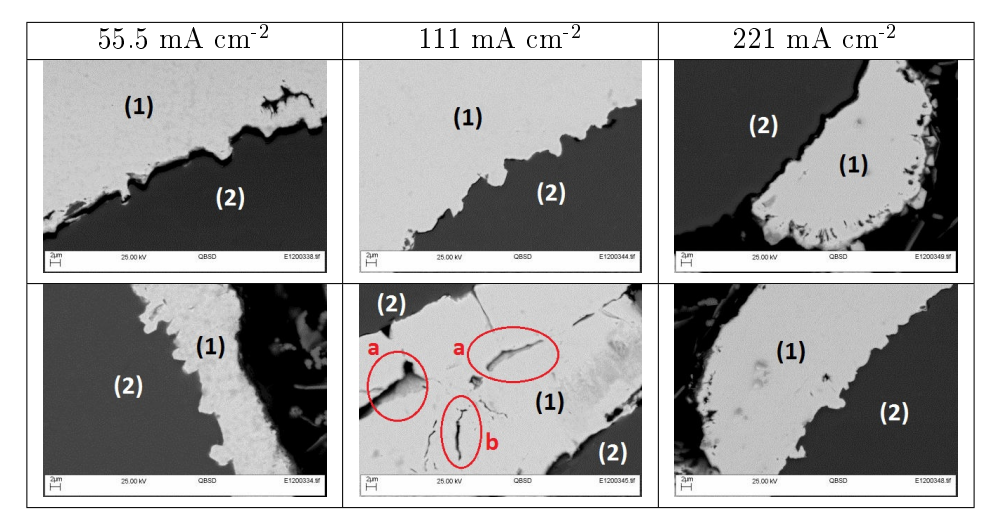


Table 24: The lead - titanium interface after electrodeposition from 1.5 M Pb 1 M methanesulphonic acid at current densities between 55.5 mA cm⁻² and 221 mA cm⁻² for 60 minutes. 293 \pm 5 K

5.1.1 Electrodeposition summary

For the thin film battery, it is important to achieve different types of lead coating in order to investigate the effects on battery performance. A high surface area deposit may increase battery power and capacity as the amount of lead in contact with the electrolyte is increased. However, the exposed titanium may interfere with the battery performance so a completely isolated substrate is also important to achieve. In this experiment set, both types of deposit have been achieved.

The optimum lead coating is the minimum mass of material which forms a complete covering. Any excess material will not participate in the reaction and act to increase the electrode mass.

The lead surface area is affected by both the amount of material deposited and by the current density. At low amounts of lead, the surface area is large as a result of the nodular nucleation points. High current densities also yield a high surface area: SEM imagery shows that the nodules become more pronounced as the current density is increased.

The titanium mesh can be completely coated at current densities up to 55.5 mA cm⁻². At greater current densities nodular deposits form preferentially to a complete deposit. The minimum amount of time required to completely coat the substrate at this current density is 60 minutes. It is important to use a minimal amount of lead as this will minimise the electrode mass.

The optimum coating on Goodfellow titanium mesh was achieved at 55.5 mA cm⁻² for 60 minutes resulting in 0.21 g cm⁻². The electrolyte was 1.5 M Pb²⁺ in aqueous CH₃SO₃H (1 M) and the temperature was 293 \pm 5 K. This was the minimum mass of material required to form a complete deposit.

Although the best coating was complete it did not adhere well to the titanium surface due to crystallograpahic mismatch or an oxide layer on the substrate.

5.2 Battery testing

This Thin Film battery operates via the surface reaction of the Pb and PbO₂ with the H₂SO₄, therefore the surface area will directly affect the power and capacity of the battery. The effects of using different geometry substrates and different surface-area to volume ratios was investigated.

The thin film battery comprises a PMMA case, a solid lead positive electrode and a lead-coated titanium mesh negative electrode, immersed in 5 M H₂SO₄ electrolyte. Nine different thin film batteries were constructed, each one with a different negative electrode. Table 25 shows these batteries and the mass of the negative electrodes; also included is the Cyclon D cell battery, which was used a benchmark for comparison to a commercially available battery. All electrodes (except the solid lead electrode) were lead coated titanium meshes, where the mesh is referred to as the 'grid' and the lead is the 'active material'. A description of the manufacturing process can be found in the experimental section. The effect of different negative electrode features including: 1) substrate mesh geometry, 2) amount and 3) morphology of deposited lead, and 4) heat treatment was investigated by comparing the specific capacity (Ah kg⁻¹) and specific power (W kg⁻¹) of the batteries. Two batteries were used as benchmarks: 1) a solid plate electrode battery, of identical construction to the Thin Film batteries and 2) a commercially available Cyclon D cell battery. The Cyclon D cell has a capacity of 2.5 Ah and a specific electrode capacity of 37.6 Ah kg⁻¹.

Nogative electrode	Negat	ive electrode mass / g	
Negative electrode	Grid only	Grid and Active Material	% of grid mass from active material
Dexmet 3020 1.5	0.7	2.2	68.2
Dexmet 1108 1.5	0.9	2.4	62.5
Dexmet 3020 14	1.2	15.2	92.1
Dexmet 1108 14	1.2	15.2	92.1
Fibretech	12.4	19.9	37.7
Goodfellow HT 16	8.5	24.5	65.3
Cyclon D Cell (commercial)	24.9	66.9	62.8
Goodfellow HT 24	6.7	30.7	78.2
Goodfellow NHT 24	7.2	31.2	76.9
Solid Plate	316.9	316.9	100

Table 25: Table showing mass of electrodes used in the thin film battery, including with and without active material. Also included is the Cyclon D cell, where the mass of the electrode is the mass of the grid without active material.

Grid geometry Figures 20 a and b show the capacity, power and the specific capacity and power for each of the thin film batteries. The capacity ranges from 0.002 Ah to 0.009 Ah. There does not appear to be a correlation between the grid geometry and the capacity, as similar grids have a large capacity range: for example, the Dexmet grids, which range from 0.002 Ah to 0.008 Ah. It is known that the Pb/PbSO₄ reaction only occurs at the active material surface / electrolyte interface. This large range shows that the surface area of the active material is not dependent on the surface area of the substrate, but on the electrodeposition conditions, and the resulting surface morphology of lead. The greatest factor affecting lead surface area during electrodeposition is the amount of lead.

As for the specific capacity and power, the two lightest electrodes, the Dexmet 1.5 samples have the highest values. As the largest proportion of the mass is lead, this shows that again, the

amount of lead has more effect than the electrode geometry.

The main effect of grid geometry was during electrode manufacture: the Fibretech grid suffered from large dendrite formations during electrodeposition. This resulted in an uneven lead distribution, and limited the total mass of lead which it was possible to deposit.

Mass of active material (electrodeposited lead) There are two main outcomes as a result of differences in the mass of electrodeposited lead: 1) active material (lead) surface area to mass ratio (dependent on the deposition current desnity) and corresponding isolation or exposure of the titanium substrate and 2) total grid mass (including the mass of the lead and the titanium).

The Goodfellow HT and NHT 24 electrodes and the Dexmet 14 electrodes were all completely coated in lead, with no exposed titanium. Three of these four electrodes had the greatest capacity; over 0.007 Ah. The capacity is not significantly affected by the exposed titanium; the Goodfellow 16 electrode also performs well.

The mass of the electrodes is largely a result of the mass of the lead. In both the specific capacity and specific power calculations, the most significant difference is the mass of the electrodes, which ranges an order of magnitude, whereas the capacity and power values are similar. Another implication of the small capacity and power range is that not all the lead is utilised. (Only the surface lead is consumed in the Pb/PbSO₄ reaction.) This is most clearly shown by comparing electrodes Goodfellow NHT 24 and Dexmet 3020 1.5. If all the lead were used, then the Goodfellow electrode, with 16 times more lead, would have a capacity 16 times greater than the Dexmet 1.5. In this case, the Dexmet 1.5 has the greater capacity and power, as a result of the textured lead, with a greater surface area.

Heat treatment Heat treatment was used on the advice of the ITRI (International Tin Research Institute). Heat treatment to below the melting temperature of lead recrystallises the grains and reduces internal stresses. Unfortunately, it also reduces the surface area.

The heat treated electrodes, Goodfellow HT 16 and 24 performed well in both capacity and power tests. The HT 24 electrode capacity was greater than twice that of the NHT 24 electrode. However, for the power tests, the NHT electrode performed slightly better. The effect of heat treatment was to significantly reduce the capacity, rather than to increase the power.

Comparison to commercially available benchmark The thin film battery electrodes have a surface area of 95 cm², which is equal to the sprial-wound electrodes in the Cyclon D cell has an electrode surface area. The Cyclon has a capacity of 2.5 Ah and a specific electrode capacity of 37.6 Ah kg⁻¹. These values are two orders of magnitude higher than any of the thin film battery results.

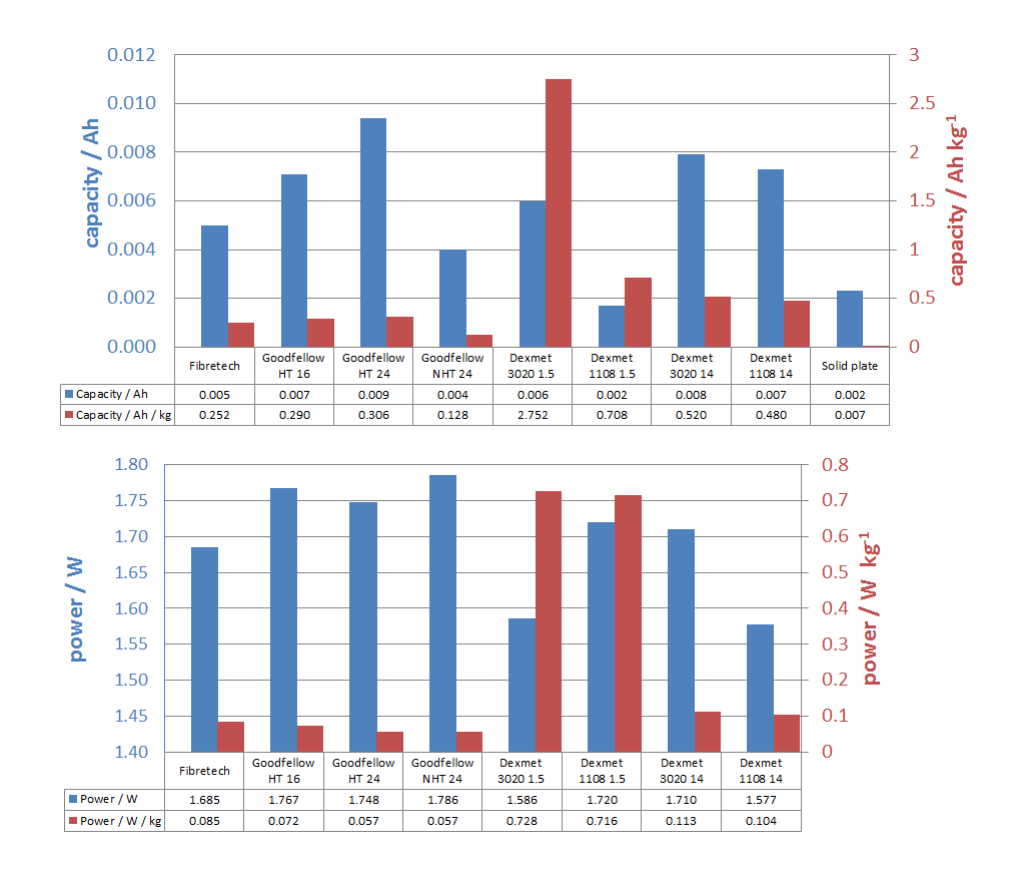


Figure 20: a Thin Film battery capacity and specific capacity, measured during a constant voltage charge, constant load discharge regime at 293 \pm 5 K. b Thin Film battery power and specific power, measured during a constant current charge and discharge regime at 293 \pm 5 K.

5.3 Thin Film battery summary

The most significant factor affecting the Thin Film battery performance (Ah kg⁻¹ and W kg⁻¹) was the amount of lead active material which was deposited onto the surface. The batteries with the least lead, had lower mass and higher specific capacity and power. An additional effect of the low mass of lead is the morhpology of the deposits. At this low mass, the deposit does not completely cover the surface, so there are nodules of lead active material which serve to increase the surface area.

It is clear that the thin film batteries do not compare favourably to the commercially available Cyclon battery, as the specific capacities are two orders of magnitude smaller.

The limitation of this thin film electrode is the solid active material, because the $Pb/PbSO_4$ reaction occurs only on the surface. There are two methods to improve this: 1) increase the surface area (as achieved in the commercial battery, where paste is used. The paste comprises a lead powder.) or 2) use a different lead chemistry, where the reaction can utilise more than the surface layer of active material.

In the case of using a paste, most of these thin film electrodes would offer a weight reduction over the Cyclon grid. It is only the Goodfellow 24 electrodes which are heavier than the Cyclon grids. Also, assuming that paste adhesion would not be problematic, these experiments show that using exposed titanium negative electrodes is a possibility.

Another factor affecting the low performance of the Thin Film batteries may well be the gap between the active material and the substrate, which would cause electrical resistance.

Hence, it is of utmost importance to use a low density, high surface area substrate which the active material can adhere to well.

6 Results: Soluble static lead-acid battery. Proof of concept

This chapter shows an investigation into using both novel electrode materials and electrolyte. This is a completely new battery chemistry. The batteries in this chapter use 1.5 M Pb²⁺ in aqueous CH₃SO₃H (1 M) as an electrolyte. The Pb²⁺ is highly soluble (up to 1.5 M) in CH₃SO₃. During charge, the Pb²⁺ is converted to solid Pb at the negative electrode and PbO₂at the positive electrode. Hence the same electrolyte and active material is used at both electrodes.

The cell configuration was preserved throughout the experiments: the negative electrodes were nickel foil, and the positive electrodes were carbon-polymer composite. The inter-electrode gap was 3 mm and electrical connection was made via crocodile clips to the current-take off tabs. The cycle regime was a shallow constant current charge and discharge profile, where each charge period corresponded to 8% of the battery capacity (calculated from [Pb²⁺] and volume of electrolyte, assuming 100% utilisation of Pb. (This assumption is discussed in chapter 8.) The effect of including Bi³⁺ (10 mM) and ligninsuphonic acid (1 g l⁻¹) as electrolyte additives and a Nafion® membrane as a separator are investigated.

Cell nomenclature	Cananatan	Additives				
Cen nomenciacure	Separator	Negative electrolyte	Positive electrolyte			
-/-/-	None	None	None			
Na/-/-	$Nafion^{ m @} NF115/H^+$	None	None			
-/Bi/Bi	None	10 mM Bi ³⁺	10 mM Bi ³⁺			
Na/Bi/Bi	$Nafion^{\mathbb{R}} NF115/H^+$	10 mM Bi ³⁺	10 mM Bi ³⁺			
Na/-/Bi	$Nafion^{\mathbb{R}} NF115/H^+$	None	10 mM Bi ³⁺			
-/Li/Li	None	Ligninsuphonic acid 1 g l ⁻¹	Ligninsuphonic acid 1 g l ⁻¹			
Na/Li/Li	$Nafion^{ m @}~NF115/H^+$	Ligninsuphonic acid 1 g l ⁻¹	Ligninsuphonic acid 1 g l ⁻¹			
Na/Li/Bi	$Nafion^{ m @} NF115/H^+$	Ligninsuphonic acid 1 g l ⁻¹	10 mM Bi ³⁺			

Table 26: Soluble lead-acid cell configurations, showing nomenclature, separator membrane and additives.

6.1 Undivided cells: -/-/-, -/Bi/Bi and -/Li/Li

The basic cell set-up uses 1.5 M Pb²⁺ in aqueous CH₃SO₃H (1 M) as an electrolyte and active material (-/-/-). Figure 22 a shows the battery voltage during charge / discharge cycles at 150 mA. The first 600 seconds of each cycle correspond to the charge period, which occurs at voltages between circa 1850 and 1950 mV. The charge part of the cycle involves electrodeposition of solid Pb onto the negative electrode surface and solid PbO₂ onto the positive electrode surface. The charge time is fixed at 600 s by the test programme, but the voltage is a result of the reaction potential and any overpotentials are a result of nucleation or electrical resistance. During the first charge, the voltage is steady at 1950 mV after an inital peak at 2100 mV. As the cycles progress, the charge voltage decreases to a constant 1850 mV, before beginning to fluctuate \pm 50 mV (figure 21) from cycle 5. This fluctuation occurs consistently throughout the cycles until cycle number 31, which can be seen in figure 22 as a colour change to yellow as the charge voltage drops to circa 1500 mV, and the battery completely fails.

The discharge voltage is smooth at 1600 mV for each cycle, with a gentle slope down to the voltage cut-off at 1200 mV. As the cycles progress, the discharge time period fluctuates. For cycle 1 the discharge time is circa 400 seconds, but this quickly drops; by cycle 10 it is 200 seconds.

A similar result is shown for the battery which uses 10 mM Bi³⁺ (-/Bi/Bi); a stable charge period at circa 1850 V, which begins to fluctuate after 27 cycles, with a varying discharge time. The first discharge time is 500 seconds but this drops to circa 200 seconds by the tenth cycle. Evidently, the Bi³⁺ is adversely affecting the performance of the battery. It is deposited before the Pb as a result of its more positive equilibrium potential; causing an efficiency drop in Pb cycling. [72] The cycle life of battery configuration -/Bi/Bi is shortened by five cycles, and the voltage efficiency is reduced (0.78 rather than 0.85 for battery configuration -/-/-, as shown in table 27). It appears from the fluctuating charge voltage and sudden drop in discharge time that these two batteries, without separator membranes, are failing by the same mode, which is discussed in detail below.

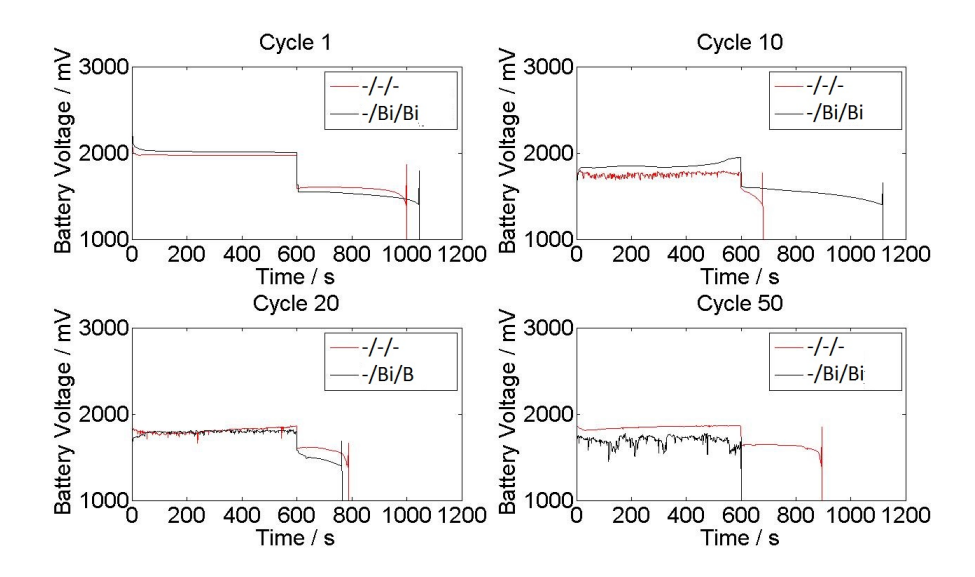


Figure 21: Four voltage / mV against time / s plots showing the cell voltage during selected charge and discharge cycles of soluble lead acid batteries at 150 mA (6 mA cm⁻²). Battery -/-/uses 1.5 M Pb²⁺ in aqueous CH₃SO₃H (1 M) electrolyte, battery -/Bi/Bi has 1.5 M Pb²⁺ and 10 mM Bi³⁺ in aqueous CH₃SO₃H (1 M) electrolyte.

Undivided cells: Failure mode The fluctuating charge voltages and sudden decrease in discharge times exhibited by both batteries -/-/- and -/Bi/Bi in figures 22 and 21 are characteristic of short circuiting, and are caused by the solid active material either forming dendrites during charge or sludging as cycling progresses. The dendrites are a result of uneven deposition, and is more typical of the Pb deposit on the negative electrode, whereas the electrochemically inactive 'sludge' is likely PbO₂ caused by the irreversibility of the positive electrode reaction. [72] Figure 23 shows the negative and positive electrodes after cycling, where it is clear that the negative active material has sloughed off and collected at the bottom of the electrode, while the positive active material is spongy and porous across the electrode surface. The negative active material which has dropped to the bottom of the electrode inidcates that the deposit was 'mossy' and porous and poorly adhered to itself, thus likely to have been dendritic. The image also shows that the thickness of this excess deposit is similar to the interelectrode gap (1.5 mm), therefore this is cause of the electrical shorting.

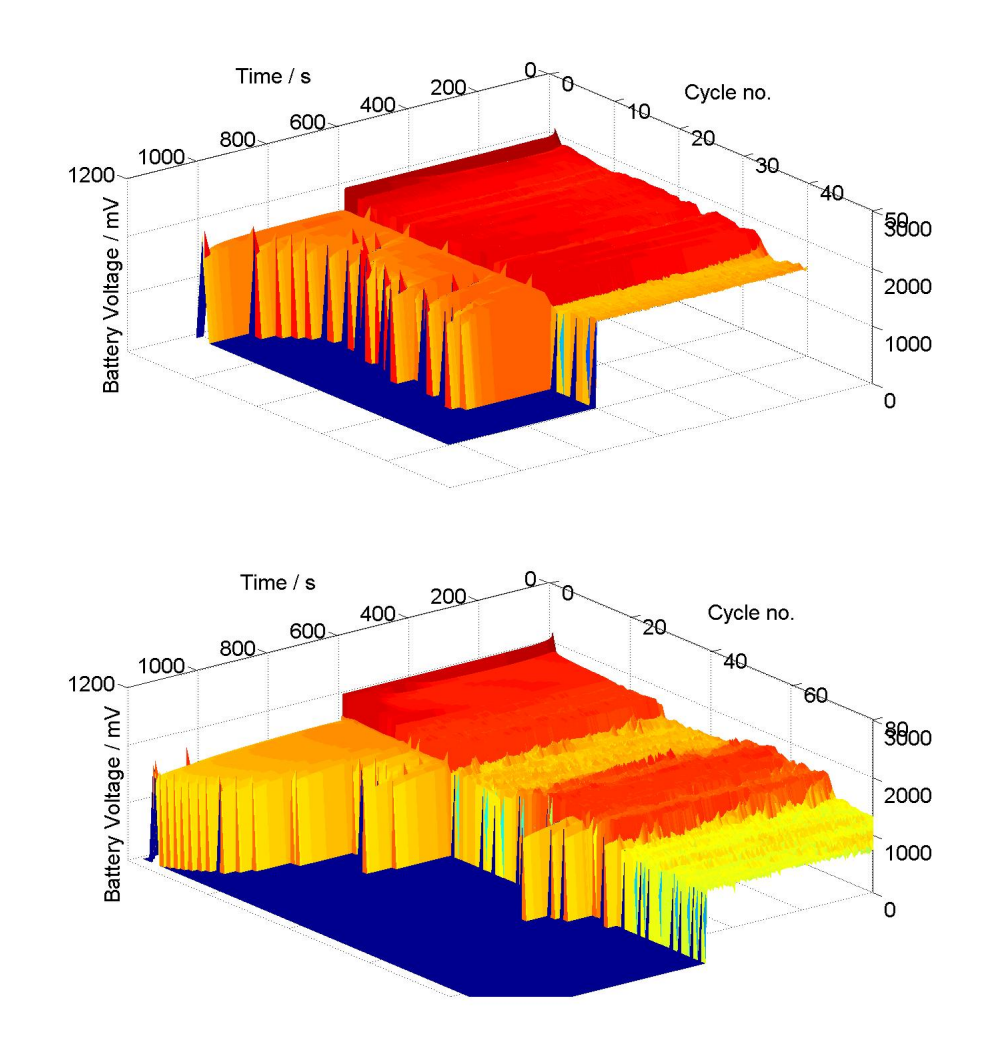


Figure 22: a and b: 3D plots showing cell voltage during charge and discharge cycles of 2D soluble lead acid batteries. a, 1.5 M Pb²⁺ in aqueous CH₃SO₃H (1 M) electrolyte (-/-/-). b, 1.5 M Pb²⁺ and 10 mM Bi³⁺ in aqueous CH₃SO₃H (1 M) (C). Constant current cycle regime at 150 mA (6 mA cm⁻²) for 600 s. Charge voltage cut-off 3 V, discharge voltage cut-off 1.2 V. 293 K.

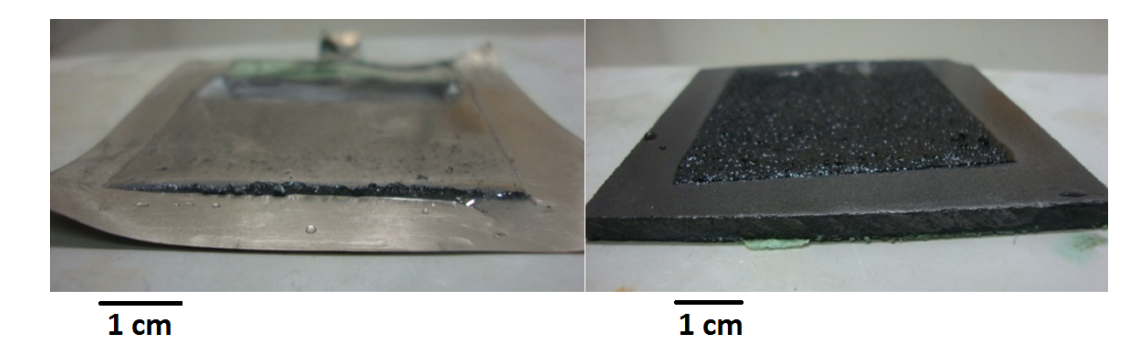


Figure 23: Battery -/-/- electrodes after cycling showing active material remaining on the surface after cycling: left; Pb negative electrode, right; PbO₂ positive electrode. Constant current charge and discharge at 150 mA (6 mA cm⁻²) for 600 s. Charge voltage cut-off 3 V, discharge voltage cut-off 1.2 V. 293 K.

While electrical shorting is the failure mode for cells -/-/- and -/Bi/Bi, cell -/Li/Li does not show the same sharp fluctuating charge voltage profile. Figure 24 shows the smooth voltage

profiles at selected cycle numbers. In this case, the ligninsulphonic acid is acting to improve the Pb deposit and reduce the dendritic formations. [25]

At cycle number 1, the charge voltage is a constant 2020 mV, and 1620 mV duing discharge. The charge voltage is lower during cycle 10, at 1900 mV. However by the end of the charge period it has increased to 2000 mV. This is evidence of oxygen gas evolution. The charge voltage for this cell is consistently higher than for the other undivided cells (battery A charge voltage is 1970 mV at cycle 1 and 1850 mV at cycle 50). The ligninsulphonic acid is adversely affecting the cell charge voltage when it is in contact with the positive electrode.

Importantly, this undivided cell has the longest cycle life of any of the undivided cells, at 43 cycles (when cell failure is defined as a drop in voltage efficiency below 75 %, shown in figure 28).

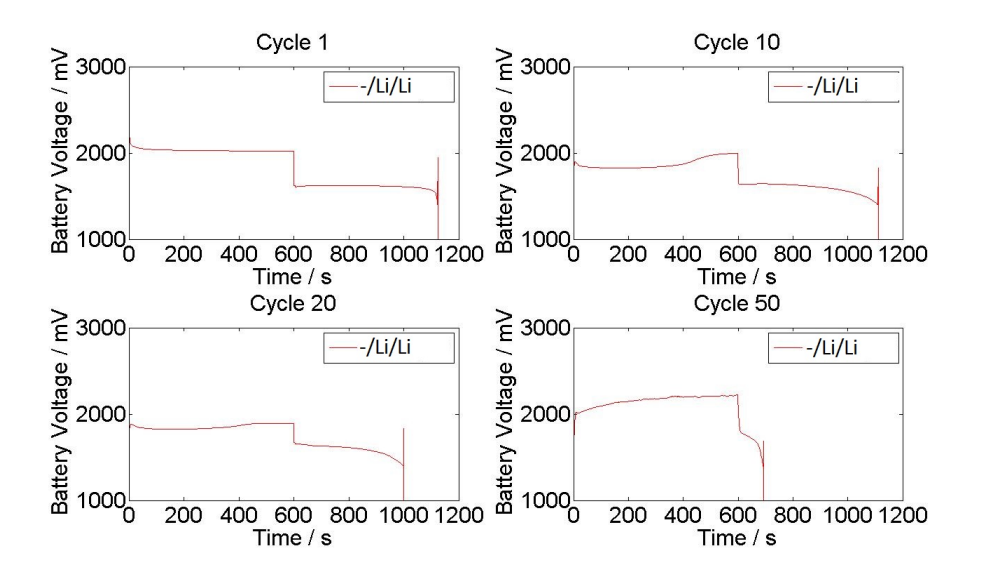


Figure 24: Four voltage / mV against time / s plots showing the cell voltage during selected charge and discharge cycles of soluble lead acid batteries at 150 mA (6 mA cm⁻²). Battery -/Li/Li uses 1.5 M Pb²⁺ in aqueous CH₃SO₃H (1 M) with 1 g l⁻¹ ligninsulphonic acid electrolyte.

6.2 Divided cells: Na/-/-, Na/Bi/Bi and Na/-/Bi

Three cell configurations were used to invstigate the effects of using a separator membrane and the Bi³⁺ additive on battery performance. The separator enables electrode specific additives to be used, as it provides a barrier between the two electrode chambers. CellsNa/-/- and Na/Bi/Bi have the same electrolyte in both electrode chambers, 1.5 M Pb²⁺ in aqueous CH₃SO₃H (1 M) without and with 10 mM Bi³⁺ respectively; whereas battery Na/-/Bi has the 10 mM Bi³⁺ additive in the positive electrode chamber only. The Nafion[®] NF115/H+ membrane used to separate the two electrode chambers allows transport of neutral molecules and cations.

The membrane has significantly changed the charge and discharge profiles of the batteries (figure 25). The charge voltage no longer suffers from sharp fluctuations, but is smooth throughout the entire charge profile with progressing cycles. In addition, the voltages have not been adversely affected by the membrane, which would be expected if the electrical resistance of the membrane was high. Table 27 shows the cell voltages and voltage efficiency for each of the cells at selected cycle numbers and figure 26 shows that the voltage efficiency of these batteries is similar until failure. The discharge voltage is 1650 mV for both cells -/-/- and Na/-/-, also suggesting that the electrical resistance of the membrane is negligible.

After several cycles, there is a sudden increase in the charge voltage, beginning at cycle number 38 for Na/-/-, 35 for Na/Bi/Bi and 55 for Na/-/Bi. This can be seen as the red regions on the plots in figure 25. Associated with this charge voltage increase is a decrease in discharge time. This increase in charge voltage indicates that the Pb/Pb²⁺ reaction has given way to oxygen evolution. This explains the decrease in discharge time: the charge current is not depositing solid lead for dissolution during discharge, so there is less available active material for consumption during discharge.

As well as preventing short circuiting, the other major effect of the membrane is to prevent bismuth poisoning of the negative electrode. When Bi³⁺ is present in the negative electrode chamber, as in the case of batteries -/-Bi/Bi and Na/Bi/Bi, the cycle life is shortened in comparison to those without Bi³⁺, batteries -/-/- and Na/-/- respectively. Battery Na/-/Bi, which has Bi³⁺ only in the positive electrode chamber, has the longest cycle life, of 61 cycles in comparison to Na/Bi/Bi, which completes 42 cycles before failure. This shows that the Bi³⁺ adversely affects the negative electrode cycle life and enhances the positive electrode cycle life.

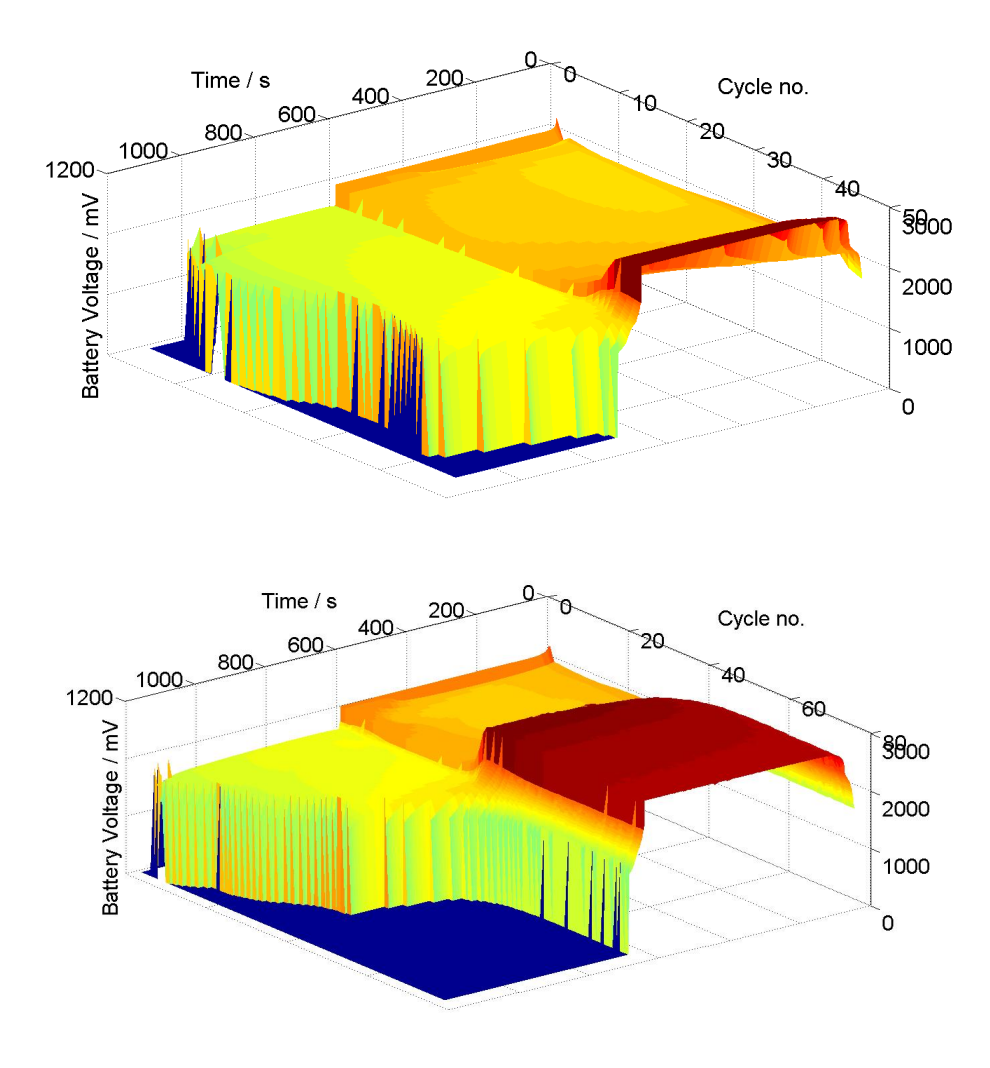


Figure 25: a and b: 3D plots showing the cell voltage during charge and discharge cycles of 2D soluble lead acid batteries. Constant current charge and discharge at 150 mA (6 mA cm⁻²) for 600 s. Charge voltage cut-off 3 V, discharge voltage cut-off 1.2 V. 293 K. a, 1.5 M Pb²⁺ in aqueous CH₃SO₃H (1 M) electrolyte (B). b, 1.5 M Pb²⁺ in aqueous CH₃SO₃H (1 M) with a Nafion[®] separator membrane (Na/Bi/Bi).

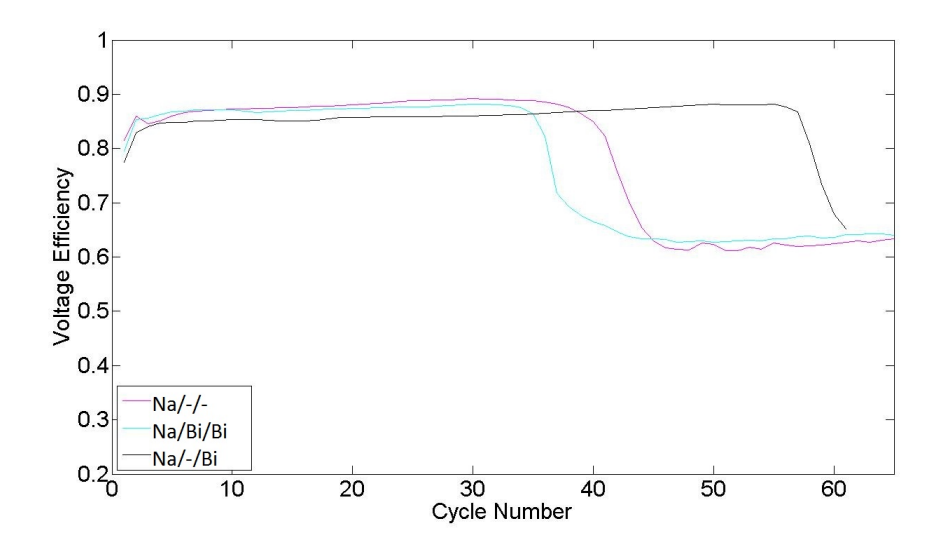


Figure 26: Voltage efficiency for batteries Na/-/-, Na/Bi/Bi and Na/-/Bi. Soluble lead-acid cells with 1.5 M Pb²⁺ in aqueous CH₃SO₃H (1 M) electrolyte, Nafion[®] membrane and 0.01 M Bi³⁺ (D and E). Cycle regime: constant current, 150 mA for 600 s. Charge voltage cut-off 3 V, discharge voltage cut-off 1.2 V. 293 K.

6.3 Ligninsulphonic acid cells: Na/Li/Li and Na/Li/Bi

The cell voltages for the three cells with ligninsulphonic acid 1 g l⁻¹ are shown in figure 27 at cycle numbers 1, 10, 20 and 50. The cell voltages at cycle 1 during discharge are consistently 1620 mV for both cells; and during charge the voltage for cell Na/Li/Li is 2010 mV. Cell Na/Li/Bi has a lower charge voltage (1970 mV) which can only be attributed to the 0.01 M Bi³⁺ at the positive electrode. By cycle 10, the charge voltage for both cells is lower for the first 300 s of charge (around 1900 mV), until it increases to around 2000 mV by 600 s. By cycle 50, the voltage profiles have differentiated. Cells Na/Li/Li and Na/Li/Bi, are exhibiting very high charge voltages of 2750 mV. This is a similar behaviour to the other divided cells: consumption of available active material results in increased voltage due to oxygen evolution.

However, the discharge times are adversely affected by the ligninsulphonic acid: cell Na/Li/Li discharges for 429 s at cycle 20, while cell Na/-/Bi discharges for 526 s at the same cycle number. In addition, there are fewer cycles to failure for cell Na/Li/Li than for cell Na/-/Bi: figure 28 shows that the voltage efficiency for cell Na/-/- drops at cycle number 47, while cell Na/-/Bi cycles to 61 cycles. Therefore, the ligninsulphonic acid is having a detrimental effect on the cell performance. Considering that it has a beneficial effect on the undivided cells, it is likely to be adversely affecting the Nafion® membrane. This is visible during cell break-down after cycling. On disassembly, the Nafion® is covered in lignin deposits, which would block free ion transport.

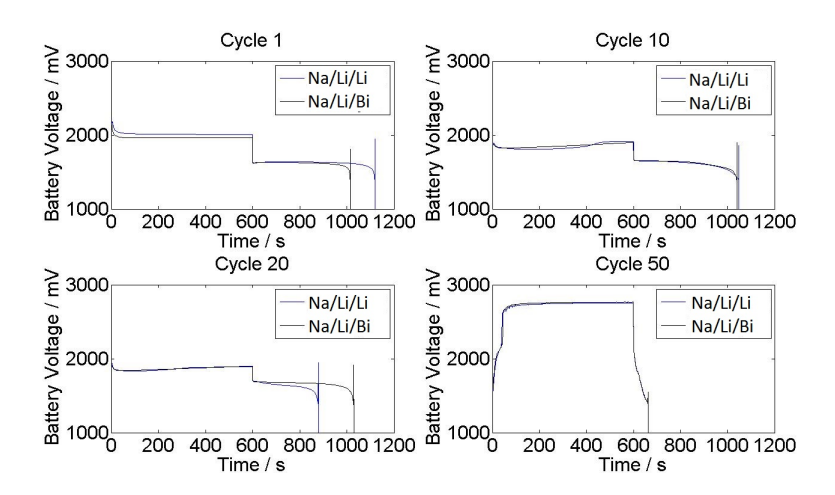


Figure 27: Four plots showing the cell voltage during selected charge and discharge cycles of soluble lead acid batteries Na/Li/Li and Na/Li/Bi. Cycle regime: constant current, 150 mA (6 mA cm⁻²) for 600 s. Charge voltage cut-off 3 V, discharge voltage cut-off 1.2 V. 293 K. Soluble lead-acid cells with 1.5 M Pb²⁺ in aqueous CH₃SO₃H (1 M) electrolyte with ligninsuphonic acid (1 g l⁻¹) and Nafion[®] membrane (G) and Bi³⁺(0.01 M) (H).

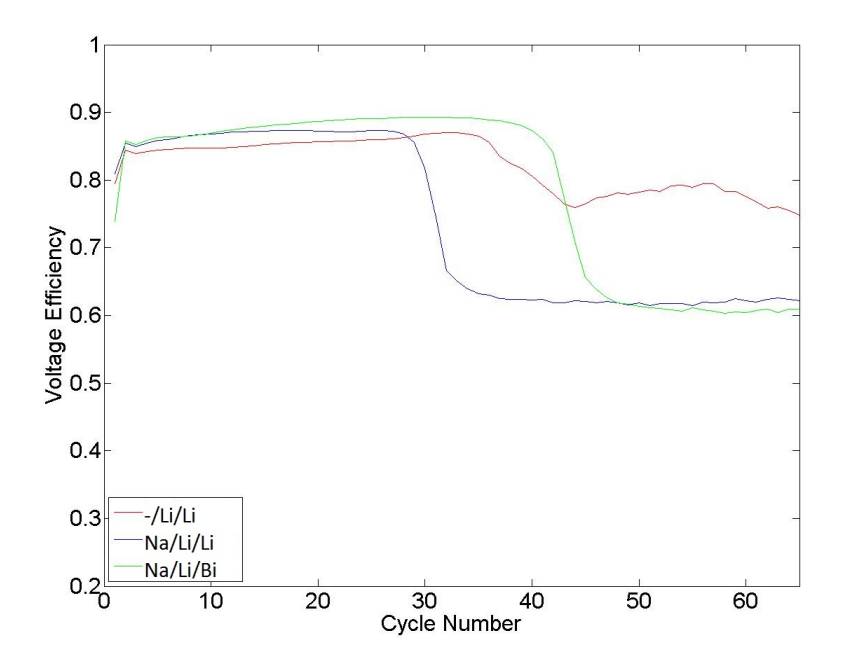


Figure 28: Voltage efficiency for soluble lead acid cells -/Li/Li, Na/Li/Li and Na/Li/Bi. Soluble lead-acid cells with 1.5 M Pb²⁺ in aqueous CH₃SO₃H (1 M) electrolyte with ligninsuphonic acid 1 g l⁻¹, Nafion[®] membrane (-/Li/Li and Na/Li/Li) and 0.01 M Bi³⁺ (Na/Li/B). Cycle regime: constant current, 150 mA (6 mA cm⁻²) for 600 s. Charge voltage cut-off 3 V, discharge voltage cut-off 1.2 V. 293 K.

Divided cells: Failure mode Both the divided and the undivided cells' electrodes become coated in solid active material as cycling progresses. The undivided cells failed due to sludging of the active material, or dendrites causing short circuits. The membrane used in the divided cells prevented short circuiting as there is no evidence of this in the battery profiles. However, there is another effect of the accumulating solid materials as the battery cycles progress: the

concentration of Pb²⁺ in solution in the electrolyte decreases. Figure 29 shows the concentration of Pb²⁺ in solution at the end of each charge/discharge cycle. The concentration is calculated based on the average values, assuming that the energy efficiency is 100%. The Pb²⁺ concentration and the voltage efficiency of each cell (shown in figure 25) both drop to minimum at the same cycle number. For Na/-/-, concentration of Pb²⁺ is zero and the voltage efficiency is the lowest at cycle number 44. For Na/Bi/Bi, this failure occurs at cycle number 25 and Na/-/B fails at cycle number 61. For the divided cells then, the voltage drop, and cell failure, is caused by insufficient Pb²⁺ present in solution to sustain the reaction.

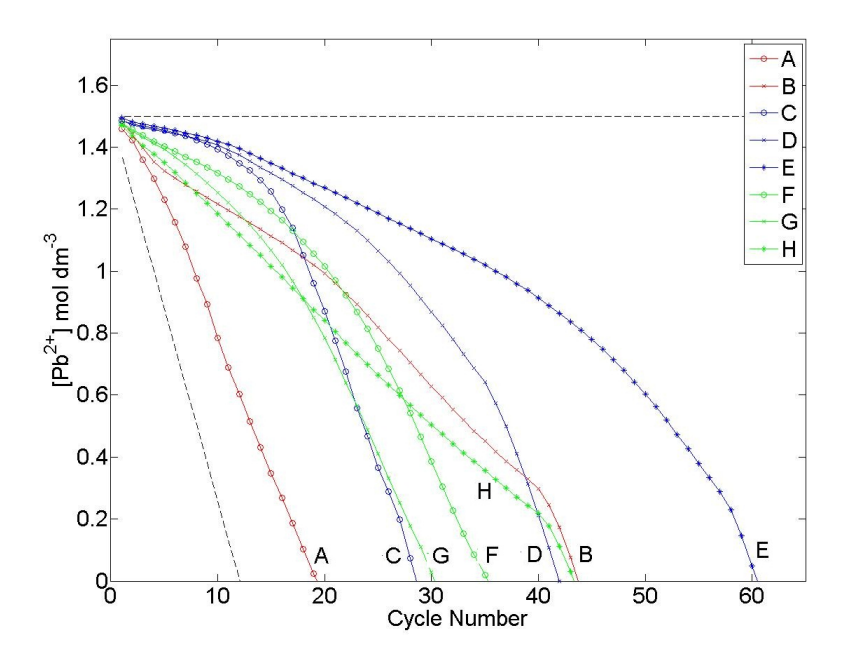


Figure 29: Concentration of Pb²⁺ in solution in the electrolyte for each battery at the end of each cycle. Coloured lines correspond to cells, black dashed lines to values 0 and 1 for coulombic efficiency. The cell lettering is shown in table 27.

Cell	Short	Cell voltag	ge	Voltag	Voltage		Cycle number to failure via:	
nomen-	nomen-	at cycle 1	/	efficienc	efficiency at			
clature		mV		cycle nur	cycle number:			
	clature	Charge	Discharge	1	10	$rac{ m Voltage}{ m efficiency} < 75\%$	$[\mathrm{Pb}_{2+}] = 0$	Electrical shorting
-/-/-	A	1950	1650	0.85	0.85	33	18	31
Na/-/-	В	1970	1650	0.84	0.87	43	44	n/a
-/Bi/Bi	C	2000	1550	0.78	0.81	27	27	27
Na/Bi/Bi	D	2060	1680	0.82	0.87	36	42	n/a
Na/-/Bi	E	2000	1590	0.80	0.85	59	61	n/a
-/Li/Li	F	2020	1620	0.79	0.85	43	35	n/a
Na/Li/Li	G	2010	1630	0.81	0.87	30	30	n/a
Na/Li/Bi	Н	1970	1620	0.74	0.87	42	44	n/a

Table 27: Cell voltages, voltage efficiencies and cycle number to failure for soluble lead acid batteries under charge and discharge cycles: constant current, 150 mA (6 mA cm $^{-2}$) for 600 s. Charge voltage cut-off 3 V, discharge voltage cut-off 1.2 V. 293 K.

6.4 Soluble static lead-acid battery: Summary and conclusions

The static soluble lead-acid battery concept has been successfully operated at low current densities (6 mA cm $^{-2}$) and low depth of charge and discharge (8%). The system demonstrates a high voltage efficiency of 0.85 for battery configuration E and was successfully operated for up to 61 cycles.

By investigating the failure modes of these batteries, a significant performance-reducing characteristic, material sludging, was identified and mitigated against by using a separator membrane. This prevented electrical shorting between the electrodes. The Nafion® NF115/H⁺ separator membrane alone increased the cycle life and the voltage efficiency significantly, but the biggest gains were made by using both the membrane and the Bi³⁺ additive. The Bi³⁺ additive increases charge efficiency at the positive electrode.

The separator membrane had two beneficial effects: 1) allows the use of different electrolytes at each electrode, which increases the cell cycle life and 2) prevents electrical shorting.

While liginsulphonic acid significantly increases the cycle life of the undivided cells, because it reduces electrical shorting, it has a detrimental effect on the divided cells, because it interferes with the membrane.

The cycle number was increased by a factor of nearly 2; from 31 cycles to 61 cycles, by using the membrane and including 10 mM of $\rm Bi^{3+}$ additive in the positive electrode chamber (cell Na/-Bi). The Nafion® membrane does not have a significant electrical resistance as cell voltages are equal for similar cells with and without the membrane.

The best performing cell, cell Na/-/Bi (membrane divided with Bi³⁺ additive) has been taken forward for additional studies in chapters 7 and 8.

7 Electrode studies: galvanostatic amperometry

The purpose of this experiment set is to identify the maximum current for each electrode. There are two reasons for this: to quantify the differences in electrode performance and allow electrode balancing, and to inform a suitable charge and discharge regime for a cell.

Electrodes used were carbon-polymer composite plates, which had been electrodeposited in lead (for use as the negative electrode) and lead dioxide (positive electrode). Deposition took place in the cell (as described in chapter 6), using the 1.5 M Pb²⁺ in aqueous CH₃SO₃H (1 M) electrolyte with ligninsuphonic acid 1 g l⁻¹ at 600 mA cm⁻²for 600 s.

The electrodes were subjected to galvanostatic amperometry at stepped potentials. The electrode potentials used are shown in table 28. Each sample was subjected to two constant potentials for 120 seconds in total; first with a potential corresponding to deposition for 60 seconds, and then a potential corresponding to dissolution for 60 seconds. In this way, each sample electrode was subjected to one battery 'charge' period and one 'discharge' period. The negative electrode potentials were applied to the lead-coated electrodes and the positive electrode potentials were applied to the lead-dioxide-coated electrodes. For example, figure 30 shows that each negative electrode was subjected to two constant voltage steps, one of which was -0.53 V vs. SCE for the first 60 seconds, and -0.43 V vs. SCE for the next and final 60 seconds. The response current was measured and recorded, and the limiting current was noted.

Each electrode was subjected to a deposition and a dissolution potential of equal overpotential (η). The overpotentials are calculated based on equilibrium potentials of 1.50 V for the positive electrode and -0.48 V for the negative electrode. These values are taken from voltammetry of lead in CH₃SO₃H (1 M). The negative electrode potential scan is presented in chapter 'Electrochemistry of Pb in solution'. The positive electrode potential scans are presented in [72]. The compositions of the electrolytes are not the same as that used in the cell experiments. The Pb²⁺ and H⁺concentrations both affect the value of the equilibrium potential. Therefore, the equilibrium potentials used are an estimation. In addition, the electrolyte concentration will vary during the reaction, so the equilibrium potential will change during the experiment. Six different electrolyte concentrations were used, and five electrolytes with the Bi³⁺additive. These are shown in table 29.

Electro	ode Potent	ials / V vs. SCE
Negative	Positive	Positive with Bi ³⁺
-	0.80	0.80
-	1.00	1.00
-	1.10	1.10
-0.18	1.20	1.20
-0.23	1.25	1.25
-0.28	1.30	1.30
-0.33	1.35	1.35
-0.38	1.40	1.40
-0.43	1.45	1.45
-0.53	1.55	1.55
-0.58	1.60	1.60
-0.63	1.65	1.65
-0.68	1.70	1.70
-0.73	1.75	1.75
-0.78	1.80	1.80
-	1.90	1.90
=	2.00	2.00
-	2.20	2.20

Table 28: Galvanostatic Amperometry experimental conditions: potentials.

	Electrolyte Concentration / M								
N	egative	P	ositive	Positive with Bi ³⁺					
Pb^{2+}	CH ₃ SO ₃ H	Pb^{2+}	$\mathrm{CH_{3}SO_{3}H}$	Pb^{2+}	$\mathrm{CH_{3}SO_{3}H}$	Bi ³⁺			
0.01	1.00	0.01	1.00	0.01	1.00	0.01			
0.10	1.00	0.10	1.00	0.10	1.00	0.01			
0.50	1.00	-	-	_	-	-			
0.75	1.00	0.75	1.00	0.75	1.00	0.01			
1.00	1.00	1.00	1.00	1.00	1.00	0.01			
1.50	1.00	1.50	1.00	1.50	1.00	0.01			

Table 29: Galvanostatic Amperometry experimental conditions: electrolytes.

7.1 Electrolyte concentration effects

Negative Electrode Figure 30a shows the current response of the negative electrode to the stepped potentials in a 0.01 M Pb²⁺ solution. The first 60 seconds, which correspond to Pb deposition from the consumption of Pb²⁺, begin with a reduction current peak that decays to a low negative constant current (1.2 mA cm⁻² after 30 s at -0.78 V). The current is extremely low as there is very little available Pb²⁺ in solution to supply the reaction: any current that passes is a result of diffusion of Pb²⁺ from the bulk electrolyte to the electrode surface. From 60 seconds onwards, which corresponds to dissolution of Pb, there is again a current peak. However, this is an oxidation current with much higher magnitude (206 mA cm⁻² after 6 s at -0.18 V), which then decays to a constant current plateau before again decaying to zero. The current magnitudes are greater at increased overpotentials, and the length of time that the plateau occurs also decreases in time. For example, when the applied potential is -0.43 V (an overpotential of 0.05 V assuming the equilibrium potential is -0.48 V), the current plateau begins to drop at around 68 s, while at

-0.38 V ($\eta = 0.10$ V) the current plateau lasts roughly 50 s. This second decay, where the current plateau falls to zero, corresponds to the total consumption of active material on the electrode surface.

In electrolytes with higher [Pb²⁺], for example the 1.5 M Pb²⁺ as shown in figure 30 b, this plateau does not decay as there is sufficient active material on the electrode surface from the preceding deposition period. In addition, when there is a high [Pb²⁺], the deposition current is greater than the dissolution current (221 mA cm⁻² after 30 s at -0.78 V compared to 138 mA cm⁻² after 30 s at -0.18 V). This higher deposition current is a result of the high availability of Pb²⁺ ions at the electrode surface; and conversely, the dissolution current is reduced due to the high [Pb²⁺], which is close to the solubility limit of Pb²⁺ in CH₃SO₃H (1 M), which must diffuse to the surface therefore this is a diffusion and [Pb²⁺] controlled process.

Figure 30 b shows an interesting phenomenon: the experiment set at -0.53 V and -0.43 V shows a reduction current (below the 0 current line), when, if it were above the equilibrium potential, it should be oxidising. This demonstrates that the equilibrium potentials used in this experiment are inaccurate for this electrolyte concentration. At that electrolyte concentration, -0.43 V is still below the equilibrium potential.

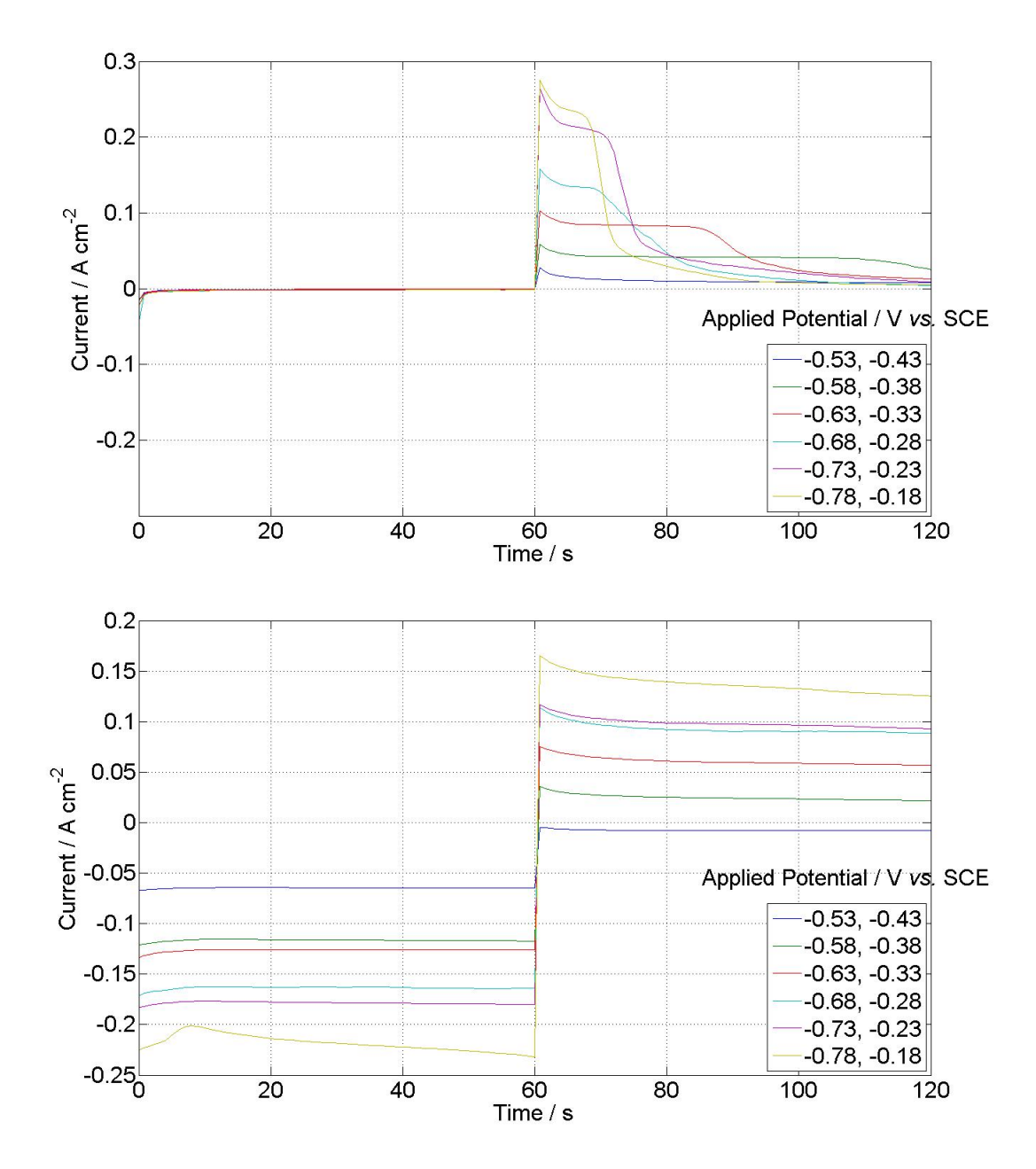


Figure 30: Negative electrode current response to constant, stepped potentials. a Electrolyte: $0.01~\mathrm{M~Pb^{2+}}$ in aqueous $\mathrm{CH_3SO_3H}$ (1 M). b Electrolyte: $1.5~\mathrm{M~Pb^{2+}}$ in aqueous $\mathrm{CH_3SO_3H}$ (1 M).293 \pm 2 K. The applied potentials are shown in the figure legend.

The effect of electrolyte concentration on current response at the negative electrode can be most clearly seen in the 3D plots in figure 31. The plot shows the limiting current as a function of both electrolyte concentration and overpotential.

In general, as the Pb^{2+} concentration increases, the limiting current increases. The lowest currents are shown in the 0.01 M Pb^{2+} solution. However, there is an anomaly at 0.75 M Pb^{2+} : the greatest currents shown at each overpotential are those taken in this concentration. In a battery using 1.5 M Pb^{2+} electrolyte, this corresponds to 50 % state of charge, assuming that active material utilisation is 100 %.

In addition, as the overpotential increases, the limiting current increases. This is a result of the migration of the Pb²⁺ ions within the potential field. As the overpotential increases,

the potential field becomes stronger and attracts the potsitive Pb^{2+} ions more strongly to the negative electrode. This increases the Pb^{2+} mass transport rate, and allows the reaction rate to increase.

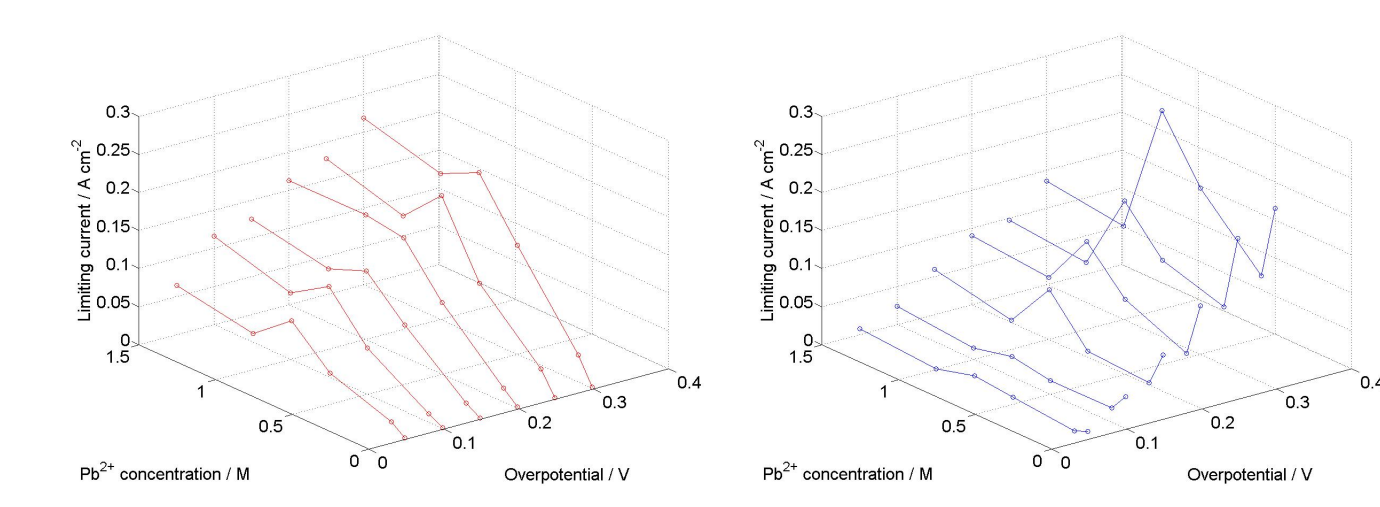


Figure 31: Lead electrode limiting currents as a function of applied overpotential and electrolyte $[Pb^{2+}]$. Potentials range from -0.78 to -0.18 V vs. SCE, where the equilibrium potential is assumed to be -0.42 V. Electrolyte $[Pb^{2+}]$ ranged from 0.01 M to 1.5 M Pb^{2+} in aqueous CH_3SO_3H (1 M). 293 \pm 2 K. Left: deposition potentials; right: dissolution potentials.

Positive electrode Figure 32 a shows the positive electrode response in 0.75 M Pb²⁺ in aqueous CH₃SO₃H (1 M). The deposition current is oxidative, which begins with a slight peak and then decays to a plateau, which is more pronounced at higher overpotentials. The current response is significantly lower for the positive electrode, because the positive electrode has a higher deposition overpotential than the negative electrode. [72] For example, the highest deposition current for lead dioxide is 265 mA cm⁻²at an overpotential of 0.7 V (2.2 V): for lead deposition, only 0.3 V overpotential is required to achieve a similar current (216 mA cm⁻²). The overpotential range was extended to achieve similar currents to the negative electrode: i.e. to achieve similar currents at each electrode, a much greater overpotential must be applied to the positive electrode than the negative electrode.

The effect of the 10 mM Bi³⁺ additive, as seen in figure 32 b, is to reduce the current further: at 1.8 V, the deposition current is 80.1 mA cm⁻² for Pb²⁺ only but 66.7 mA cm⁻² with the bismuth additive. Likewise for dissolution: at 1.2 V, the current is 19.8 mA cm⁻² without the additive compared to 9.95 mA cm⁻² with the additive. At 0.01 M Pb²⁺ however, the Bi³⁺ additive affects the positive electrode by increasing the deposition current to 24.3 mA cm⁻² (from 13.6 mA cm⁻² after 30 s at 1.8 V), but reduces the dissolution current to 0.358 mA cm⁻² (from 8.73 mA cm⁻² after 30 s at 1.2 V).

The electrolyte concentration effects on the positive electrode limiting currents are less pronounced than for the negative electrode. Figure 33 shows a shallower gradient over the $[Pb^{2+}]$ axis than in figure 31. There is less dependence on $[Pb^{2+}]$, which shows that for this electrode, the availability of Pb^{2+} is not the limiting factor; in this case the reaction kinetics are limiting the reaction rate. In general, there is a slight increase in limiting current as the $[Pb^{2+}]$ increases, for both deposition and dissolution, and as with the negative electrode, there is a slight peak in limiting current at 0.75 M.

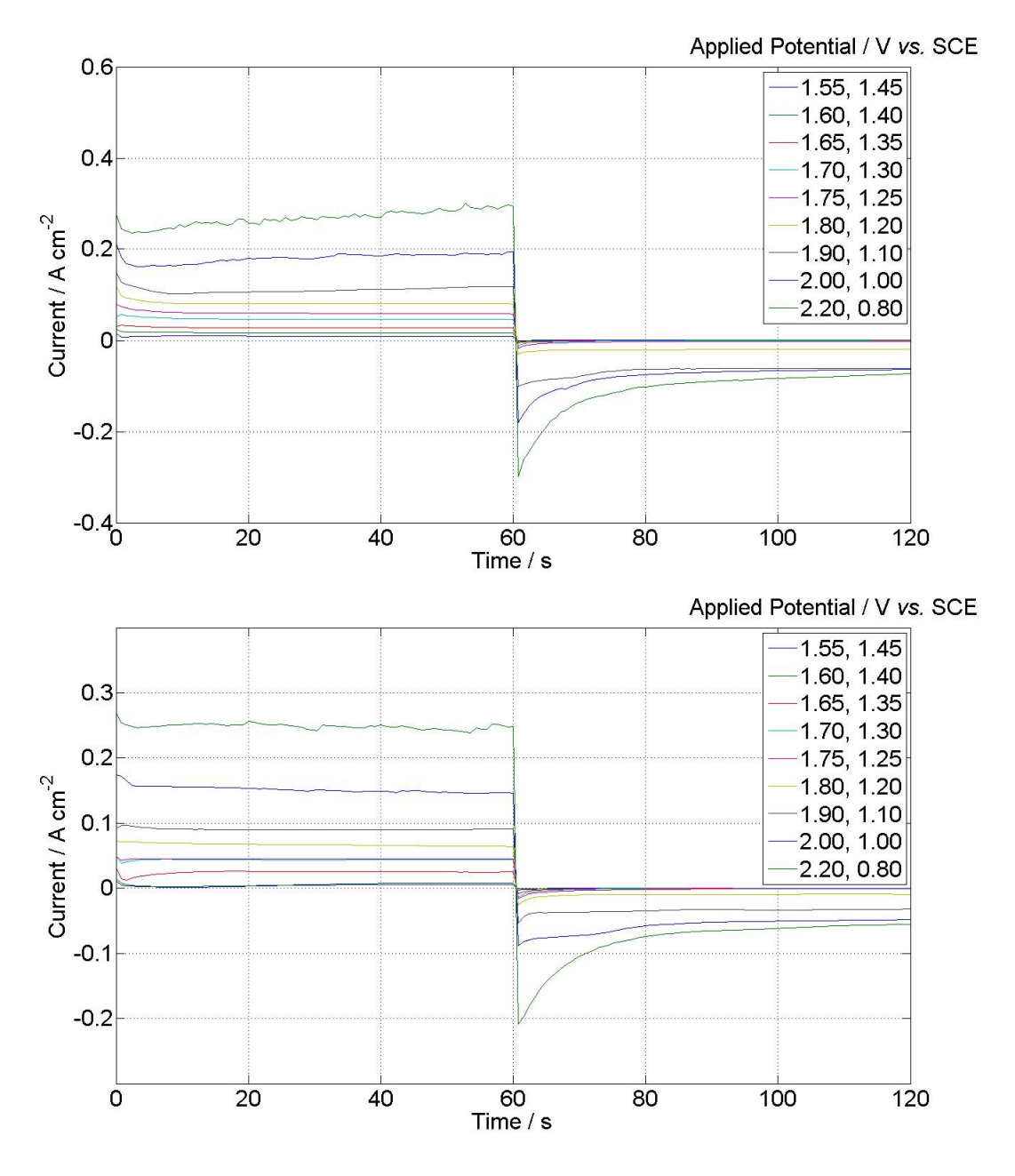


Figure 32: Positive electrode current response to constant, stepped potentials. a Electrolyte: $0.75~\mathrm{M~Pb^{2+}}$ in aqueous $\mathrm{CH_3SO_3H}$ (1 M). $293~\pm~2~\mathrm{K}$. b Electrolyte: $0.75~\mathrm{M~Pb^{2+}}$ in aqueous $\mathrm{CH_3SO_3H}$ (1 M) with 10 mM $\mathrm{Bi^{3+}}$. $293~\pm~2~\mathrm{K}$. The applied potentials are shown in the figure legends.

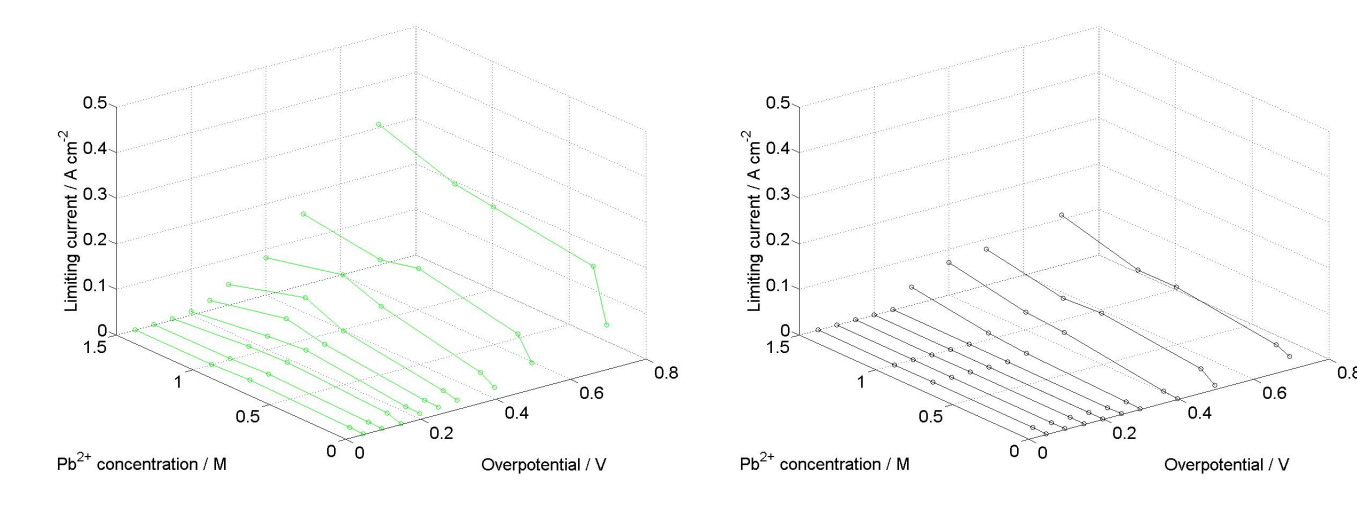


Figure 33: Lead dioxide electrode limiting currents as a function of applied overpotential and electrolyte [Pb²⁺]. Potentials range from 0.80 to 2.20 V vs. SCE, where the equilibrium potential is assumed to be 1.50 V. Electrolyte [Pb²⁺] ranges from 0.01 M to 1.5 M Pb²⁺ in aqueous CH₃SO₃H (1 M) with 10 mM Bi³⁺. 293 \pm 2 K. Left: deposition potentials; right: dissolution potentials.

Limiting current /	Negative	electrode	Positive electrode		
$ m mA~cm^{-2}$	Deposition	Dissolution	Deposition	Dissolution	
$0.75~\mathrm{M~Pb^{2+}}$ in	156	151	46.6	0.400	
aqueous CH ₃ SO ₃ H					
(1 M)					
$0.75~\mathrm{M~Pb^{2+}}$ in	-	-	37.5	0.276	
aqueous $\mathrm{CH_3SO_3H}$					
(1 M) with 10 mM					
Bi^{3+}					

Table 30: Significant limiting currents: 0.75 M Pb²⁺, $\eta = 0.2$ V.

7.1.1 Summary

The limiting current at both the positive and negative electrode increases with overpotential. The negative electrode is more sensitive to Pb^{2+} concentration than the positive electrode, but both show a general increase in limiting current as the Pb^{2+} concentration increases, with a peak for both deposition and dissolution limiting currents at 0.75 M Pb.

The greatest limiting currents are found in electrolytes of 0.75 M Pb²⁺. At this concentration, and when $\eta = 0.2$ V, the limiting current is at the positive electrode: during deposition this is 37.5 mA cm⁻² and during dissolution, 0.276 mA cm⁻². At equal [Pb²⁺] and η , the negative electrode limiting current is 156 mA cm⁻² during deposition and 151 mA cm⁻² during dissolution. These values are shown in table 30.

7.2 Limiting factors: mass transport and electrode kinetics

For comparison, the negative and positive electrode deposition and dissolution current magnitudes are plotted in figures 34 a and b. The trend of increasing limiting current with applied overpotential shown in figures 30 and 32 can be seen in figures 34 a and b. In addition, the

magnitude of these currents can be easily compared.

For the negative electrode (figure 34 a) in 0.01 M Pb²⁺ solution, the dissolution currents are significantly greater than the deposition currents at similar overpotentials. For example, when $\eta=0.2$ V, the dissolution current is 134 mA cm⁻², while the deposition current is 1.94 mA cm⁻². In this extreme case, the dissolution current is greater because the deposition current is limited by availability of Pb²⁺ at the electrode surface. At such a low bulk Pb²⁺ concentration, the Pb²⁺ must diffuse towards the electrode surface. The rate of this mass transport is linked to the electrolyte viscosity, coordination number of reactants and ionic mobility. At high Pb²⁺ concentrations, the dissolution current is lower than the deposition current at similar overpotentials. (For 1.5 M Pb²⁺, $\eta=0.2$ V, current is 90.2 mA cm⁻² during dissolution and 164 mA cm⁻² during deposition. For 0.75 M Pb²⁺, $\eta=0.2$ V, current is 151 mA cm⁻² during dissolution and 156 mA cm⁻² during deposition). The reduction in dissolution current at high concentrations is due to the solution concentration approaching the solubility limit for lead ions, which restricts the dissolution current. The greatest dissolution currents are shown at concentrations of 1.5 M, 0.75 M and 0.01 M; the deposition currents are greatest at 1.5 M and 0.75 M.

For the positive electrode (figure 34 b), the trends are similar, both for increasing current with overpotential but also that the deposition currents are higher for the higher concentration electrolytes, and the dissolution currents are higher for the lower concentration electrolytes. When compared to the negative electrode, the dissolution currents of the positive electrode are all of a lower magnitude: this confirms that the positive electrode kinetics are limiting during dissolution. When $\eta=0.2$ V, and 0.01 M Pb²⁺, dissolution current is 3.07 mA cm⁻² and deposition current is 0.078 mA cm⁻², two orders of magnitude lower than the negative electrode. This is consistent across electrolyte concentrations, and during both deposition and dissolution: see table 30. The Bi³⁺ additive lowers the positive electrode limiting currents further: at the same concentration and overpotential, the deposition current is 37.5 mA cm⁻² and the dissolution current is 0.276 mA cm⁻².

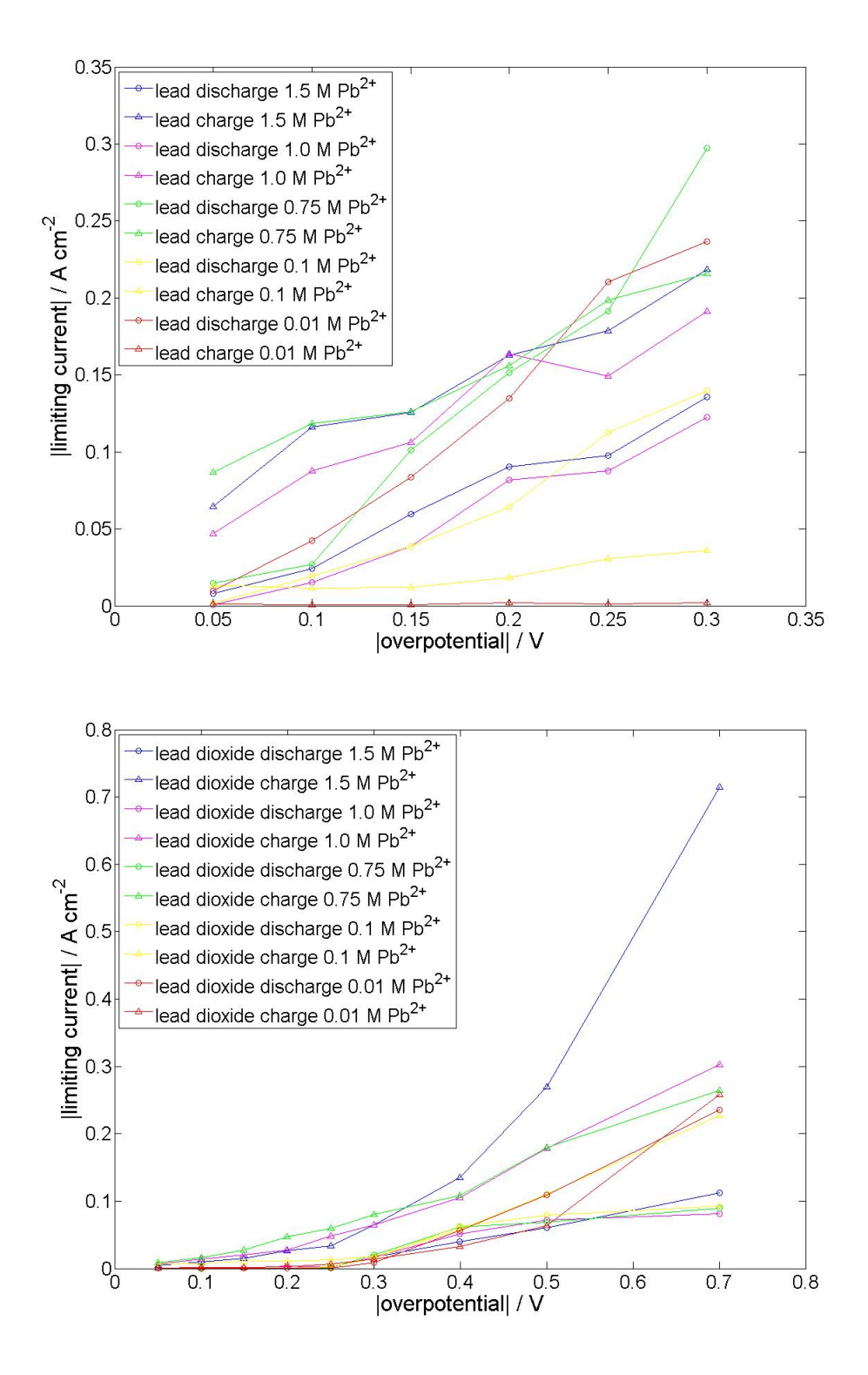


Figure 34: Lead (a) and lead dioxide (b) electrode limiting currents as a function of applied overpotential and electrolyte [Pb²⁺]. Potentials range from 0.80 to 2.20 V vs. SCE, where the equilibrium potential is assumed to be 1.47 V. Electrolyte [Pb²⁺] ranged from 0.01 M to 1.5 M Pb²⁺ in aqueous CH₃SO₃H (1 M). 293 \pm 2 K. Left: deposition; right: dissolution.

7.3 Conclusions

The purpose of this experiment set is to identify the maximum current for each electrode, so that the cells developed in chapter 6 may be improved. There are two avenues for performance improvement: 1) balance electrode currents and 2) use a suitable charge and discharge regime, including electrolyte concentration. The conclusions found here will inform the next stage of soluble static cell development.

Electrode performance and balancing The positive electrode is limiting during both deposition and dissolution, it exhibits currents (mA cm⁻²) at least two orders of magnitude lower than the negative electrode. In order to achieve similar current densities at both electrodes, the overpotential at the positive electrode is more than twice that at the negative electrode.

At the negative electrode, mass transport is the limiting factor. To mitigate this effect, the distance from the bulk electrolyte to the electrode surface should be reduced. Three dimensional (3D) carbon felts are available which have a surface area in the region of 20 000 m² m⁻³; assuming electrode thickness of 0.01 m, these would increase the the surface area by 200 times, and reduce mass transport effects

.

Cell cycling regime The optimum electrolyte concentration for cell operation is 0.75 M [Pb²⁺]. This concentration therefore offers a good balnace of viscosity, coordination number of reactants and ionic mobility. Therefore, either 0.75 M Pb²⁺ solution should be used, or to maximise battery capacity, which would use a 1.5 M Pb²⁺ solution (this is the maximum solubility of Pb²⁺ in aqueous CH₃SO₃H (1 M) then the cell should be operated at 50 % state of charge (SoC). Therefore, a cell cycling regime where the SoC is around 50 % would yield the highest current densities.

The greatest current densities are around 150 mA cm⁻² for both deposition and dissolution of the negative electrode (at 0.75 M Pb²⁺ and an overpotential of 0.2 V). The cell cycling regime should use this current density, if a 3D positive electrode is used.

8 Results: Soluble static lead-acid battery. Further studies

Further cell configurations (single cells and four cells) and test regimes were used in order to inform the design of an optimised static soluble lead acid cell. Eight cell configurations and two test regimes were used: the high current test and the s-HEV test. The efficacy of using 3D electrodes, percentage 3D electrode compression and the operating currents were investigated.

Cells were constructed using two electrodes, called 1-cells as they have one electrode chamber; and five electrodes with four electrode chambers in a bipolar arrangement, called 4-cells. The configuration of these cells, including electrolyte chamber volume and electrode structre in shown in table 31. Some cells used a planar (2D) carbon polymer composite electrode, while others used a carbon felt (3D) electrode. The felt was selected in order to btoh increase the electrochemically active surface area, and to reduce the distance from the bulk electrolyte to the electrode surface. This distance directly affects the mass transport rate and the electrical resistance in the system. Felt compression also acts to reduce this distance.

Cell nomenclature	Cell Voltage	Cell Elec-	Interelectrode	Negative	Positive
		trolyte	gap / mm	Electrode	Electrode
		${ m chamber}$			
		$\mathbf{volume} \ /$			
		$_{ m ml}$			
1-cell J	2	3.75	3	2D	2D
				(nickel)	
1-cell K	2	3.75	3	2D	2D
1-cell M	2	3.75	3	3D	3D
1-cell N	2	11.25	9	3D	3D
1-cell O	2	15.00	12	3D	3D
4-cell B	6	15.00	12	3D	3D
4-cell A	6	6.50	9	3D	3D

Table 31: Nomenclature of cells used in this chapter under the s-HEV cycle regime: 2D carbon polymer composite and 3D carbon felt electrodes, 2 V and 6 V cells with different interelectrode gaps. Electrolyte composition was 1.5 M Pb²⁺ in aqueous CH₃SO₃H (1 M) electrolyte for the negative electrode, and 1.5 M Pb²⁺ and 10 mM Bi³⁺ in aqueous CH₃SO₃H (1 M) for the positive electrode. The charge voltage cut-off was 2.5 V, discharge voltage cut-off 1.2 V for the 1-cells.

8.1 High current tests of 1-cells O

It was found that using 1-cells J at currents greater than 20 mA cm⁻² resulted in corrosion of the nickel negative electrodes (figure 35); hence the use of 1-cell O which has carbon polymer composite negative and positive electrodes. The current density was kept low in order to avoid detrimental effects. It has been shown that currents above 150 mA cm⁻² cause gas evolution and damage to the solid active material, and above 50 mA cm⁻² cracks begin to form in the active material. [55] It is also reported in the literature that at currents above 40 mA cm⁻² the deposits become loose. [24] The current range selected was from 6 mA cm⁻² to 72 mA cm⁻².



Figure 35: Corroded nickel negative electrode current collector taken from 1-cell J after constant current cycling at 20 mA cm⁻². In subsequent tests, 1-cell O was used.

In this set of experiments, the cell with 3D carbon felt inserted into both electrolyte chambers, in electrical contact with the carbon-polymer composite electrodes via cell compression. In this way, the electrode surface areas were increased significantly. In order to accommodate the carbon felt, the interelectrode gap was increased to 6 mm per electrode (12 mm total). The cells are referred to as 1-cells O. These 3D cells were subjected to high constant current cycle tests, where the current ranged from 6 mA cm⁻² to 72 mA cm⁻², as shown in table 32.

Current / mA	$ m Current / mA cm^{-2}$	Cycle Time / s	DoD / %
150	6	600	2.1
600	24	600	8.3
1086	43	600	15.0
1200	48	600	16.6
1809	72	600	25.0

Table 32: High constant current cycling test regime used with 3D 1-cells O. The applied charge and discharge currents, cycle times and corresponding DoDs are listed. The surface area is geometrical surface area. Electrolyte composition was 1.5 M Pb²⁺ in aqueous CH₃SO₃H (1 M) electrolyte for the negative electrode, and 1.5 M Pb²⁺ and 10 mM Bi³⁺ in aqueous CH₃SO₃H (1 M) for the positive electrode. The charge voltage cut-off was 2.5 V, discharge voltage cut-off 1.2 V. 293 K.

The DoD (depth of discharge) refers to the percentage of total battery charge used in the teststep, assuming 100 % utilisation of the Pb²⁺ in solution. As the current is increased, the total charge passed is increased and thus more solute active material from the electrolyte is converted to solid according to Faraday's Law.

A voltage against time plot for the type O single cell during cycling at 150 mA is shown in figure 8.1. The first charge shows the highest voltage, which decays exponentially from an initial peak at 2.12 V to 1.98 V. This high initial voltage is a result of the overpotential which results from the nucleation of the solid Pb and PbO₂ onto the carbon felt substrate. The charge voltage profiles change shape with progressing cycles: cycle 2 begins with a slight peak at 1.91 V which then falls to a trough at 1.90 V briefly before increasing to a constant 1.94 V for the final 200s of charge. Each subsequent charge period exhibits a similar behaviour, however the initial voltage and the final voltage both decrease as cycles progress, converging to a constant charge voltage of 1.87 V

by cycle number 14. This charge voltage profile, with an initial trough, is common in the soluble lead system, and is an artefact of positive electrode 'sludging' (described in previous chapters and here [39]). There are several effects of sludging: 1) a decrease of Pb²⁺ concentration in solution; 2) an increase of H+ concentration in solution; 3) an increase in electrolyte viscosity; 4) a decrease in the charge reaction potentials. The composition of this sludge has been investigated via XRD in a different study, and the results show that it is either PbO or PbO₂, but it is not possible to say with any certainty exactly what the composition of these leady oxides are [39]. These leady oxides are more readily oxidised to PbO₂ than the Pb²⁺, which accounts for the charge voltage at 1.90 V: the Pb²⁺ conversion to PbO₂ reaction occurs at 1.98 V. However, it is not completely reversible, and as the cycles progress, the sludge accumulates, and the PbO begins to dominate the Pb²⁺ in PbO₂ formation. This is of benefit to the voltage efficiency of the battery. [54, 24] Another effect of the sludge accumulation is a change in H⁺ concentration in the electrolyte. The concentrations of both the H⁺ and Pb²⁺ will affect the voltage of the battery, according to the Nernst equation 9. As the voltage stabilises after 14 cycles, it can be assumed that the concentrations of these solutes remain constant. Therefore, the sludge is participating in the positive electrode reaction.

$$E0 = EoPbO2/Pb2 + -EoPb2 + /Pb - \frac{2.3RT}{F}logcPb2 + -\frac{4.6RT}{F}logcH + \\ (9)$$

The discharge voltages follow a consistent pattern; beginning at 1.7 V, there is a smooth curve down to 1.6 V before a rapid drop to the lower voltage cut off value. The gradient of the discharge voltage gives an indication of the internal resistance of the cell. The discharge gradients are slightly steeper in these 3D cells than for the 2D cells.

The voltage efficiency (table 33) generally increases as the cycles progress, mostly as a result of the charge voltage decreasing. There are also effects from the discharge: for example, under the 600 mA test regime, the cell discharges at 1.61 V at cycle 10 and 1.62 V at cycle 20. These cells improve in performance as the cycles progress. As the applied current density increases, the voltage efficiency decreases. This is a result of the IR drop, which results in an increasing overpotential: for example, during cycling at 150 mA, the overpotential at cycle 10 is 0.28 V, at 600 mA it is 0.31 V, and at 1086 mA it is 0.50 V.

While the voltage efficiency decreases at increased current, the charge efficiency (table 33) increases as the applied current increases, being greatest for the 1086 mA current test at 77 % at cycle number 10 and 94 % at cycle 20. At any higher current however, the battery fails (table 34): the upper voltage cut-offs are met immediately during 1800 mA cycling. At such high current, two phenomena arise: the IR drop increases, and the rate of mass transport may not be sufficient to support the reaction rate: both of these would cause the voltage to increase. However, it is interesting that the charge efficiency increases. This may be a result of the increased operating temperature (arising from the electrical resistance), resulting in a different composition of leady oxides which are more readily reduced. [39]

Although this definition of cycles to fail is extreme, it is related to the behaviour of the static lead cells. It was shown in Chapter 6 that the voltage efficiency of the static cells drops sharply at around the 75 % voltage efficiency point. This definition has been preserved throughout for consistency, despite being quite harsh.

In summary, the lower the current density, the more cycles the cells will peform. In order to sustain at least 10 cycles, the maximum operating current is 43 mA cm⁻².

Of particular interest is the comparison between this 1-cell O, with 3D carbon positive and negative electrodes and carbon current collectors, to the result from chapter 6 on the 2D electrode cells with a nickel negative current collector.

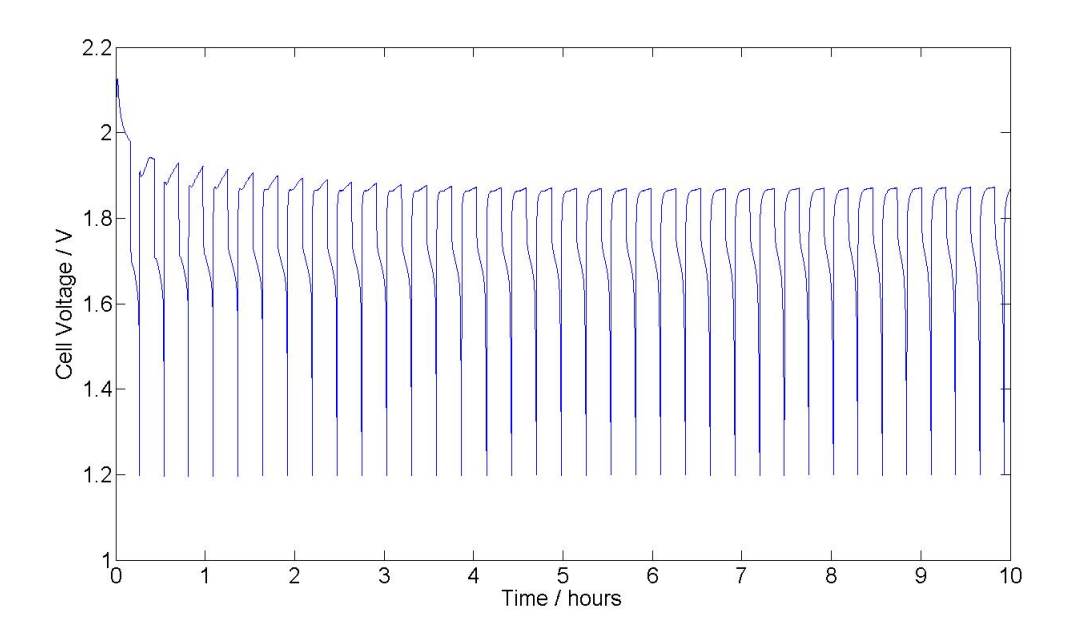


Figure 36: A voltage vs. time plot showing cell voltage during charge and discharge cycles of 1-cell O, a soluble lead acid cell. Constant current cycle regime at 150 mA (6 mA cm⁻²) for 600 s. Charge voltage cut-off 2.5 V, discharge voltage cut-off 1.2 V. 293 K. 1.5 M Pb²⁺ in aqueous CH₃SO₃H (1 M) electrolyte at the negative electrode and 1.5 M Pb²⁺ and 10 mM Bi³⁺ in aqueous CH₃SO₃H (1 M) at the positive electrode.

Current	Charg	ge voltag	ge /	Discharge voltage		Voltag	ge efficie	ncy	Charge efficiency		Cycle	Cycles to		
	V at c	ycle nur	nber	/ V at cycle		at cy	cle num	ber	at cy	cle num	ber	life /	fail /	
/ mA		number		number							hours	Voltage		
														efficiency <
	1	10	20	1	10	20	1	10	20	1	10	20		75%
150	2.01	1.88	1.87	1.67	1.69	1.70	0.83	0.90	0.91	0.60	0.63	0.69	18+	67+
600	1.96	1.92	1.94	1.59	1.61	1.62	0.81	0.84	0.84	0.75	0.63	0.70	8.2	31
1086	2.12	2.03	2.10	1.49	1.53	1.53	0.70	0.75	0.73	0.35	0.77	0.84	4.6	10
1809	-	-	-	-	-	-	-	-	-	-	-	-	0	0

Table 33: Charge and voltage efficiency for three selected cycles of 1-cells O with 3D electrodes under the high current cycle regime at 150, 600, 1086 and 1809 mA for 600 s. Charge voltage cut-off 2.5 V, discharge voltage cut-off 1.2 V. 293 K. 1.5 M Pb²⁺ in aqueous CH₃SO₃H (1 M) electrolyte at the negative electrode and 1.5 M Pb²⁺ and 10 mM Bi³⁺ in aqueous CH₃SO₃H (1 M) at the positive electrode.

Current	Cycle	Cycles
/ mA	life /	to fail /
	$_{ m hours}$	Voltage
		effi-
		ciency <
		75%
150	18+	67+
600	8.2	31
1086	4.6	10
1809	0	0

Table 34: Cycle life of 1-cells O with 3D electrodes under the high constant current cycling test regime.

8.1.1 Comparison of 2D and 3D cells: the 1-cells J and K

The 3D electrodes have had several effects on cell performance; the major effect is on the charge voltage. The voltage trough is not so pronounced in the 2D cells, which means that the 3D cells suffer more from sludging at the positive electrode. This affects both for the cycle life, and the voltage efficiency.

At similar current, the 3D cells offer an increased cycle life: at 150 mA, the cycle life of the 1-cell O is greater than 67 cycles while 1-cell J cycled for 61 cycles. The electrolyte volume in the 3D cells is greater than the 2D cells, hence the greater cycles to fail before Pb²⁺ depletion. This is verified during cycling at a similar DoD of 8.3 %, the 3D 1-cell O now only lasts 31 cycles.

The voltage efficiency of the 2D cell E is 77 % at cycle 1 and 85 % at cycle 10, whereas at the same current density the 3D 1-cell O has corresponding voltage efficiencies of 83 % and 90 %. This is due to the higher discharge voltage in the 3D 1-cell O, as shown in figure 37. Despite this advantage, the discharge voltage profiles are less stable in the 3D cells. The negative gradient on the 3D cells voltage plots is indicative of a greater electrical resistance. This is a result of the increased interelectrode gap.

The 3D cells offer a significant improvement on voltage efficiency, which is of paramount importance in battery operation.

Cell	Voltage	Voltage	Cycles to fail /
	Efficiency at	Efficiency at	Voltage
	cycle 1 / %	cycle 10 / %	efficiency <
			75%
1-cell O 3D	83	90	67+
1-cell J 2D	77	85	61

Table 35: Comparison of 1-cells K with 3D electrodes to 1-cells J with 2D electrodes and a nickel negative electrode, at 150 mA constant current cycling.

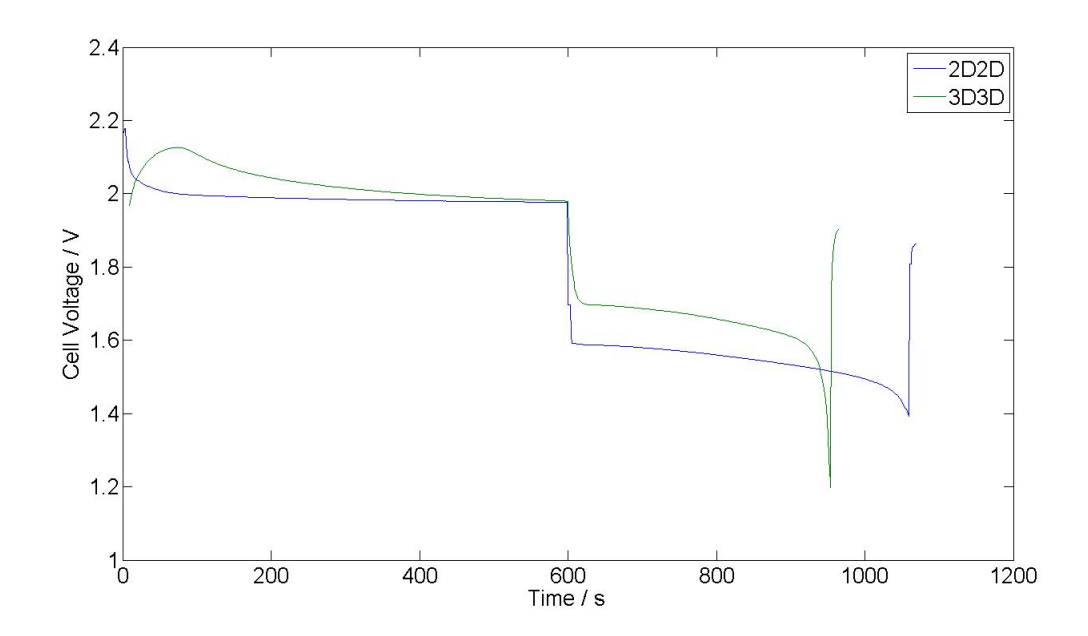


Figure 37: A voltage vs. time plot showing cell voltage during charge and discharge cycles of a 1-cell K and a 1-cell O static soluble lead acid cells. Constant current cycle regime at 150 mA (6 mA cm⁻²) for 600 s. Charge voltage cut-off 2.5 V, discharge voltage cut-off 1.2 V. 293 K. 1.5 M Pb²⁺ in aqueous CH₃SO₃H (1 M) electrolyte at the negative electrode and 1.5 M Pb²⁺ and 10 mM Bi³⁺ in aqueous CH₃SO₃H (1 M) at the positive electrode.

8.2 3D electrodes under HEV simulated cycling: 1-cells and and 4-cells

The simulated HEV (s-HEV) cycle test regime was used to simulate HEV operation. It is a much harsher test than than the 150 mAcm⁻² constant current testing used previously. Both the current density and the depth of discharge are greater. The test steps are shown in table 36. Chapter 7 Electrode Studies showed that the optimum electrolyte concentration is 0.75 M Pb²⁺, which corresponds to 50 % SoC (State of Charge) of the 1.5 M Pb²⁺ electrolytes that have been used in this study. In addition, s-HEV cycle regimes in the literature cycle around the 50 % SoC mark [52, 44, 47, 71, 65]. For these reasons, the s-HEV cycle regime used in this study operates around 50 % DoD. This test profile, shown in table 36, preserves the SoC over the range of electrolyte volumes by altering the charge and discharge times. The cells are charged to 100 % SoC at constant current, discharged at the same current to 50 % SoC, then cycled between 75 % and 25 % SoC.

Current / A	Current			Step time / s		
	$/ \mathrm{mA}$	SoC at end of cycle $/\%$	Condition			
	$ m cm^{-2}$			$3.75 \mathrm{ml}$	11.25 ml	15.00 ml
0.5	20	100	Charge	2171	6513	8684
		50	Discharge	1086	3256	4342
		75	Charge	543	1628	1108
		-	Cycle Start	-	-	-
		25	Discharge	1086	3256	4342
		75	Charge	1086	3256	4342
		-	Cycle End	-	-	-

Table 36: Constant current charge and discharge cycle regime s-HEV. Current, SoC, cell condition and step time are listed for each cell volume. The surface area is geometrical surface area. Electrolyte composition was 1.5 M Pb²⁺ in aqueous CH_3SO_3H (1 M) electrolyte for the negative electrode, and 1.5 M Pb²⁺ and 10 mM Bi³⁺ in aqueous CH_3SO_3H (1 M) for the positive electrode. The charge voltage cut-off was 2.5 V, discharge voltage cut-off 1.2 V. 293 K.

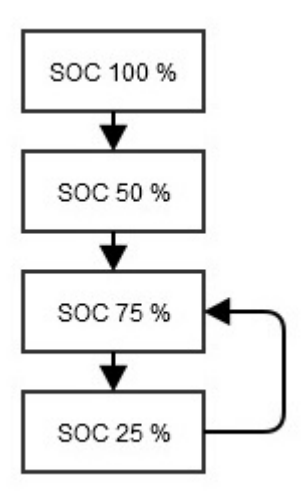


Figure 38: Constant current charge and discharge cycle regime s-HEV.

8.2.1 Electrode compression ratios

The s-HEV cycle profile was applied to 1-cells under three different electrode compression ratios: 0%, 25% and 75%.

The 75% compression 1-cell M struggled to perform in several tests. The upper charge voltage cut-off was met after only 58 seconds of charge, and subsequent cycles were impaired. The carbon felt was not completely wetted by the electrolyte and this adversely affected the performance. Figure 41 shows a plot for one of these cells, before it reached the lower voltage cut-off without recovery.

However, the cells under less compression performed well. The voltage - time plot for the 25 % compression 1-cell N is shown in figure 39. The charge profiles are similar to the high current cells, except that the first charge shows an initial lower voltage at 1.74 V for 230 s. Following this, the profile is similar: a relatively constant voltage trough of 2.0 V before a climb to 2.2 V. The cell reaches the end of the programmed time for both the first charge and discharge time. The first charge corresponds to 100 % charge, and the first discharge brings the SoC to 50 %.

This discharge occurs at an average of 1.7 V, but shows a steep gradient which indicates that the electrical resistance is high. The second charge, to 75 % SoC, occurs at roughly 1.9 V, but the second discharge, which should discharge the battery to 25 % SoC, shows a lower average voltage than the first, and the gradient has become steeper. As a result, it reaches the lower voltage cut off before the end of the discharge time. Therefore, the actual SoC of the battery is not 25 %. The actual SoC of the cell is recorded in table 37, where the SoC is calculated based on two assumptions. The first assumption is that all of the discharge current is used to reduce the active material, and the second assumption is that any charge current passed above 2.2 V is not used for Pb²⁺ oxidation, but is consumed in the parasitic side reaction of water hydrolysis. These assumptions are based on both the voltammetry for this system, and the physical evidence of gas evolution during charge. This phenomenon, of decreasing capacity as cycling progresses, is known as capacity fade.

The type N 1-cell performed 7 cycles to failure (mode: <75% voltage efficiency). At cycle number six, charge efficiency was 80.3%, considering the charge passed during each step of the cycle. It is clear from the figure that the cycle times are decreasing with each cycle. This charge regime is much harsher than the constant current regime, and the Pb^{2+} concentration is rapidly reduced due to leady oxides formation at the positive electrode. The failure mode of this cell is due to critically low Pb^{2+} concentrations.

The voltage profiles of the 1-cell O (0 % compression) are similar to the 1-cell N, except that the cycle times are extended to account for the increased electrolyte volume. This cell also charged at around 2.1 V and discharged at around 1.65 V for several hours over 13 cycles. At the 14th charge, electrolyte spills across the electrodes, causing short circuiting. This is a result of the gas evolution, which collects on the carbon felt and pushes the electrolyte out of the top of the cell. This can be clearly seen in the last charge of figure 40 as the charge voltage spikes. At the preceding cycle, charge efficiency was 88.5% and voltage efficiency was 77.4%.

In general, the voltage efficiency of the 1-cell N was higher than the larger 1-cell O at respective cycles. This is likely to be a result of improved electrical contact from the cell compression, and a smaller interectrode gap reducing the cell internal resistance. This is verified by the increased discharge voltage gradient exhibited by the 1-cell O, and that the upper voltage cut-off was met during the first charge (see figure 41). This high charge voltage reduces the voltage efficiency.

In summary, the 25 % compression offered the optimum amount of cell compression to allow good electrical contact, which increases voltage efficiency, but still maintains cell capacity.

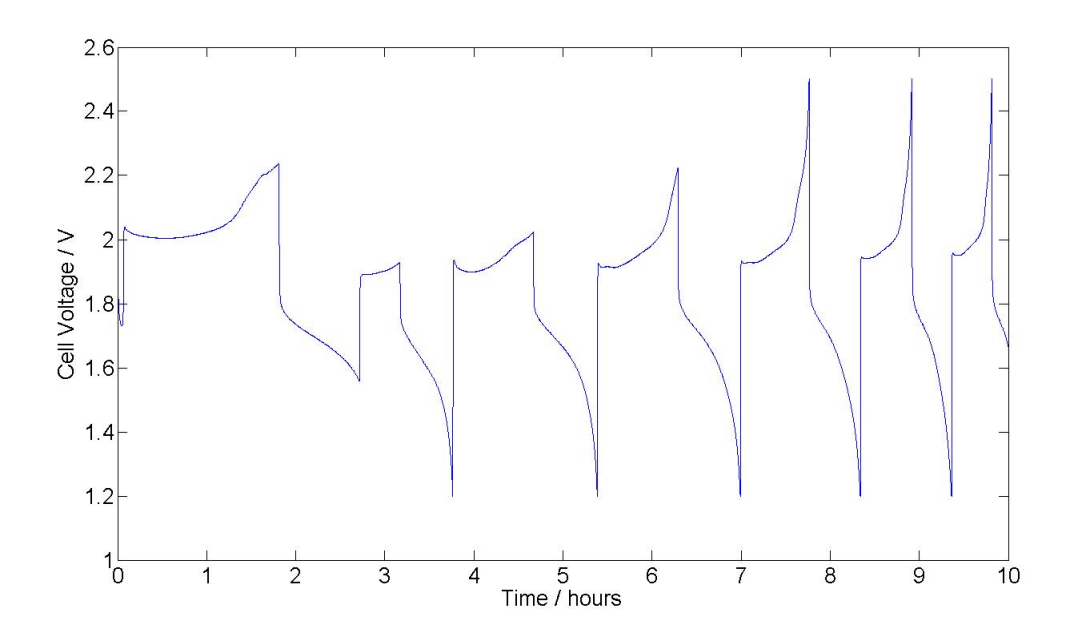


Figure 39: A voltage vs. time plot showing cell voltage during charge and discharge cycles of 1-cell N static soluble lead acid cell. s-HEV cycle regime at 500 mA (20 mA cm⁻²). Charge voltage cut-off 2.5 V, discharge voltage cut-off 1.2 V. 293 K. 1.5 M Pb²⁺ in aqueous CH₃SO₃H (1 M) electrolyte at the negative electrode and 1.5 M Pb²⁺ and 10 mM Bi³⁺ in aqueous CH₃SO₃H (1 M) at the positive electrode.

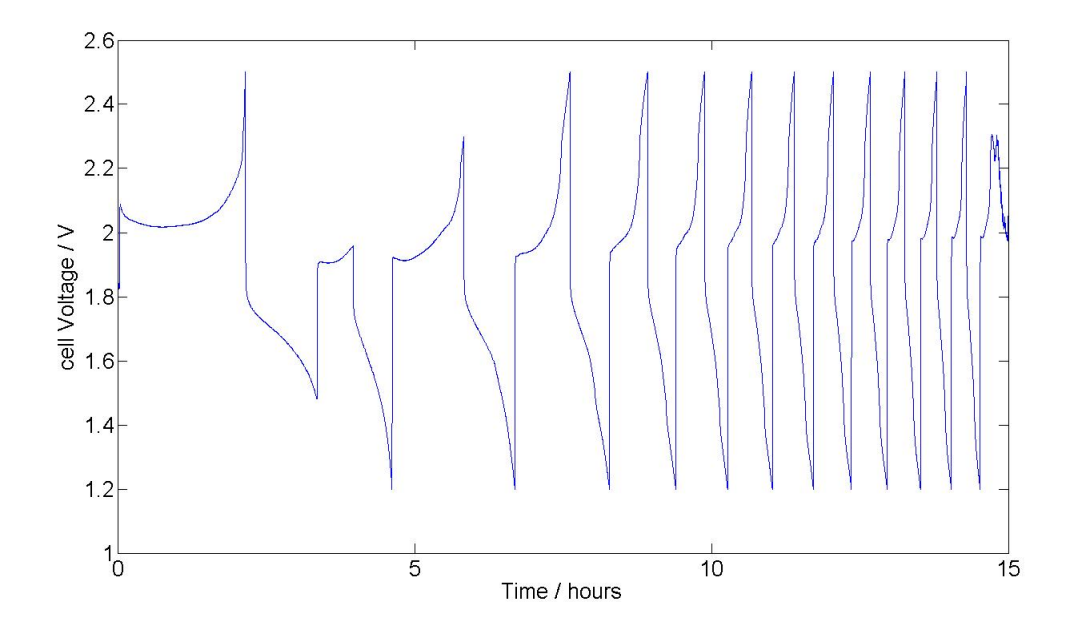


Figure 40: A voltage vs. time plot showing cell voltage during charge and discharge cycles of a 1-cell O 3D soluble lead acid cell. s-HEV cycle regime at 500 mA (20 mA cm⁻²). Charge voltage cut-off 2.5 V, discharge voltage cut-off 1.2 V. 293 K. 1.5 M Pb²⁺ in aqueous CH₃SO₃H (1 M) electrolyte at the negative electrode and 1.5 M Pb²⁺ and 10 mM Bi³⁺ in aqueous CH₃SO₃H (1 M) at the positive electrode.

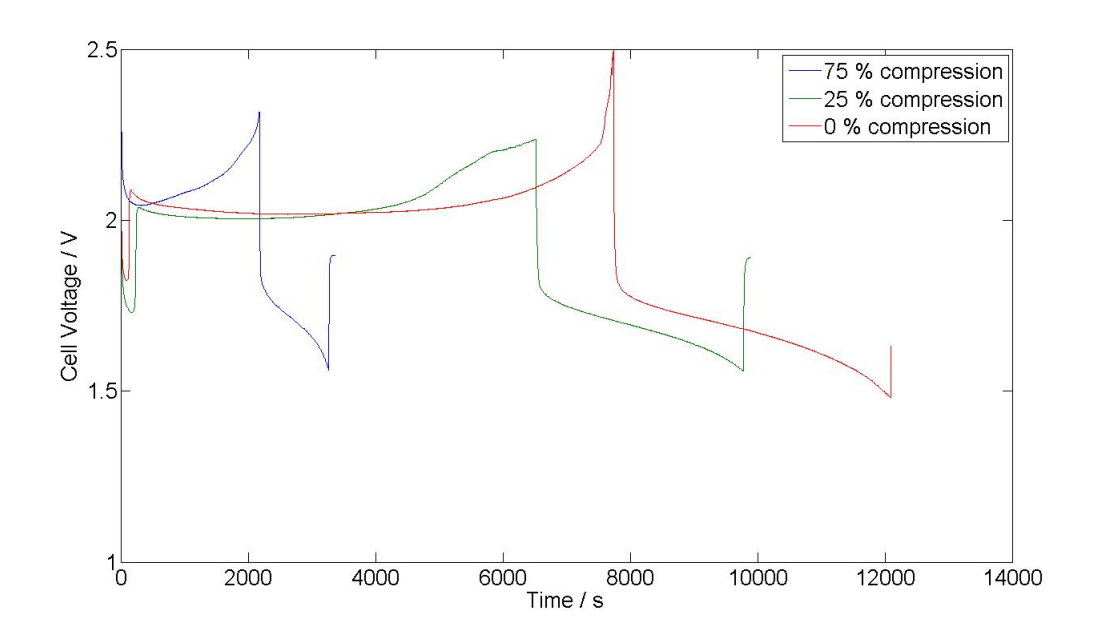


Figure 41: A voltage vs. time plot showing cell voltage during charge and discharge cycles of three soluble lead acid cells under three different compressions: 0, 25 and 75 %. These are 1-cells O N and M. Both electrodes are 3D carbon felt. The charge regime is s-HEV cycle regime at 500 mA (20 mA cm⁻²). Charge voltage cut-off 2.5 V, discharge voltage cut-off 1.2 V. 293 K. 1.5 M Pb²⁺ in aqueous CH₃SO₃H (1 M) electrolyte at the negative electrode and 1.5 M Pb²⁺ and 10 mM Bi³⁺ in aqueous CH₃SO₃H (1 M) at the positive electrode.

Cyalo number	State	Theoretical SoC / %	Actual SoC / %			
Cycle number	State	Theoretical SoC / /0	1-cell N	1-cell O		
1	Charge	100	72.1	86.9		
1	Discharge	50	21.8	36.8		
2	Charge	75	46.9	61.8		
2	Discharge	25	14.1	35.0		
3	Charge	75	64.2	76.9		
3	Discharge	25	23.8	41.2		
4	Charge	75	63.2	67.6		
4	Discharge	25	24.5	39.9		
5	Charge	75	53.9	53.5		
5	Discharge	25	27.5	33.7		

Table 37: Actual SoC for the 1-cells N and O. SoC calculations are based on: during charge; the time to reach a charge voltage above 2.2 V and during discharge; the time to reach the lower voltage cut-off. The discrepancy is caused by capacity fade.

8.2.2 4-cell s-HEV cycling: a bipolar 6 V battery

The single 1-cells were combined in a bipolar arrangement to form an approximately 6 V battery. This is a significant step as are few electrode materials can withstand operation at both negative and positive electrode potentials. This has been discussed at length in the literature review chapter.

4-cell A used 25 % electrode compression, and 4-cell B electrodes were not compressed. A

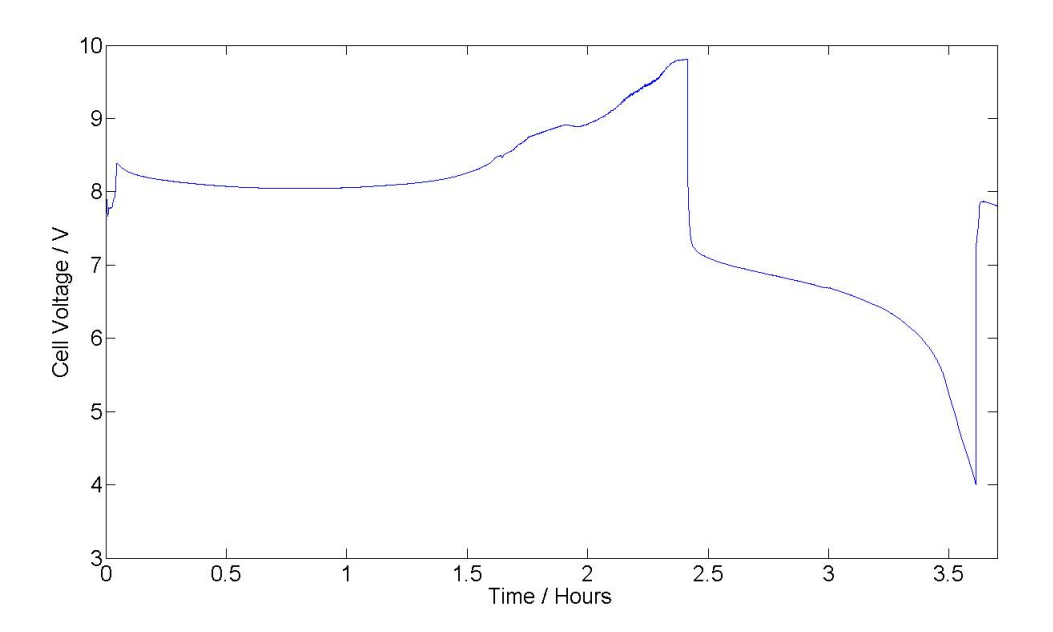


Figure 42: A voltage vs. time plot showing cell voltage during charge and discharge cycles of 4-cell B, a static soluble lead acid cell. s-HEV cycle regime at 500 mA (20 mA cm⁻²). Charge voltage cut-off 9.5 V, discharge voltage cut-off 4 V. 293 K. 1.5 M Pb²⁺ in aqueous CH₃SO₃H (1 M) electrolyte at the negative electrode and 1.5 M Pb²⁺ and 10 mM Bi³⁺ in aqueous CH₃SO₃H (1 M) at the positive electrode.

plot of 4-cell B is shown in figure 42. The voltage efficiency for this first cycle is 80 %. The charge efficiency is 50 % because the s-HEV charge regime involves charging to 100 % SoC and then discharging to 50 %: the cell followed the charge regime. The second charge does not complete. The second charge occurs at 7.7 V, but the second discharge time is much less than anticipated: capacity fade is high and the third charge does not succeed at all: the voltage peaks at 6.6 V and the cell immediately discharges. Inspection of the cell reveals that the electrolyte levels have risen (a result of electrolyte decompostion and bubble formation on the electrodes), flooded the cell and caused short circuiting. (Similar to 1-cell N.)

To mitigate against this effect in subsequent tests, the voltage-cut offs were modified, and the electrode chamber size and electrolyte volume were reduced by half. The modified electrodes are shown in figure ??. When this modified 4-cell A was tested, the current was also reduced by half to conserve the current density and SoC of the cell. The voltage-time plot for this modified battery is shown in figure 43. This 4-cell A shows good voltage efficiency for more than 32 cycles; it is consistently above 80 %. The charge efficiency is also good, however there is some capacity fade: after the fifth cycle, the total discharge time is less than half of the applied test regime (1627 s) at 774 seconds.

It can be seen in figure 44 that the electrolyte-level mark has risen on the electrode surface after the cycle regime shown in figure 43. The dimensions shown are in mm; the value of x is 25 mm and y varies between chambers from 36 to 50 mm. This gassing is much more severe than for the 1-cells. One possible reason for the increased gassing of the 4-cells is the higher operating temperature: the higher electrical resistance of the 4-cell battery results in an elevated temperature (this can be felt when handling the cell after cell operation).

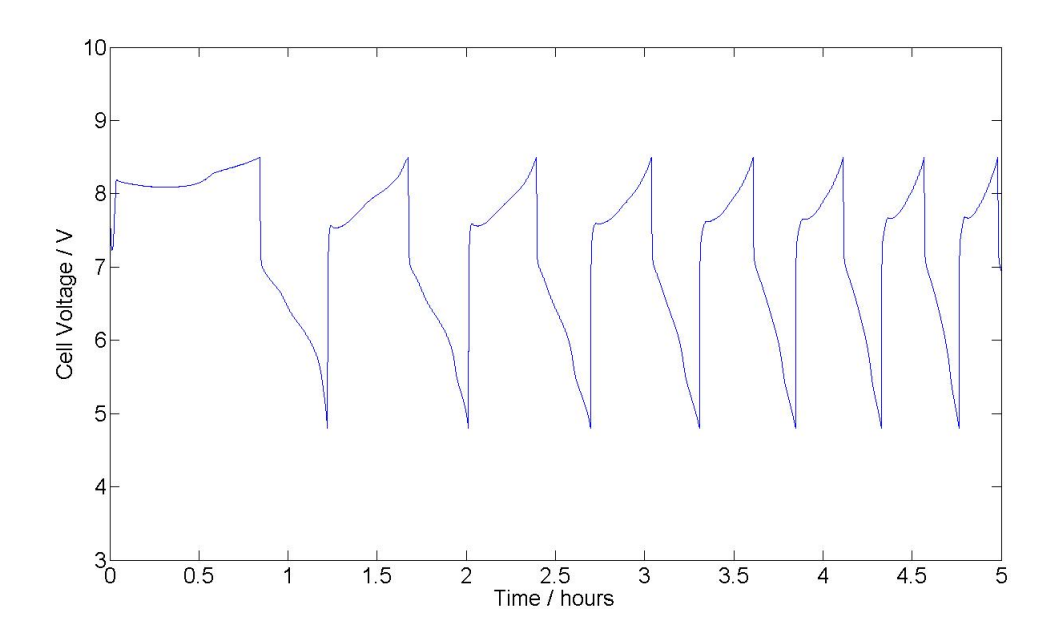


Figure 43: A voltage vs. time plot showing cell voltage during charge and discharge cycles of a modified 4-cell A, a static soluble lead acid cell. This cell has half the 3D electrode removed, and the electrolyte level is half of 4-cell A. s-HEV cycle regime at 250 mA (20 mA cm⁻²). Charge voltage cut-off 8.5 V, discharge voltage cut-off 4.8 V. 293 K. 1.5 M Pb²⁺ in aqueous CH₃SO₃H (1 M) electrolyte at the negative electrode and 1.5 M Pb²⁺ and 10 mM Bi³⁺ in aqueous CH₃SO₃H (1 M) at the positive electrode.

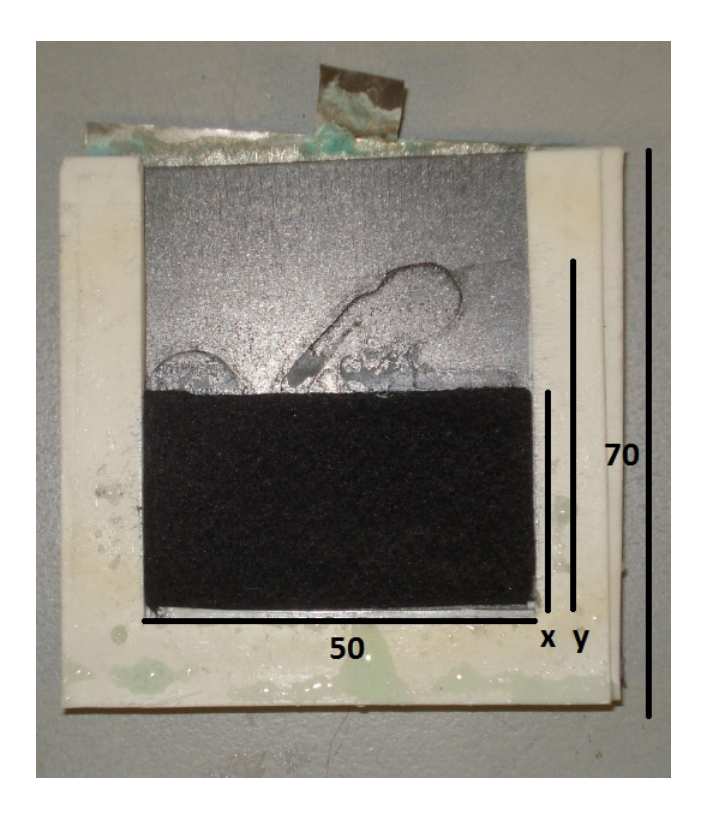


Figure 44: Electrolyte levels in the 5.6 ml 6 V battery have increased after s-HEV cycling.

Performance under s-HEV conditions	1-cell N	4-cell A (mod)
Number of cycles to failure (V $< 75\%$)	7	32 +
V Eff at cycle 1 / %	83	78
C Eff at cycle 5 / %	74	82
V Eff at cycle 5 $/$ %	84	82
Specific Capacity / Ah kg ⁻¹	3.17	5.54
Specific Capacity / Ah l ⁻¹	29.0	11.8
Capacity Fade at cycle 5 / %	36	45

Table 38: Comparison of performance for 1-cell N and 4-cell A under s-HEV tests.

8.2.3 Comparison of 1-cell and 4-cell

The modified 4-cell A performed well. It compares in performance to the similar 1-cell N favourably. Table 38 shows the values for the significant performance characteristics. The 4-cell outperforms the 1-cell in most measures: the cycle life, charge efficiency and specific capacity are all improved. The voltage efficiency is similar. The 4-cell is the most optimised configuration of this series of static soluble lead acid batteries.

One reason for the improved performance of the modified 4-cell A is the same electrolyte level increases that caused failure in the unmodified 4-cell A. As the electrolyte level increases, the current density decreases. It is well established that the lower the current density, the greater the cycle life.

8.3 Conclusions

A 6 V battery based on the static soluble lead acid system has been built and tested, and shown to cycle with a voltage efficiency of over 80 % for more than 32 cycles under a severe simulated HEV charge regime. The specific capacity was 5.5 Ah kg⁻¹.

Tests were conducted which demonstrate the benefits of using 3D carbon felt at both negative and positive electrodes. It was demonstrated that the voltage efficiency is increased when using 3D electrodes.

The compression of this felt was found to be optimal at 25 % under both high current and s-HEV tests. The voltage efficiency and the cycle life is improved.

The bipolar arrangement (4-cell) improved both the specific capacity and the charge efficiency. Cells in chapter 6 had a specific capacity of 1.78 Ah kg⁻¹; the bipolar battery showed an improvement of 147 %. The chage efficiency of the 1-cell O and the 4-cell A (mod) was 72 and 84 % respectively.

Issues that face this system include high internal resistance and parasitic side reactions which adversely affect the coulombic efficiency. Cell compression and reduced interelectrode gap helps to mitigate against this, as demonstrated in the comparison between the 1- cells O and N, which had 0 and 25 % cell compression respectively. In addition, the 4-cell showed improved charge efficiency over the 1-cells; this again is a result of a lower number of electrically resistive parts in relation to the electrode reaction surfaces.

					o o	L-		4	اي ا							
4-cell	A		25	11.25	Mass per parts	39.27	98.19	9.384	19.76	91.91	0.04	2.78	65.07	326.37	5.54	11.8
1-cell 4-			2		No.of parts	2	ro	∞	2	24	4	2		32(70	
	() () () () ()	3D (+ve)	0	15	Mass per parts	39.27	39.27	2.35	19.75	22.98	0.01	2.78	21.69	148.11	4.07	38.6
	0	3D(-ve) 3D (+ve)			No.of parts	2	2	2	2	9	-	2				
			25	11.25	Mass per parts	39.27	39.27	2.35	19.75	22.98	0.01	2.78	16.27	142.69	3.17	29.0
	Z				No.of parts	2	2	2	2	9	-	2				
	Т	L 2D(-ve) 3D (+ve)	n/a	15	Mass per parts	39.27	39.27	1.17	19.75	30.64	0.01	2.78	21.69	154.59	3.90	34.4
		2D(-ve)			No.of parts	2	23	1	2	∞	П	2		15	က်	60
	K D (+ve)		n/a	3.75	Mass per parts	39.27	39.27	0	19.75	2.66	0.01	2.78	5.42	114.2	1.32	12.7
		2D(ve) 2D (+ve)	n,	3.	No. of parts	2	2	0	2	2	П	2		711	Ï	12
		2D(ve) 2	n/a	3.75	Mass per parts / g	39.27	19.64	0	9.88	99:2	0.01	2.78	5.42	84.6	82	6.
	J		u/u	က်	No.of parts	2	1	0	1	2	-	2		≆	1.78	16.9
Cell type	Cell name	Electrode structure	Electrode compression / %	Simgle electrolyte chamber volume / ml	Mass / g	19.64	19.64	1.17	9.88	3.83	0.01	1.39	144.6 g per 100 ml	Total mass/g	Specific Capacity / Ah kg ⁻¹	Specific Capacity / Ah
					Material	carbon polymer composite	carbon polymer composite	carbon felt	silicone	silicone	Nafion	nickel foil	1.5 M Pb ²⁺ in aqueous CH ₃ SO ₃ H (1 M) (with 0.01 M Bi ³⁺ at the - ve electrode)			

Table 39: Specific energy of 1-cells and 4-cells. Table includes mass of individual components and electrolyte.

Structure

Part

Electrode

Electrode 3D Electrolyte

Current Collector

Separator

Spacer Gasket

8.4 Further work

The improved performance of the 4-cell is largely a result of the reduced number of components (and the cross section) in relation to the electrode reaction surface. The electrical resistance is reduced by using fewer components. In addition, using components of a lower electrical resistance will improve performance. This would involve using a thinner carbon-polymer composite electrode, and considering using a different carbon felt. The wettablilty of the felt was low; perhaps this had an adverse effect on cell performance.

In order to make informed improvements on this battery system, is it important to understand the nature of the reactions at each electrode. There is ambiguity of the electrochemistry at both electrodes: the negative electrode may be depositing an alloy of Pb and Bi, and the positive electrode deposit is comprised of an unknown composition of leady oxides. Further investigation is needed, particularly EDX analysis at the negative electrode.

Different charge and discharge regimes should be used to control the electrode reactions. An effect of the PbO build up was gas evolution at the electrodes, which was the failure mode of some of the 4-cells. Constant voltage charge would limit the accumulation of leady oxides, thus reducing the gas evolution.

The causes of gassing and electrolyte push-up need to be investigated. Perhaps it is an artefact of poor contact between the electrolyte and the substrate. Different, more wettable carbon felts should be used.

There is also scope for further work on selection of both additives and separator combinations. Particularly of interest is a separator which does not allow transport of Bi³⁺ ions, as the Nafion[®] NF115/H⁺ separator membrane is a cation transport membrane. The extent of the effect of cation transport is unknown in this system, and would benefit from investigation.

9 Conclusions

The aim of the project was to develop novel designs for lightweight lead acid batteries. Two approaches were taken: 1) a Thin Film battery was made with novel electrodes and 2) a static soluble lead acid battery with novel electrodes and novel electrolyte composition.

The Thin Film battery was made using novel coated scaffolds; this battery showed that the surface area to mass ratio of the active material is critical. The second two batteries used a novel electrode material (carbon polymer composite) and electrolyte (lead methanesulphonic acid). The first of these static soluble lead acid batteries used planar electrodes; this battery demonstrated the importance of using a separator membrane. As well as preventing cell failure by active material contact, this allows the use of electrode-specific additives. It was found that bismuth (at the negative electrode only) significantly improves the cycle life of the battery. The second design used a carbon felt electrode, which allowed increased current density. The electrolyte composition was found to be optimum at 0.75 M lead in 1 M methanesulphonic acid. These batteries were tested under simulated HEV cycle regimes, and had a much improved specific capacity over the Thin Film batteries. In addition, a 6 V bipolar static soluble lead battery was built and characterised.

It is clear that the proposed novel static soluble lead acid battery shows some potential, however there is plenty of scope for improvement.

Cell architecture: The cell architecture should be improved: currently it is clamped together and is unsealed. This is unsuitable for use in a moving vehicle! Glues should be used to fix the seals and produce a standalone battery. If the battery were to be sealed, suitable valves would have to be selected. The mass of these components would have to be carefully considered in order to keep the weight of the battery low. In addition, the cell electrodes could be even more lightweight. Now that we have established that a carbon-polymer composite is suitable for electrodes, other carbon-polymer composited can be considered. Recently, a thinner carbon polymer composite has come on the market: Sigracell PV10 (SGL group). This fluoropolymer has a density of 1.65 g cm⁻³ and an electrical resistivity of $< 10 \Omega$ mm, according to the data sheet. This could reduce the mass and volume of an improved battery.

3D electrodes: The carbon felt improved the battery performance, but other 3D electrodes could be compared to find an optimal porosity and fibre properites. The use of carbon foams is a well-worn path in the literature and there is a plethora of commercially available carbon felts and foams that could be investigated.

Cycle regime: a cycle profile which is more similar to the HEV profile would benefit the validity of the report. There are several industry standard regimes (PALC, PNGV) which could be used now that the capacity of the battery has been established.

References

- [1] Robert Alvarez and Martin Weilenmann. Effect of low ambient temperature on fuel consumption and pollutant and CO2 emissions of hybrid electric vehicles in real-world conditions. Fuel, 97:119–124, July 2012.
- [2] E Bashtavelova and A Winsel. Paste structure and its influence on the agglomerate of spheres parameters of the PbO2 electrode. *Journal of Power Sources*, 53:175–183, 1995.
- [3] R Bhardwaj. Lead acid battery with thin metal film (TMF®) technology for high power applications. *Journal of Power Sources*, 91:51–61, November 2000.
- [4] K. R. Bullock. Lead Acid batteries. Journal of Power Sources, 51:1-17, August 1994.
- [5] Y Chen, B Z Chen, L W Ma, and Y Yuan. Effect of carbon foams as negative current collectors on partial state of charge performance of lead acid batteries. *Electrochemistry Communications*, 10:1064–1066, July 2008.
- [6] Y Chen, B Z Chen, L W Ma, and Y Yuan. Influence of pitch based carbon foam current collectors on the electrochemical properties of lead acid battery negative electrodes. *Journal* of Applied Electrochemistry, 38:1409–1413, May 2008.
- [7] Y Chen, B Z Chen, X C Shi, H Xu, W Shang, Y Yuan, and L Xiao. Preparation and electrochemical properties of pitch-based carbon foam as current collectors for lead acid batteries. *Electrochimica Acta*, 53:2245–2249, January 2008.
- [8] A. Cooper. Development of a lead acid battery for a hybrid electric vehicle. *Journal of Power Sources*, 133:116–125, May 2004.
- [9] A Cooper, J Furakawa, L Lam, and M Kellaway. The UltraBattery: A new battery design for a new beginning in hybrid electric vehicle energy storage. *Journal of Power Sources*, 188:642–649, March 2009.
- [10] M Coux. Bipolar lead acid batteries: effect of membrane conductivity on performance. Journal of Power Sources, 78:115–122, March 1999.
- [11] A. Czerwinski, S. Obrebowski, J. Kotowski, Z. Rogulski, J. Skowronski, M. Bajsert, M. Przystalowski, M. Buczkowska Biniecka, E. Jankowska, and M. Baraniak. Hybrid lead acid battery with reticulated vitreous carbon as a carrier and current collector of negative plate. *Journal of Power Sources*, 195(22):7530–7534, November 2010.
- [12] A. Czerwinski, S Obrebowski, J Kotowski, Z Rogulski, J M Skowronski, P Krawczyk, T Rozmanowski, M Bajsert, M Przystalowski, and M Buczkowska Biniecka. Electrochemical behavior of negative electrode of lead-acid cells based on reticulated vitreous carbon carrier. Journal of Power Sources, 195(22):7524-7529, November 2010.
- [13] A Czerwinski, S. Obrebowski, and Z Rogulski. New high energy lead-acid battery with reticulated vitreous carbon as a carrier and current collector. *Journal of Power Sources*, 198:378–382, October 2012.

- [14] A. Czerwinski and M. Zelazowska. Electrochemical behavior of lead deposited on reticulated vitreous carbon. *Journal of Electroanalytical Chemistry*, 410:55–60, 1996.
- [15] Department for Transport. UK transport greenhouse gas emissions. Technical report, Department for Transport, 2009.
- [16] D R P Egan, C T J Low, and F C Walsh. Electrodeposited nanostructured lead dioxide as a thin film electrode for a lightweight lead acid battery. *Journal of Power Sources*, 196:5725– 5730, July 2011.
- [17] K. Ellis. The performance of Ebonex electrodes in bipolar lead-acid batteries. *Journal of Power Sources*, 136:366–371, October 2004.
- [18] European Commission. Reducing Emissions from Transport, 2014.
- [19] Jürgen Garche. Advanced battery systems: the end of the lead acid battery? *Physical Chemistry Chemical Physics*, 3(3):356–367, 2001.
- [20] B Grgur, V Ristic, M Gvozdenovic, M Maksimovic, and B Jugovic. Polyaniline as possible anode materials for the lead acid batteries. *Journal of Power Sources*, 180:635–640, May 2008.
- [21] W. X. Guo, D. Shu, H. Y. Chen, A.J. Li, H. Wang, G. M. Xiao, C. L. Dou, S. G. Peng, W. W. Wei, and W. Zhang. Study on the structure and property of lead tellurium alloy as the positive grid of lead acid batteries. *Journal of Alloys and Compounds*, 475:102–109, May 2009.
- [22] E. Gyenge, J. Jung, and B. Mahato. Electroplated reticulated vitreous carbon current collectors for lead acid batteries: opportunities and challenges. *Journal of Power Sources*, 113:388–395, 2003.
- [23] B. Hariprakash and S. A. Gaffoor. Lead acid cells with lightweight, corrosion protected, flexible graphite grids. *Journal of Power Sources*, 173:565–569, November 2007.
- [24] A. Hazza, D. Pletcher, and R. G. A. Wills. A novel flow battery: A lead acid battery based on an electrolyte with soluble lead (II) Part I. Preliminary studies. *Physical Chemistry Chemical Physics*, (6):1773–1778, 2004.
- [25] Ahmed Hazza, Derek Pletcher, and Richard Wills. A novel flow battery. A lead acid battery based on an electrolyte with soluble lead(II) IV. The influence of additives. *Journal of Power Sources*, 149:103–111, September 2005.
- [26] M Inai, C Iwakura, and H Tamura. Application of DSA-type electrodes to a positive grid in lead-acid batteries. *Journal of Applied Electrochemistry*, 8:515–522, November 1978.
- [27] IPCC. Climate Change 2007: Synthesis Report. Technical report, IPCC, Geneva, 2007.
- [28] Y Jang, N Dudney, T Tiegs, and J Klett. Evaluation of the electrochemical stability of graphite foams as current collectors for lead acid batteries. *Journal of Power Sources*, 161(2):1392–1399, October 2006.

- [29] Francisco José Jimenez-Espadafor, Juan José Ruiz Marín, José a. Becerra Villanueva, Miguel Torres García, Elisa Carvajal Trujillo, and Francisco José Florencio Ojeda. Infantry mobility hybrid electric vehicle performance analysis and design. *Applied Energy*, 88(8):2641–2652, August 2011.
- [30] W H Kao. Substrate materials for bipolar lead acid batteries. *Journal of Power Sources*, 70:8–15, 1998.
- [31] Wen-Hong Kao. Corrosion Resistant Coating for a Positive Lead Acid Battery Electrode.

 Journal of The Electrochemical Society, 139(11):L105, 1992.
- [32] H Karami, M Shamsipur, S Ghasemi, and M Mousavi. Lead acid bipolar battery assembled with primary chemically formed positive pasted electrode. *Journal of Power Sources*, 164:896–904, February 2007.
- [33] R. Kiessling. Copper stretch metal technology and applications. *Journal of Power Sources*, 19:147 150, 1987.
- [34] A Kirchev, N Kircheva, and M Perrin. Carbon honeycomb grids for advanced lead acid batteries. Part I: Proof of concept. *Journal of Power Sources*, 196:8773–8788, October 2011.
- [35] I. Kurisawa. Development of positive electrodes with an SnO2 coating by applying a sputtering technique for lead-acid batteries. *Journal of Power Sources*, 95:125–129, March 2001.
- [36] Rodney M Lafollette and Douglas N Bennion. Design fundamentals of High Power Density, Pulsed Discharge Lead Acid Batteries. Electrochemical Science and Technology, 137(12):3693-3701, 1990.
- [37] L T Lam. Failure mode of valve regulated lead-acid batteries under high rate partial state of charge operation. *Journal of Power Sources*, 133:126–134, May 2004.
- [38] L T Lam and R Louey. Development of ultra battery for hybrid electric vehicle applications. Journal of Power Sources, 158:1140–1148, August 2006.
- [39] X. Li, D. Pletcher, and F. C. Walsh. A novel flow battery: A lead acid battery based on an electrolyte with soluble lead(II) Part VII. Further studies of the lead dioxide positive electrode. *Electrochimica Acta*, 54(20):4688–4695, August 2009.
- [40] A Loyns, A Hill, K Ellis, T Partington, and J Hill. Bipolar batteries based on Ebonex technology. *Journal of Power Sources*, 144:329–337, June 2005.
- [41] M Lushina, Y Kamenev, V Leonov, and E Ostapenko. Use of expanded copper mesh grid for negative electrodes of sealed lead storage batteries. *Journal of Power Sources*, 148:95–104, September 2005.
- [42] A. Madani. Use and Development of Battery Systems for HEV, EV and Plug in Hybrid Vehicles. In *Batteries 2010: The international energy and power supply conference and exhibition*, Cannes Mandelieu, 2010.

- [43] S. K. Martha, B. Hariprakash, S. A. Gaffoor, D. C. Trivedi, and A. K. Shukla. A low cost lead acid battery with high specific-energy. *Journal of Chemical Sciences*, 118:93–98, January 2006.
- [44] G J May, N Maleschitz, H Diermaier, and T Haeupl. The optimisation of grid designs for valve regulated lead acid batteries for hybrid electric vehicle applications. *Journal of Power Sources*, 195:4520–4524, July 2010.
- [45] P. T. Moseley, B. Bonnet, A. Cooper, and M. J. Kellaway. Lead acid battery chemistry adapted for hybrid electric vehicle duty. *Journal of Power Sources*, 174:49–53, November 2007.
- [46] P T Moseley and R D Prengaman. In pursuit of high specific energy, high specific power valve regulated lead-acid batteries. *Journal of Power Sources*, 107:240–244, 2002.
- [47] P. T. Moseley and D. A. J. Rand. Changes in the demands on automotive batteries require changes in battery design. *Journal of Power Sources*, 133:104–109, May 2004.
- [48] NASA. Definition Of Technology Readiness Levels. Technical report.
- [49] I Paleska, R Pruszkowska-Drachal, J Kotowski, Z Rogulski, J D Milewski, and A Czerwinski. Electrochemical behaviour of barium metaplumbate as a lead carrier. *Journal of Power Sources*, 129:326–329, April 2004.
- [50] D. Pavlov. A theory of the grid-positive active-mass (PAM) interface and possible methods to improve PAM utilization and cycle life of lead-acid batteries. *Journal of Power Sources*, 53:9–21, 1995.
- [51] D. Pavlov and E. Bashtavelova. A Model of the Structure of the Positive Lead Acid Battery Active Mass. *Journal of The Electrochemical Society*, 131:1468–1476, 1984.
- [52] D. Pavlov, P. Nikolov, and T. Rogachev. Influence of expander components on the processes at the negative plates of lead-acid cells on high-rate partial-state-of-charge cycling. Part I: Effect of lignosulfonates and BaSO4 on the processes of charge and discharge of negative plates. *Journal of Power Sources*, 195(14):4435–4443, July 2010.
- [53] I Petersson and E Ahlberg. Oxidation of electrodeposited lead tin alloys in 5 M H2SO4. Journal of Power Sources, 91:143–149, 2000.
- [54] D. Pletcher and R.G.A. Wills. A novel flow battery: A lead acid battery based on an electrolyte with soluble lead (II). Part II. Flow cell studies. *Physical Chemistry Chemical Physics*, (6):1779–1785, 2004.
- [55] D. Pletcher, H. Zhou, G. Kear, C.T. J. Low, F. C. Walsh, and R.G.A. Wills. A novel flow battery. A lead-acid battery based on an electrolyte with soluble lead(II) Part VI. Studies of the lead dioxide positive electrode. *Journal of Power Sources*, 180(1):630–634, May 2008.
- [56] R. Ponraj, S. D. McAllister, I. F. Cheng, and D. B. Edwards. Investigation on electronically conductive additives to improve positive active material utilization in lead-acid batteries. *Journal of Power Sources*, 189:1199–1203, April 2009.

- [57] M. Raghavan and D.C. Trivedi. Use of polyaniline in lead acid battery. *Synthetic Metals*, 119:285–286, 2001.
- [58] D Rand. The lead Acid battery: a key technology for global energy management. *Journal of Power Sources*, 64(1-2):157–174, January 1997.
- [59] A. Roos and P. Hedenqvist. Corrosion protetion of aluminium surfaces using pyrolytic tin oxide. *Applied Physics Letters*, 59:25–27, 1991.
- [60] M. Saakes, C. Kleijnen, and D. Schmal. Advanced bipolar lead acid battery for hybrid electric vehicles. *Journal of Power Sources*, 95:68–78, 2001.
- [61] M. Saakes, D. Schellevis, D. V. Trier, and M. Wollersheirn. Performance and use of composite substrate-based bipolar lead acid batteries for pulsed-power applications. *Journal of Power Sources*, 67:33–41, 1997.
- [62] M. Saakes, R. Woortmeijer, and D. Schmal. Bipolar lead acid battery for hybrid vehicles. Journal of Power Sources, 144:536–545, June 2005.
- [63] S. Schaeck, A. O. Stoermer, F. Kaiser, L. Koehler, J. Albers, and H. Kabza. Lead acid batteries in micro-hybrid applications. Part I. Selected key parameters. *Journal of Power Sources*, 196:1541–1554, February 2011.
- [64] M. Soria, J. Fullea, F. Saez, and F. Trinidad. Lead acid batteries with polymer structured electrodes for electric vehicle applications. *Journal of Power Sources*, 78:220–230, March 1999.
- [65] M.L. Soria, F. Trinidad, J. M. Lacadena, J. Valenciano, and G. Arce. Spiral wound valve regulated lead acid batteries for hybrid vehicles. *Journal of Power Sources*, 174:41–48, November 2007.
- [66] F Trinidad, C Gimeno, J Gutiérrez, R Ruiz, J Sainz, and J Valenciano. The VRLA modular wound design for 42 V mild hybrid systems. *Journal of Power Sources*, 116(1-2):128-140, July 2003.
- [67] F. Trinidad, F. Saez, and J. Valenciano. High power valve regulated lead acid batteries for new vehicle requirements. *Journal of Power Sources*, 95:24–37, 2001.
- [68] W. Utomo and S. W. Donne. Electrochemical behaviour of titanium in H2SO4 MnSO4 electrolytes. *Electrochimica Acta*, 51:3338–3345, April 2006.
- [69] J R Vilche and F E Varela. Reaction model development for the Pb PbS04 system. *Journal of Power Sources*, 64:39–45, 1997.
- [70] R. Wagner. Failure modes of valve regulated Lead Acid batteries in different applications. Journal of Power Sources, 53:153–162, January 1995.
- [71] R. Wagner. High power lead acid batteries for different applications. *Journal of Power Sources*, 144:494–504, June 2005.

- [72] L.P.J. Wallis and R.G.A. Wills. Membrane divided soluble lead battery utilising a bismuth electrolyte additive. *Journal of Power Sources*, 247:799–806, 2014.
- [73] F. C. Walsh and R. G. A. Wills. The continuing development of Magnéli phase titanium sub-oxides and Ebonex electrodes. *Electrochimica Acta*, 55:6342–6351, September 2010.
- [74] J. Wang, Z. P. Guo, S. Zhong, H. K. Liu, and S. X. Dou. Lead coated glass fibre mesh grids for lead acid batteries. *Journal of Applied Electrochemistry*, 33:1057–1061, 2003.
- [75] H. Warlimont and T. Hofmann. Simultaneous optimisation of the properties of engineered composite grids for lead acid batteries. *Journal of Power Sources*, 158:891–896, August 2006.
- [76] R. G. A. Wills, J. Collins, D. Stratton-Campbell, C. T. J. Low, D. Pletcher, and Frank C. Walsh. Developments in the soluble lead acid flow battery. *Journal of Applied Electrochemistry*, 40(5):955–965, March 2010.
- [77] Working Group III. Fifth Assessment Report. Technical report, IPCC, 2014.
- [78] L A Yolshina and V G Zyryanov. Development of an electrode for lead acid batteries possessing a high electrochemical utilization factor and invariable cycling characteristics. *Journal of P*, 65:71–76, 1997.
- [79] N Yu and L Gao. Electrodeposited PbO2 thin film on Ti electrode for application in hybrid supercapacitor. *Electrochemistry Communications*, 11:220–222, January 2009.